UNIVERSITY OF CALIFORNIA, SAN DIEGO

Advancing solar irradiance/marine layer stratocumulus forecasting in California

A dissertation submitted in partial satisfaction of the requirements for the degree of Doctor of Philosophy

in

Engineering Sciences (Mechanical Engineering)

by

Xiaohui Zhong

Committee in charge:

Professor Jan Kleissl, Chair
Professor Carlos Coimbra
Professor Juan Carlos Del Alamo
Professor Joel Norris
Professor Shang-Ping Xie

2017

The Dissertation of Xiaohui Zhong is approved and it is acceptable in quality and form for publication on microfilm and electronically:

Chair

University of California, San Diego

2017

EPIGRAPH

April showers bring May flowers.

Thomas Tusser

TABLE OF CONTENTS

LIST OF FIGURES

LIST OF TABLES

ACKNOWLEDGEMENTS

I would like to first thank Professor Jan Kleissl for allowing me to join his group and begin this wonderful and memorable study and research journey, in which I have no regret and only gratitude. In the past few years, I have grown stronger both intellectually and psychologically. I also appreciate Jan's trust, guidance, and feedbacks so that I feel more and more confident to embrace challenges one after another. Once a teacher, always a teacher.

Furthermore, I want to express my sincere appreciation for the UCSD Solar Resource Assessment and Forecasting (SRAF) lab: Handa Yang, Patrick Mathiesen, Israel Lopez, Mohamed Ghonima, Dipak Sahu, Ben Kurtz, Andu Nguyen, Bengu Ozge Akyurek, Elynn Wu, Monica Zamora Zapata, Felipe Mejia, Guang Wang, Oytun Babacan, Ryan Hanna, Changfu Li, Zachary Pecenak, Bryan Urquhart, Matthew Lave, Abdulelah Habib, Victor Fung, Iman Gohari, Juan Bosch.

Chapter 2, in full, is a reprint of the materials as it appears in Zhong, X., Ruiz-Arias, J. A., and Kleissl, J., 2016: Dissecting Surface Clear Sky Irradiance Bias in Numerical Weather Prediction: Application and Corrections to the New Goddard Shortwave Scheme. *Solar Energy*. The dissertation/thesis author was the primary investigator and author of this paper.

Chapter 3, in full, is a reprint of the material as it appears in Zhong, X., D. K. Sahu, and J. Kleissl, 2017: WRF inversion base height ensembles for simulating marine boundary layer stratocumulus. *Solar Energy*. The dissertation/thesis author was the primary investigator and author of this paper.

Chapter 4, in part is currently being prepared for submission for publication of the material as it may appear in Zhong, X., Lauret, P., and Kleissl, J., 2017: Intra-day solar energy prediction using machine learning models with selected meteorological variables over southern California. *Solar Energy*, to be submitted. The dissertation/thesis author was the primary investigator and author of this paper.

VITA

2012 Bachelor of Engineering, Wuhan University

2013 Master of Science, University of California, San Diego

2017 Doctor of Philosophy, University of California, San Diego

PUBLICATIONS

Zhong, X., Lauret, P., and Kleissl, J., 2017: Intra-day solar energy prediction using machine learning models with selected meteorological variables over southern California. In preparation.

Zhong, X., D. K. Sahu, and J. Kleissl, 2017: WRF inversion base height ensembles for simulating marine boundary layer stratocumulus. *Solar Energy,* 146, 50–64.

Sahu, D. K., Kim, C. K., **Zhong, X.**, and Kleissl, J., 2016: Assimilating in-situ observations over Southern California for improved solar forecasting. *IEEE 43rd Photovoltaic Specialists Conference (PVSC)*.

Zhong, X., Ruiz-Arias, J. A., and Kleissl, J., 2016: Dissecting Surface Clear Sky Irradiance Bias in Numerical Weather Prediction: Application and Corrections to the New Goddard Shortwave Scheme. *Solar Energy*, 132, 103-113.

Zhong, X., and Kleissl, J., 2015: Clear sky irradiances using REST2 and MODIS. *Solar Energy*, 116, 144-164.

ABSTRACT OF THE DISSERTATION

Advancing solar irradiance/marine layer stratocumulus forecasting in California

by

Xiaohui Zhong

Doctor of Philosophy in Engineering Sciences (Mechanical Engineering)

University of California, San Diego, 2017

Professor Jan Kleissl, Chair

In summertime mornings, marine boundary layer (MBL) stratocumulus clouds commonly cover the southern California coast. The formation and dissipation of MBL stratocumulus affect the photovoltaic (PV) power. Increasing rooftop solar PV generation over the coast necessitates accurate solar forecasts to facilitate the reliable and economical integration of solar PV into the electric grid. For forecast horizons of hours to days, numerical weather prediction (NWP) and machine learning techniques are considered as the most accurate methods and widely used. However, the comparisons of

NWP irradiance forecasts with ground measurements show that NWP models consistently overestimate the solar irradiance at the surface due to both clear sky biases and cloud modelling issues. As for machine learning techniques, most researchers either deliberately ignore meteorological conditions (for endogenous forecast models) or lack meteorological expertise to select meteorological input variables that go beyond classical weather station measurements such as air temperature, wind speed, and relative humidity. In this study, several methods are proposed to improve both NWP and machine learning forecast accuracy. Firstly, the clear sky irradiance bias in the New Goddard Shortwave (SW) scheme of Weather Research and Forecasting (WRF) scheme are found to be missing absorption of water vapor continuum. Use of the new parameterization of water vapor including water vapor continuum reduced WRF's clear sky biases. Secondly, we confirmed the positive correlation between temperature inversion base height (IBH) and inland extent of MBL stratocumulus, and postulated that WRF underprediction of cloud cover extent is due to underprediction of IBH. A thermodynamic method was developed to modify the boundary layer temperature and moisture profiles to better represent the boundary layer structure in WRF. Validation against satellite global horizontal irradiance (GHI) demonstrated that the best IBH ensemble improves GHI accuracy by 23% mean absolute error compared to the baseline WRF model and is similar to 24-hour persistence forecasts for coastal marine layer region. The spatial error maps showed deeper inland cloud cover. Thirdly, we focused on selecting appropriate meteorological input variables based on the characteristics of MBL clouds and studied how accurately support vector machine (SVM), random forest (RF), and gradient boosting (GB) machine learning models predict solar radiation. All three models significantly outperform physics-based

NWP models and 24-hour persistence in predicting solar radiation, especially during cloudy periods in the morning. The most important meteorological variables are found to be liquid water path, IBH, and thickness between 1000 and 500 mb pressure levels.

1. Introduction

1.1. Marine boundary layer (MBL) stratocumulus

Stratocumulus clouds are critical to the Earth's radiative budget as a result of their strong net negative radiative effect and enormous spatial coverage (Hartmann et al. 1992; Wood 2012). Annually, 22% of the ocean surface and 12% of the land surface is covered by stratocumulus (Hahn and Warren 2007; Eastman et al. 2011). Stratocumulus preferably occur in a shallow planetary boundary layer (PBL) capped by a strong temperature inversion. The strong inversion inhibits warm dry air from above from penetrating the inversion that would otherwise facilitate cloud evaporation (Bretherton and Hartmann 2009).

Marine boundary layer (MBL) stratocumulus clouds are an important climate and weather feature along the California coast, and are especially dominant in Southern California during the summer months (Iacobellis and Cayan 2013a). In California, the majority of rooftop solar photovoltaic (PV) panels are installed near the coast, thus the PV power generation is strongly affected by the formation and dissipation of MBL stratocumulus (Jamaly et al. 2013). Accurate solar forecasts facilitate the reliable and economical integration of solar PV into the electric grid.

Solar forecasting for California is challenging mainly due to complexity of the MBL clouds (Zhong et al. 2017). Solar radiation is lowest during the mornings during the summer months of May through September as a result of persistent occurrence of coastal MBL clouds. A variety of factors control the spatial and temporal variations of MBL clouds. Iacobellis and Cayan (2013) and Zhong et al. (2017) demonstrated that the inland

penetration of the MBL clouds are determined by the inversion base height and coastal topography. Ghonima et al. 2016) investigated factors controlling lifetime of coastal MBL clouds using large eddy simulation (LES) and mixed layer model (MLM). They concluded that cloud lifetime depends on the cloud-top entrainment flux, the Bowen ratio of the surface, and the strength of advection of cool ocean air by the sea breeze. Myers and Norris (2013) analyzed satellite cloud data and reanalysis meteorological parameters to study the effect of subsidence and inversion strength on MBL cloud fraction and liquid water path (LWP). They found that the reduced subsidence or enhanced inversion strength increases cloud fraction and total liquid water path. Through a simple conceptual model, they illustrated that weaker subsidence leads to higher cloud top and greater cloud thickness and cloud fraction while stronger inversion results in less entrainment drying and greater cloud fraction. Within the southern California Bight, a counter-clockwise circulation occasionally develops in the marine layer from Point Conception to San Diego, which is called Catalina Eddy (Bosart 1983; Davis and Low-Nam 2000). The Catalina Eddy, is usually accompanied by the development of southerly wind, deepening of the marine layer, and persistent MBL clouds over the southern California coast (Mass and Albright 1989).

In this project, we applied two approaches to forecast MBL stratocumulus: a numerical weather prediction model, more specifically, Weather and Research and Forecasting Model (WRF), and machine learning models.

1.2. Weather Research and Forecasting Model (WRF)

The WRF model is a state-of-the-art numerical weather prediction (NWP) model based on the simplified versions of equations describing the evolution of atmosphere. Since the first attempt of one-day weather forecast using a one-layer model in 1949 (Charney et al. 1950), the NWP models have evolved significantly to multi-layer models capable of predicting tropical cyclone, wildfires, and thunderstorms thanks to the increasing power of supercomputers. This remarkable evolution of NWP models' complexity has both advantages and disadvantages. The advantage is greatly improved forecast benefits for both individuals and weather-related industries, e.g. airlines, agriculture, wind and solar power generation. The disadvantage is that it is harder for scientists and researchers to understand model behavior and improve model accuracy.

1.2.1. Physical Parameterizations

Similar to other modern NWP models, WRF consists of two major components: numerical techniques and physical parametrizations. The numerical techniques are used to step forward the governing thermo-fluid equations in time as they are not analytically solvable. Parameterizations are also necessary and important as they represent some processes that are either too small scale to be resolved explicitly or too complex. For example, the process involving phase change of water are too complex and not fully understood. Therefore, parameterization schemes are designed to simplify complex processes using assumptions and derive statistical/empirical relationships or approximations based on observations.

The parameterized physics include radiative transfer (longwave and shortwave scheme), surface processes (land surface scheme), vertical turbulent mixing (planetary boundary scheme), clouds and large-scale condensation (microphysics scheme), and convection (cumulus and shallow cumulus scheme). Radiation schemes calculate both net radiative flux at the ground surface needed for the surface energy budget and vertical radiative flux divergence for radiative heating and cooling. The radiation model considers absorption, reflection, and scattering due to the predicted cloud and water vapor as well as ozone, aerosols, and background gases (e.g., trace gases) which are usually prescribed by climatological look-up tables. Although many simplifications are made to make radiation parametrizations more computationally affordable, radiation schemes are still computationally expensive and often called less frequently than other schemes.

Land surface schemes define properties of the land surface that affect the partitioning into surface sensible and latent heat fluxes. The planetary boundary layer scheme is responsible for determining vertical mixing in the entire atmospheric column, but especially to represent mixing effects of turbulence in the boundary layer. After decomposing each variable into a mean and a perturbation (Reynolds averaging) and substituting into the Navier-Stokes equations, there are more unknowns than equations, which is called a turbulence closure problem. Therefore, unknowns need to be expressed in terms of known variables and two approaches called local closure and non-local closure are used (Stensrud 2009). The local closure relates the unknown variables to known variables at adjacent vertical grids while non-local closure relates the unknown variables to known variables at any vertical grid point. As the size of eddies responsible for most of turbulent mixing are usually of the boundary depth, use of non-local schemes

often predict boundary layer height and boundary layer turbulence more accurately than local schemes.

The microphysics parametrizations attempt to model the microphysical processes of cloud formation, growth, dissipation, and precipitation. Cumulus parametrizations represent the effects of subgrid scale convective processes such as unresolved updrafts and downdrafts on resolved variables. Theoretically, they are necessary for simulations using coarse grids and they should be turned off when the grid is finer than 4 km as resolutions of 4 km are sufficient to resolve convective processes explicitly (Weisman et al. 1997; Gilliland and Rowe 2007).

Comparisons of current NWP solar irradiance forecasts with ground measurements show that NWP models often overestimate the solar irradiance at the surface (Remund et al. 2008; Lorenz et al. 2009; Lara-Fanego et al. 2011). This bias is due to both clear sky part of radiation schemes and cloud modelling issues. The following two sections will discuss clear sky biases and NWP modelling issue of MBL stratocumulus clouds over southern California in more detail.

1.2.2. WRF clear sky biases

Often, but not always (as it is detailed below), clear sky biases are related to aerosol modeling issues (Ruiz-Arias et al. 2013; Jimenez et al. 2015; Ruiz-Arias et al. 2015). Although applying model output statistics (MOS) approaches (Mathiesen and Kleissl 2011; Lorenz et al. 2009) can reduce these biases in NWP irradiance, MOS functions may not be applicable across sites and seasons. Moreover, correcting the source of error directly in the model would result in more accurate solar heating at the surface

and the atmospheric column and, therefore, improve other forecast variables such as temperature.

Ruiz-Arias et al. (2012) showed that neglecting or oversimplifying the aerosols attenuation of solar radiation in the Rapid Radiative Transfer Model for Global Circulation Models (RRTMG) and New Goddard SW radiative transfer schemes of the WRF model causes positive surface solar irradiance biases with respect to ground observations. Since version 3.6 of the WRF model, a parameterization of the aerosol optical properties is implemented in these two SW schemes (Ruiz-Arias et al., 2014). Overall, the use of a good estimate of aerosol optical depth and this new parameterization, significantly improved the agreement of the RRTMG and New Goddard clear-sky solar radiation predictions with ground observations for global horizontal irradiance (GHI), direct normal irradiance (DNI), and diffuse horizontal irradiance (DIF). Ruiz-Arias et al., (2014) showed that, using RRTMG in WRF, the relative MBE of GHI, DNI and DIF decreased from 1%, 7% and -34% to 0%, 0% and 3%, respectively. Using the New Goddard SW scheme, in contrast, the relative MBE decreased from 4%, 11% and -32% to 2%, 5% and -5%, respectively. This residual bias in the New Goddard SW scheme remained unexplained by Ruiz-Arias et al. (2014). Although the RRTMG SW scheme was superior to the New Goddard SW scheme in terms of clear-sky radiation, López-Coto et al. (2014) showed that the latter performs better at simulating cloud formation near the California coast. Therefore, the removal of the remaining WRF's New Goddard SW scheme biases remains of interest and it cannot be accomplished solely through aerosol modeling improvements.

1.2.3. WRF biases in modelling MBL stratocumulus clouds

Understanding the causes of NWP biases is difficult due to the complexity of interactions between radiation (both shortwave and longwave), turbulence, surface fluxes, phase change, subsidence, and entrainment, and the variety of scales involved. Myers and Norris (2013) argued that stronger subsidence lowers cloud tops and reduces the cloudiness while a stronger inversion reduces entrainment drying and warming, thickening clouds. At night, cloud top longwave cooling is the main driver for turbulence that transports surface moisture to the cloud layer and maintains a well-mixed layer under the inversion (Lilly 1968). During the day, solar radiation absorbed within the clouds suppresses turbulence driven by longwave cooling (Wood 2012). Clouds may then dissipate due to a weakened coupling between clouds and surface moisture. Compared to the ocean, the land surface has less ability to store heat. A large portion of incoming solar radiation at the land surface is therefore returned to the atmosphere as sensible heat flux which tends to shorten stratocumulus life times. Brenguier et al. (2000) demonstrated that radiative properties of MBL stratocumulus also depend on aerosol properties. The processes that controls formation and dissipation of MBL stratocumulus range from planetary scale to droplet scale making MBL stratocumulus extremely challenging to understand and predict.

Increasingly, researchers are finding that NWP biases are largely due to misrepresentation of PBL properties. In particular for MBL stratocumulus, several lower atmospheric properties related to the temperature inversion have been linked to enhanced cloud cover. Klein and Hartmann (1993) demonstrated a correlation between MBL stratocumulus cloud cover and lower troposphere static stability (LTS) which is a proxy

measure of the inversion strength and defined as difference in potential temperature between 700 mb and the surface. Koračin et al. (2003) demonstrated that accurate prediction of the inversion base height (IBH) is crucial to the success of simulating the structure and evolution of the MBL. However, many studies evaluating NWP models in simulating stratocumulus show that the simulated PBL/MBL is too shallow. Hannay et al. (2009) examined several NWP models in representing regions of stratocumulus using cruise observations (Bretherton et al. 2004). They found that modeled PBL ranging between 400 and 800 m are substantially shallower than the observed IBH of about 1100 m. Although they suggested that the model PBL can be deepened by modifying the underestimated entrainment, they also argued that increasing entrainment increases the surface evaporation and can make overall simulation results worse. Similarly, Wyant et al. (2010) demonstrated that a wide range of contemporary atmospheric models from fourteen modeling centers underpredict the IBH but the interaction between mean IBH bias and mean cloud fraction bias was not clear. Rahn and Garreaud (2010a, 2010b) compared the Weather Research and Forecasting (WRF) modeled MBL with observations from the VOCALS Regional Experiment over the subtropical southeast Pacific. They found that WRF simulate the spatial variability of MBL correctly but underestimates the IBH. In addition, Iacobellis and Cayan (2013) showed that the inland penetration of MBL stratocumulus is controlled by where the IBH intersects with the coastal topography. The IBH controls the cloud top height, and the MBL stratocumulus can only extend inland when the ground elevation is lower than cloud top height. Therefore, we hypothesize that underestimation of the IBH limits the ability of WRF to accurately predict inland cloud cover.

In attempting to improve MBL height, most researchers focused on the PBL parameterizations which are most influential to atmospheric tendencies of temperature, moisture, and horizontal momentum in the PBL (Skamarock et al. 2008). Hu et al. (2010) concluded that the Mellor–Yamada–Janjic (MYJ) PBL scheme, which models mixing strength based on local gradients only, predicts lower PBL heights than two non-local schemes, the Yonsei University (YSU) scheme and the asymmetric convective model version 2 (ACM2), because of less vertical mixing and entrainment in MYJ than YSU and ACM2. They further confirmed their conclusion by showing that the PBL height varies monotonically with altered vertical mixing strength in ACM2. Jousse et al. (2016) suggested that the differences in mixing strength formulations between the MYJ and the Mellor-Yamada Nakanishi and Niino PBL schemes (MYNN) cause MYNN to outperform MYJ in representing PBL height. Banks et al. (2015) revealed large difference in WRF simulated PBL heights using eight PBL schemes. They proposed that different definitions of PBL height and differences in the entrainment formulations are responsible for the differences.

Despite intense research efforts, accurate forecasts of PBL height and stratocumulus are still elusive. Independent of the skill of a particular regional NWP model, the bias in initial conditions is still inherited from the parent model. Therefore, improving the initial conditions is pertinent such as in Koračin et al. (2003) who used satellite data to modify mesoscale NWP initial conditions. This led to better representation of the IBH and more accurate prediction of cloud development. Kann et al. (2009) developed an empirical subinversion cloudiness enhancement scheme which yielded more realistic temperature inversion and cloudiness.

1.3. Machine learning models

Unlike WRF model that is physics based, machine learning models are data-driven approaches which predict the future based on the relations between input variables and target variable learned from past data.

Machine learning models are more and more widely used for predicting solar radiation and solar power (Lauret et al. 2015; Antonanzas et al. 2016; Chen et al. 2013; Pedro and Coimbra 2017). Despite this increasing popularity, most researchers either deliberately ignore meteorological conditions (for endogenous forecast models) or lack meteorological expertise to select meteorological input variables that go beyond classical weather station measurements such as air temperature, wind speed, and relative humidity. However, the performance of machine learning models largely depends on the selection of input variables (Bluma and Langley 1997; Guyon and Elisseeff 2003), and the amount of solar radiation depends on meteorological and climatic conditions. Under clear sky conditions, the solar radiation varies mainly due to aerosols and water vapor. Under cloudy conditions, the solar radiation varies mainly due to cloud optical depth.

Zeng and Qiao (2013) trained support vector machine (SVM), an autoregressive (AR) model, and a radial basis function neural network (RBFNN)-based model using the latest observed solar radiation, radiation at the hour of prediction during the previous two days, as well as latest measurement of meteorological variables including sky cover, relative humidity and wind speed to predict 1 hour ahead atmospheric transmissivity. Validation demonstrated the superiority of SVM over AR and RBFNN because the regularization terms in SVM models limit overfitting in the training stage and improve the generalization ability. They also showed that use of meteorological variables,

especially sky cover, improves prediction accuracy compared to models with only solar radiation. Sharma et al. (2011) used historical National Weather Service (NWS) weather forecasts of temperature, dew point, wind speed, sky cover, probability of precipitation, relative humidity and solar radiation to build linear least squares regression and SVM with multiple kernel functions to predict solar radiation within next three hours. They found that SVM model with RBF kernels achieved the highest accuracy. Zamo et al. (2014) tested several machine learning models including SVM, random forest (RF), and gradient boosting (GB) using 31 outputs from the numerical weather prediction model ARPEGE (see Table 1 in their paper) to generate day-ahead PV forecasts. Their benchmark designated RF as the best forecast model in predicting hourly PV production for the next day.

1.4. Thesis Outline

The outline of the thesis is as follows. In Chapter 2, the bias errors of the WRF's New Goddard SW scheme associated with the multiple atmospheric constituents of relevance under clear-sky conditions (i.e., gases, ozone, water vapor and aerosols) are dissected independently following an original approach. The effect of each constituent is isolated by subtracting from the GHI predicted for an atmosphere that lacks one constituent, the GHI predicted for an atmosphere with all the constituents. In Chapter 3, we proposed an approach to improve representation of boundary layer temperature and moisture to correct IBH before sunrise. In Chapter 4, we focused on selecting the meteorological input variables based on the characteristics of MBL clouds over southern California and studied how accurately SVM, RF, and GB predict solar radiation. Chapter

5 summarizes the most important findings in this thesis and some thoughts on the future research.

2. Dissecting and Corrections of Clear Sky Irradiance Bias in Numerical Weather Prediction

Clear-sky GHI is attenuated primarily by four atmospheric constituents: (i) Ozone (ii) background gases (e.g., trace gases), (iii) precipitable water and, (iv) aerosols. The effect of each constituent in the New Goddard SW scheme is isolated here by subtracting from the GHI predicted for an atmosphere that lacks one constituent, the GHI predicted for an atmosphere with all the constituents. Compared with the WRF's RRTMG, the main contributions to the clear-sky irradiance bias in the New Goddard SW scheme come from modeling issues with the absorptions by water vapor and ozone. Enhancing the absorption due to water vapor continuum and using the RRTMG's ozone profiles in the New Goddard SW scheme improved the agreement with the WRF's RRTMG predictions for both GHI and direct normal irradiance. These results are further confirmed with the REST2 radiative transfer model.

Section 2.1 describes radiative transfer models, the configuration of the WRF model, as well as the input data. The method for dissecting the bias errors is described in Section 2.2, and applied in Section 2.3 to the New Goddard SW scheme. An approach for correcting the bias related to ozone absorption and a parameterization to account for water vapor continuum are proposed in Section 2.4. Section 2.5 shows the validation results of the improved New Goddard SW model benchmarked against the WRF's RRTMG SW scheme and the high-performance broadband clear-sky irradiance REST2 model. Concluding remarks are made in Section 2.6.

2.1. Model Description

2.1.1. WRF Model Setup

The version 3.6 of WRF is used and configured with a single domain (no nesting) of 40×40 grid cells at a horizontal resolution of 4 km centered at grid point at latitude of 32.87 N and longitude of 117.25 W. WRF is initialized using the North American Model (NAM) for boundary and initial conditions. The model is integrated every 5 seconds with radiation schemes called every 5 minutes. Physical parameterizations include the Morrison double-moment scheme for microphysics (Morrison et al. 2009), Noah for land surface, Mellor-Yamada Nakanishi and Niino Level 2.5 for planetary boundary layer (PBL) mixing (MYNN, Nakanishi and Niino, 2006), and New Simplified Arakawa-Schubert for cumulus (NSAS, Han and Pan, 2011).

Table 2.1 shows the name convention for the model runs. For the WRF ensembles (names starting with "WRF"), "Goddard", "RRTMG", or "Goddard 2" indicate different combinations of SW schemes and sources for atmospheric input data. Both WRF Goddard and WRF Goddard 2 were initialized every 24 hours and run for ten days from June 1 to June 10, 2013. WRF RRTMG was only run for June 10, 2013. Besides, WRF was configured such that in parallel to the total optical depth including clouds, a separate optical depth without clouds was generated, such that the clear-sky irradiance was obtained for both clear and cloudy days simultaneously.

Table 2.1: Ensemble forecasts name convention (column 1) and atmospheric inputs common to WRF and REST2 (columns 2 to 4).

Ensemble Name	AOD [-]	Water vapor	Ozone
WRF Goddard	Fixed to 0.12 at 0.55 μm, with rural aerosol type	Dynamic from WRF simulation	Goddard Ozone
WRF RRTMG			RRTMG Annual Ozone
WRF Goddard 2			RRTMG Annual Ozone
REST2 Goddard			Goddard Ozone
REST2 Goddard 2			RRTMG Annual Ozone

2.1.2. The REST2 Clear-Sky Model

REST2 is a clear-sky broadband radiative transfer model (Gueymard 2008) which has proven to be a top performer of its class (Gueymard 2012; Gueymard and Ruiz-Arias 2015) and, thus, it is used as a benchmark here. The model consists of transmittance parameterizations derived from the Simple Model of the Atmospheric Radiative Transfer of Sunshine (SMARTS) spectral solar irradiance model (Gueymard 2001). REST2 uses atmospheric inputs that include Ångström's wavelength exponent (AEX), Ångström's turbidity coefficient, aerosol single-scattering albedo, total column amount of ozone, nitrogen dioxide and water vapor (Gueymard 2012; Zhong and Kleissl 2015). It treats the spectral UV and visible bands (from 0.29 to 0.70 μm), and the spectral near-infrared (from 0.7 to 4 μm) band separately.

For the REST2 runs (ensemble names starting with "REST2") in Table 2.1, "Goddard" and "Goddard 2" indicate different sources of atmospheric input data. REST2 is run for validation from June 1 to June 10, 2013, using the same atmospheric constituents (aerosols, ozone and water vapor) as in the WRF simulations.

2.1.3. New Goddard and RRTMG shortwave schemes

The (New) Goddard solar radiative transfer scheme explicitly takes into account the extinction by water vapor, ozone, oxygen, carbon dioxide, aerosols, Rayleigh scattering, and clouds (Chou and Suarez 1999; Chou and Lee 1996; Chou 1990, 1992). Fluxes are integrated using the two-stream adding method over the spectral range from 0.175 to 10 μm. Reflection and transmission of each layer are computed using the δ-Eddington approximation (Joseph et al. 1976), which induces about a 5% bias in transmissivity and reflectivity (King and Harshvardhan 1986). The SW spectrum is divided into eight different bands in the ultraviolet (UV) and photosynthetically active (PAR) regions and three bands in the infrared region. Band-specific coefficients for ozone absorption and Rayleigh scattering (WMO, 1986) are used. In the near infrared, the k-distribution method is applied for water vapor absorption. Overall, the Goddard model is expected to represent atmospheric heating rates between 0.01 hPa and the surface to within 5% deviation relative to the line-by-line method (Chou and Suarez 1999). Improvements on optical depths for condensates, two-stream adding approximation, delta-Eddington approximation and molecular absorption were included in the WRF's implementation of the New Goddard SW scheme (Shi et al. 2007). Thus, it is known as New Goddard SW scheme in the realm of the WRF NWP model.

The RRTMG SW scheme is a simplified version of the RRTM SW model (Mlawer et al. 1997) for GCMs with better computational efficiency and minimal loss of accuracy (Iacono et al. 2008). It explicitly accounts for extinction due to water vapor, carbon dioxide, methane, oxygen, nitrogen, aerosols, Rayleigh scattering and clouds, and

calculates fluxes over the spectrum from 0.2 to 12.2 μm. RRTMG shares basic physics and absorption coefficients with RRTM.

2.1.4. Atmospheric Constituent Inputs

The New Goddard SW radiation scheme requires inputs of the optical depth of atmospheric constituents as detailed in Table 2.1. AOD, water vapor, and ozone are chosen to be identical in REST2 Goddard (REST2 Goddard 2) and WRF Goddard (WRF Goddard 2). Aerosol optical properties are parameterized in terms of the total aerosol optical depth (AOD) at 0.55 μm and a reference aerosol type to determine AEX, and spectral values of single-scattering albedo and asymmetry parameter, which are further modulated by relative humidity (Ricchiazzi et al. 1998; Gueymard 2001; Ruiz-Arias et al. 2014).

Constituents that are not listed in the table, but are unique to each model and have a negligible effect on surface irradiance are 0.2 matm-cm of nitrogen dioxide in REST2, 320 ppbv of nitrous oxide and 336 ppmv of carbon dioxide in the New Goddard SW scheme, and 319 ppbv of nitrous oxide and 379 ppmv of carbon dioxide in the RRTMG SW scheme.

2.1.5. Anecdotal Evidence that New Goddard Biases are Model Errors, not Input Errors

Figure 2.1 shows time series of difference of WRF Goddard (Table 2.1) compared to clear sky GHI, DNI and DIF computed from REST2 Goddard. Even with aerosols, WRF Goddard presents significant difference, especially for DNI, consistent with Ruiz-Arias et al. (2013).

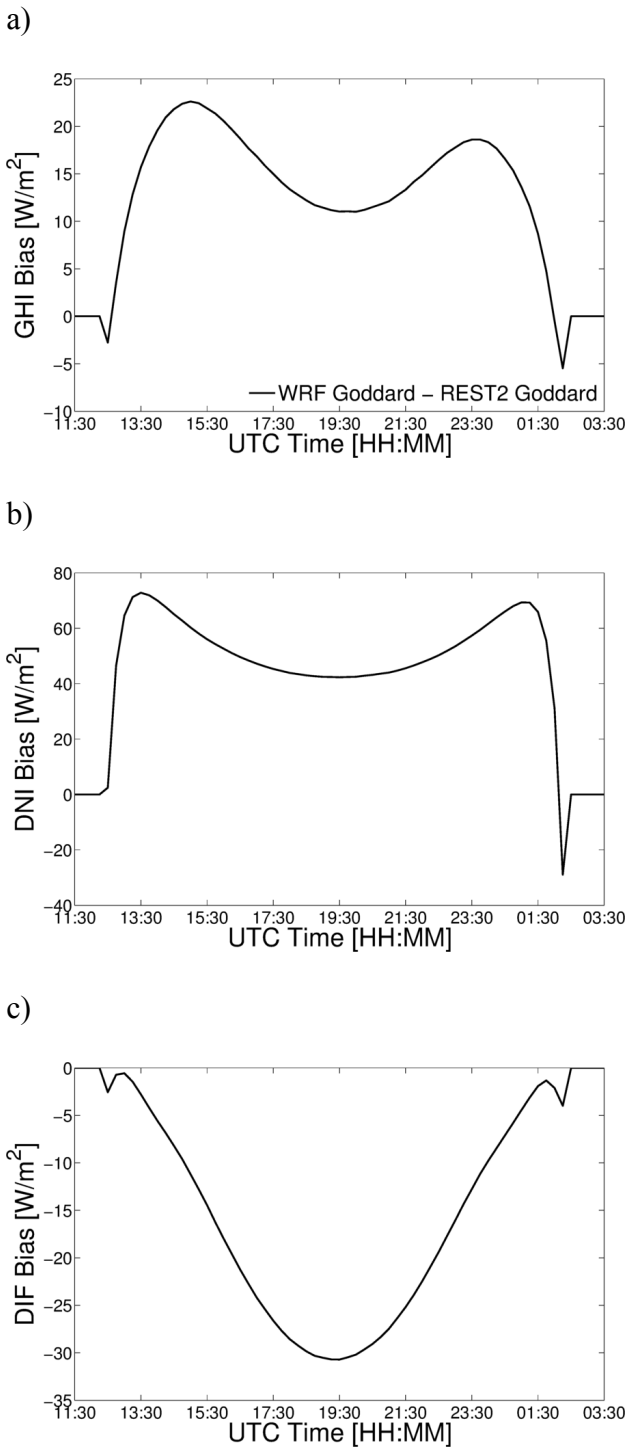

Figure 2.1: Clear sky GHI (a), DNI (b) and DIF (c) difference time series of WRF Goddard (see Table 1) versus REST2 Goddard data at the grid point at 32.87 N, 117.25 W for daytime on June 10, 2013.

2.2. Separating the Effects of each Constituent on GHI

In order to determine the source of error in the New Goddard SW model, the effect of different atmospheric constituents is analyzed separately. In the New Goddard and RRTMG SW models, the effective optical depth, single scattering albedo, and asymmetry factor are computed for each atmospheric layer and spectral band by adding contributions from ozone, water vapor, aerosols, and other atmospheric gases (i.e. Rayleigh scattering) (Chou and Suarez 1999). Note that clouds are excluded from this analysis. The flux reduction due to oxygen and carbon dioxide is small compared to the error observed in Figure 2.1, so their contributions are not investigated further. Computing the extinction effect of each constituent directly from within the model is cumbersome because the transmittance is calculated for each vertical layer and spectral band from solar zenith angle and total optical properties. Instead, we choose an empirical approach which excludes one constituent at a time from the calculation of the layer's optical properties by zeroing that constituent. The difference between GHI predicted for an atmosphere with one constituent excluded and GHI predicted for an atmosphere with all constituents is normalized by GHI at the top of the atmosphere, which leads to the attenuation due to that constituent. Then, the transmittance at the surface due to each constituent is calculated using

$$T_{X,1} = \left(1 - \frac{GHI_{w/o\,X} - GHI}{GHI^{TOA}}\right)^{\mu}, \tag{2.1}$$

where $T_{X,1}$ is the transmittance of each atmospheric constituent normalized by the cosine of the solar zenith angle (μ) to remove air mass dependence, GHI^{TOA} is GHI at the top of atmosphere, GHI is calculated with all constituents considered while $GHI_{w/o\,X}$ is

calculated after removing ("without" = w/o) one constituent. X can be aerosol, water vapor, ozone or Rayleigh scattering. Figure 2.2a illustrates the case when the contribution of water vapor is calculated ($T_{wv,1}$).

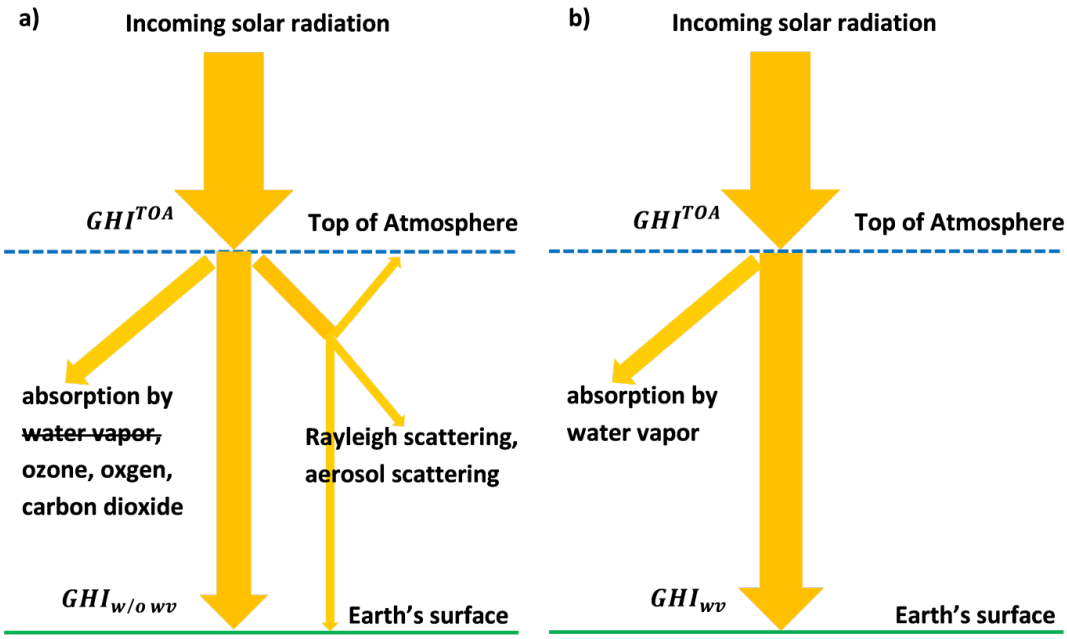

Figure 2.2: Illustration of the calculation of GHI reduction due to water vapor by using Eq. 2.1 (a) and Eq. 2.2 (b), respectively.

An alternative approach is to simulate an atmosphere with only one constituent at a time. The resulting GHI_X is divided by GHI^{TOA} to derive T (see Figure 2.2b) as

$$T_{X,2} = \left(\frac{GHI_X}{GHI^{TOA}}\right)^{\mu}. \quad (2.2)$$

Differences between $T_{X,1}$ and $T_{X,2}$ are caused by the interaction between different constituents. For example, $T_{AOD,1}$ is greater than $T_{AOD,2}$ since water vapor and ozone reduce the direct irradiance that can interact with aerosols. In this paper, both Eqs. 2.1 and 2.2 are used to analyze the causes of GHI biases.

2.3. Contribution of Atmospheric Constituents to the GHI and DNI bias

2.3.1. Separating the Contribution for each Constituent

Table 2.2 and Figure 2.3 show that for this case study water vapor dominates the reduction in GHI at the surface with transmittance of RRTMG at noon, per Eq.2.2, equal to about 86.8% followed by Rayleigh scattering (95.6%), ozone (97.3%) and aerosols (98%). The difference in $T_{X,2}$ between WRF Goddard and WRF RRTMG by atmospheric constituent provides clues about the source of bias in the New Goddard SW scheme. Compared to RRTMG, the New Goddard SW scheme overestimates the transmittance due to ozone and water vapor absorption by about 1% each (corresponding to about 10 W m^{-2} at solar noon) respectively, on average, while the difference for aerosols (< 4 W m^{-2} or $\Delta T_{AOD,2}$ < 0.1% near solar noon) and Rayleigh scattering (< 5 W m^{-2} or $\Delta T_{RS,2}$ < 0.3% near solar noon) is smaller.

Table 2.2 Transmittance at solar noon due to aerosols, ozone, water vapor and Rayleigh scattering calculated using Eq. 2.1 and Eq. 2.2 in the New Goddard and RRTMG SW schemes. Rows 2 and 4 are differences (Goddard - RRTMG) in $T_{X,1}$ and $T_{X,2}$, respectively.

	aerosol		ozone		water vapor		Rayleigh scattering	
	Goddard	RRTMG	Goddard	RRTMG	Goddard	RRTMG	Goddard	RRTMG
$\boldsymbol{T_{X,1}}$	0.985	0.985	0.989	0.983	0.879	0.880	0.967	0.966
Difference	0.000		0.006		-0.001		0.001	
$\boldsymbol{T_{X,2}}$	0.981	0.980	0.983	0.973	0.878	0.868	0.959	0.956
Difference	0.001		0.010		0.010		0.003	

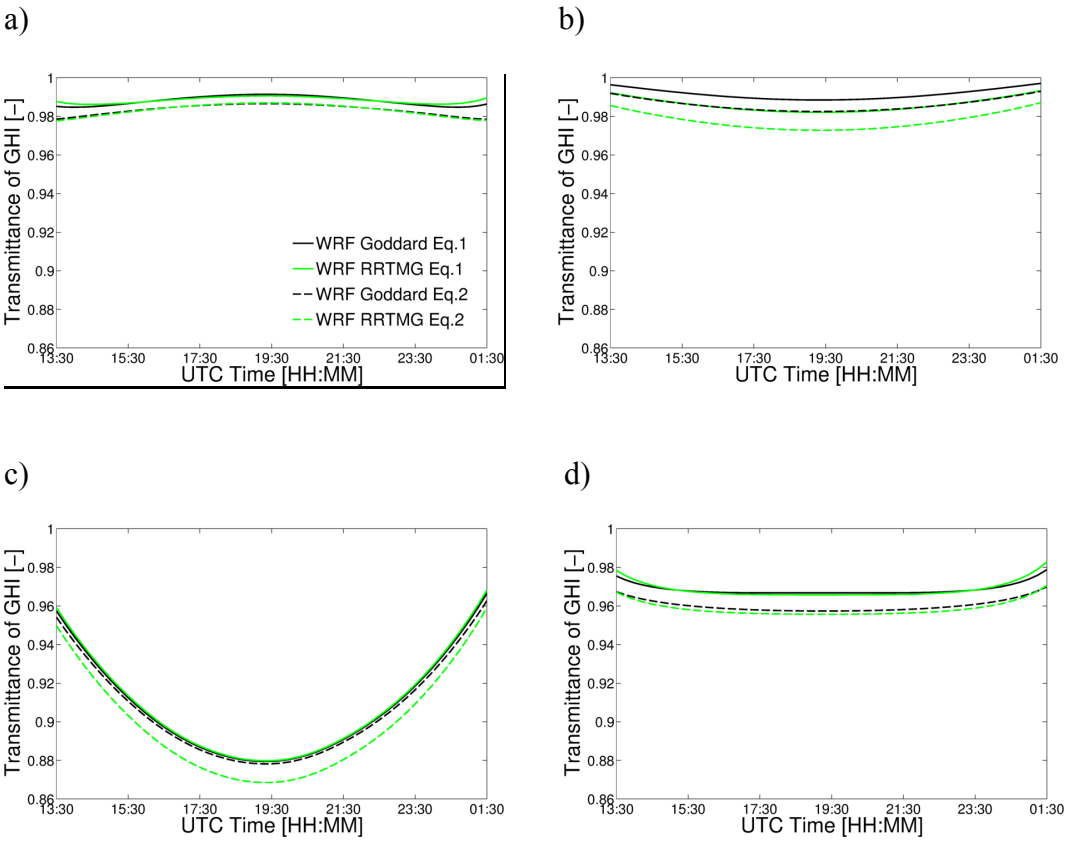

Figure 2.3: WRF Goddard and WRF RRTMG time series of T_X due to aerosols (a), ozone (b), water vapor (c) and Rayleigh scattering of other gases (d) at the grid point at 32.87 N, 117.25 W for June 10, 2013. Solid lines are computed using Eq. 2.1 and dashed lines are computed using Eq. 2.2. The variability in T_X due to water vapor is caused by change in simulated amount of water vapor during the day.

2.3.2. Influence of the delta-scaling approximation

The New Goddard SW overestimation of DNI (Figure 2.1b) can be broken down in a similar way as GHI. Although the same aerosol optical properties are input to both New Goddard and RRTMG SW, the values of DNI transmittance due to aerosols are significantly different (Figure 2.4a). The New Goddard SW scheme applies delta scaling to optical depth (Zeng et al. 1996) and uses scaled optical depth to calculate GHI and DNI transmittance. On the other hand, the RRTMG SW calculates GHI using scaled optical depth and partitions GHI into DNI and DIF using unscaled optical depth. The

delta scaling approximation assumes that scattered beams contained within the forward peak are not scattered at all, and those beams are added back to the original radiation field. Therefore, scaled optical depth is smaller than unscaled optical depth. According to Blanc et al. (2014), who reviewed multiple definitions of DNI in the literature, in the domain of numerical modeling of radiative transfer such as MODTRAN, SMARTS and libRadtran, DNI at the surface does not take into account the scattered photons that may reenter the beam. For this reason, direct transmittance in WRF Goddard 2 is modified using unscaled optical depth in order to be equivalent to RRTMG (Figure 2.4b).

a) b)

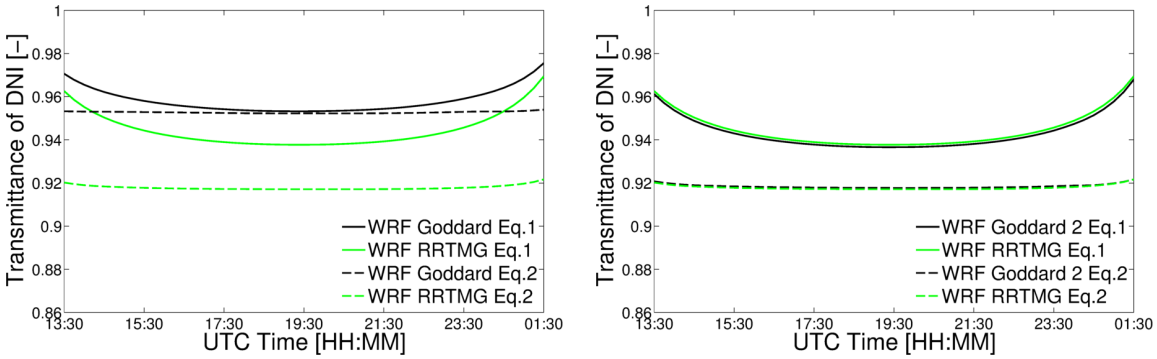

Figure 2.4: WRF Goddard (left) and WRF RRTMG time series of T_X of DNI due to aerosols at the grid point at 32.87 N, 117.25 W for June 10, 2013. The WRF Goddard 2 (right) uses unscaled optical depth to partition GHI into DNI and DIF. Note that WRF Goddard 2 here incorporated ozone and water vapor corrections (see Section 2.4).

2.3.3. Influence of model top pressure

In WRF, a model top is chosen at a discrete pressure level (here $p_{top} = 50$ hPa, consistent with the NAM) and the atmospheric constituents above that pressure level do not participate in radiative transfer. Therefore, Rayleigh scattering above the model top is neglected and it is necessary to analyze its impact. The overall atmospheric transmittance T due to Rayleigh scattering can be approximated by:

$$T = e^{-\overline{ry}\Delta p}, \tag{2.3}$$

where $\overline{ry}$ is the mean Rayleigh scattering coefficient and Δp is pressure difference between the ground and model top (p_{top} = 50 hPa). If Rayleigh scattering above model top were included, the transmittance should be $T' = e^{-\overline{ry}(\Delta p + p_{top})}$. The resulting relative change in transmittance due to Rayleigh scattering of the atmosphere above the model top can be calculated as

$$\frac{T'-T}{T} = \frac{e^{-\overline{ry}(\Delta p + p_{top})} - e^{-\overline{ry}\Delta p}}{e^{-\overline{ry}\Delta p}} = \frac{e^{-\overline{ry}\Delta p}\left(e^{-\overline{ry}p_{top}} - 1\right)}{e^{-\overline{ry}\Delta p}} = e^{-\overline{ry}p_{top}} - 1 = \left(e^{-\overline{ry}\Delta p}\right)^{\frac{p_{top}}{\Delta p}} - 1 = T^{\frac{p_{top}}{\Delta p}} - 1. \tag{2.4}$$

From Figure 2.3 we estimate the transmittance $T_{Rayleigh} \approx 0.96$ and $\frac{T'-T}{T}$ is approximately -0.2%. To reconfirm this, we have run WRF initialized from GFS with a p_{top} of 10 hPa and Rayleigh scattering increased by less than 1% corresponding to a change in transmittance of 0.04%. Similarly, a large amount of stratospheric ozone exists above 50 hPa. In Section 2.4.1, we will show that transmittance due to ozone is not sensitive to the missing ozone above the model top of 50 hPa.

2.4. Correcting Absorption of Ozone and Water Vapor Continuum in the New Goddard SW Scheme

2.4.1. Ozone Profiles in the New Goddard and RRTMG SW Schemes

The total amount of ozone within a vertical air column from the ground to TOA is defined as column abundance (Hewitt and Jackson 2009). Column abundance is reported in Dobson units (DU), which corresponds to the depth (in units of 10-5 m) that pure

ozone would have when compressed at standard temperature (273 K) and one atmosphere pressure (STP). The New Goddard SW scheme includes five vertical profiles of ozone for tropical (all year), mid-latitude (summer/winter) and arctic (summer/winter), which are selected based on the latitude of the center of the domain and the day of the year (Montornès et al. 2015). In the RRTMG, on the other hand, only one profile (RRTMG annual) representing an average of RRTMG summer and winter ozone profiles is utilized (Figure 2.5). Below model top pressure at 50 hPa is utilized (Figure 2.5b), the RRTMG annual shows a slightly higher ozone concentration than Goddard mid-latitude summer and Goddard tropical has the lowest ozone concentration. For our location in La Jolla, CA and the June day, the Goddard mid-latitude summer ozone profile should be used. However, we found a programming error that causes the variable center_lat, defined as the latitude of domain center to not be computed in the module_radiation_driver.F before input to module_ra_goddard.F. Therefore, center_lat =0 and the Goddard tropical ozone profile is always used independent of the location of the domain center, which results in underestimation of ozone and ozone absorption in the New Goddard SW scheme especially during winter. While the obvious correction would be to correctly compute center_lat[1], we applied the RRTMG annual ozone profile in the New Goddard SW scheme here to exclude the ozone concentration difference as a source of bias as we correct water vapor absorption in the next section. Figure 2.6 shows that the difference in transmittance between New Goddard SW and RRMTG SW has become $\Delta T_{X,2} < 0.14\%$.

[1] The programming error has been communicated to the WRF hosting team. It has been included into a the version 3.8.1 WRF release (http://www2.mmm.ucar.edu/wrf/users/wrfv3.8/updates-3.8.1.html).

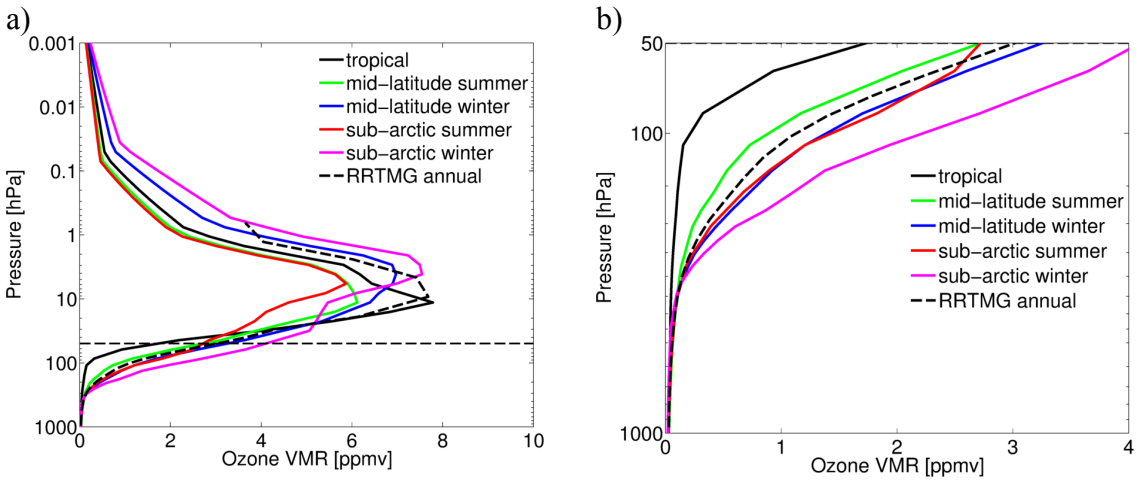

Figure 2.5: Ozone volume mixing ratio profile data in the New Goddard (solid lines) and RRTMG models (dashed lines). The horizontal dashed line indicates 50 hPa. The scaled column abundance of ozone from the ground to TOA (model top at 50 hPa) for New Goddard tropical, mid-latitude summer, mid-latitude winter, sub-arctic summer, sub-arctic winter and RRTMG annual are about 76 (55), 124 (103), 148 (125), 143 (125), 178 (153), 135 (111) DU.

The tropical profile selected by default in the New Goddard results in (unscaled) total ozone abundance from the ground to 50 hPa of about 63 DU while RRTMG (unscaled) total ozone abundance (from the ground to to 50 hPa) is about 173 DU (note that these numbers differ from the scaled values in the caption of Figure 2.5). Although (unscaled) total ozone abundance from the ground to TOA derived from the RRTMG ozone profile is more than 300 DU, the sensitivity of ozone absorption to missing ozone above the model top of 50 hPa is reduced by the scaling of the absorption coefficients as a function of pressure and temperature (θ). For ozone the scaling (Chou and Suarez 1999) follows:

$$O_3(p,\theta) = O_3'\left(\frac{p}{p_r}\right)^m [1 + 0.00135(\theta - \theta_r)], \quad (2.5)$$

where O_3' and O_3 are ozone before and after scaling, p_r and θ_r are reference pressure (300 hPa) and reference temperature (240 K), and m =0.8. As the effect of

temperature on scaling of ozone is weak, we ignore the temperature term in Eq. 2.5. For example if RRTMG annual profile is used, the scaled ozone abundance only increases from 111 DU to 135 DU when model top increases from 50 hPa to TOA. The corresponding change of total transmittance can be calculated similarly as Eq. 2.4 as $\frac{T'-T}{T} = \frac{T^{\frac{135}{111}}-T}{T} = T^{\frac{24}{111}} - 1 \approx -0.5\%$ (the transmittance $T_{O3} \approx 0.98$).

2.4.2. Water Vapor Continuum Absorption

The water vapor continuum is a component of water vapor absorption whose contribution varies smoothly from the visible to the microwave spectral regions (Shine et al. 2012). Feng et al. (2005) incorporated its absorption and that of a number of weak bands for water vapor and other atmospheric constituents, in the Fu-Liou solar radiation model using the correlated-k distribution method (CKD). This update increased the solar absorption from about 9% to 13% of the extraterrestrial value, mostly due to the water vapor continuum absorption. The original CKD water vapor continuum model (Clough et al. 1989, 1992) and its successor MT_CKD (Clough et al. 2005) have been widely adopted in many atmospheric radiative transfer models (Daniel 2004), including, particularly, the Rapid Radiative Transfer Model for Global Circulation Models (RRTMG) (Mlawer et al. 1997; Mlawer and Clough 1997, 1998). However, it has not been considered yet in the WRF's New Goddard SW scheme.

Table 2.3: The flux-weighted k-distribution function, Δg, in the near infrared and infrared regions. The parameter k is the absorption coefficient. The 'original' values are from Chou and Lee (1996) and used in the New Goddard SW scheme. The corrected values include water vapor continuum absorption and are recommended for use. Note that the sum of the original Δg must be equal to sum of the corrected Δg.

k-interval	k [g-1 cm2]	Δg (0.7 – 1.22 μm)		Δg (1.22 – 2.27 μm)		Δg (2.27 – 10.0 μm)	
		original	corrected	original	corrected	original	corrected
1	0.0010	0.20673	0.19310	0.08236	0.06924	0.01074	0.00310
2	0.0133	0.03497	0.05716	0.01157	0.01960	0.00360	0.00638
3	0.0422	0.03011	0.02088	0.01133	0.00795	0.00411	0.00526
4	0.1334	0.02260	0.02407	0.01143	0.01716	0.00421	0.00641
5	0.4217	0.01336	0.01402	0.01240	0.01118	0.00389	0.00542
6	1.3340	0.00696	0.00582	0.01258	0.01377	0.00326	0.00312
7	5.6230	0.00441	0.00246	0.01381	0.02008	0.00499	0.00368
8	31.620	0.00115	0.00163	0.00650	0.00265	0.00465	0.00346
9	177.80	0.00026	0.00101	0.00244	0.00282	0.00245	0.00555
10	1000.0	0.00000	0.00041	0.00094	0.00092	0.00145	0.00098

Chou and Lee (1996) developed a computationally efficient parameterization of water vapor absorption using the k-distribution method. The flux-weighted k-distribution function Δg_j is calculated as:

$$\Delta g_j = \sum_i (S_i \Delta \upsilon_i) f_i(k_j) / S_0, \tag{2.6}$$

where $S_i \Delta \upsilon_i$ is the extraterrestrial solar flux in the spectral interval i, υ is the wavenumber, $f_i(k_j)$ is the k-distribution function derived from a line by line method, k_j is the absorption coefficient, and S_0 is the total extraterrestrial solar flux. The values of Δg_j given in Table 1 of Chou and Lee (1996) and repeated in Table 2.3 in this paper are implemented in the New Goddard SW scheme. However, the embedded calculations of $f_i(k_j)$ by Chou (1992) using the HITRAN-92 spectroscopic database (Rothman et al. 1992) did not take into account absorption of the water vapor continuum. Tarasova and Fomin (2000) used the HITRAN-96 database together with the water vapor continuum model (Clough et al. 1989) to calculate $f_i(k_j)$. Since their Δg_j (Table 1 and Eq. 7 of

Tarasova and Fomin, 2000) is defined differently than in Eq. 2.6 here, the fractional solar flux (defined as S_j/S_0, where S_j is the extraterrestrial solar flux in spectral interval j) is used to convert Δg in Tarasova and Fomin (2000) to Δg as defined in Eq. 2.6. The corrected Δg given in Table 2.3 account for absorption due to both water vapor lines and continuum. The water vapor absorption is enhanced as more spectral regions correspond to larger values of absorption coefficient.

2.5. Clear-Sky Irradiance with the Corrected New Goddard Scheme and Discussion

The RRTMG ozone profile and the new parameterization of water vapor absorption including water vapor continuum are implemented in the corrected New Goddard SW scheme, which we named WRF Goddard 2. Figure 2.6 demonstrates that WRF Goddard 2 is in better agreement with WRF RRTMG. The transmittance $\tau_{X,2}$ at solar noon due to ozone and water vapor absorption are 0.974 and 0.870 in the corrected New Goddard SW scheme, and 0.973 and 0.868 in the RRTMG SW scheme, respectively. The GHI biases are reduced by 38% and 47% due to the ozone and water vapor corrections, respectively, compared with the original New Goddard SW scheme.

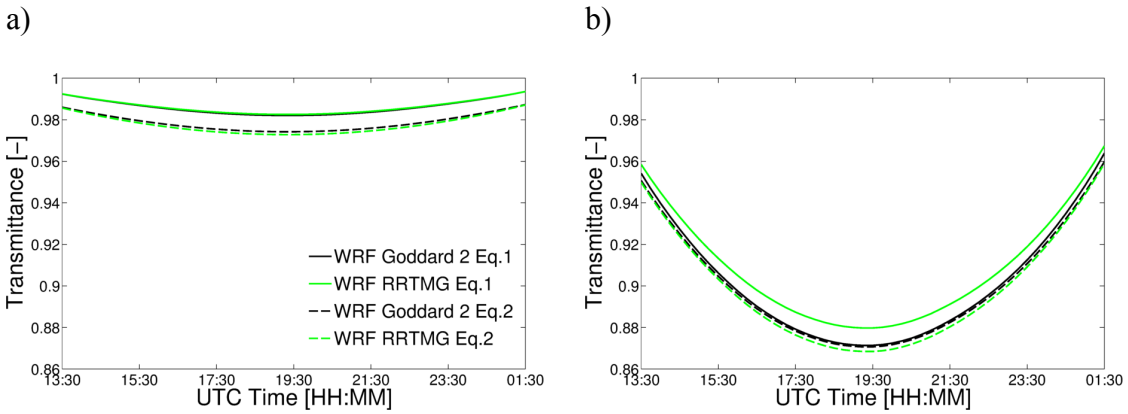

Figure 2.6: WRF Goddard 2 and WRF RRTMG time series of T_X due to ozone (a) and water vapor (b) at the grid point at 32.87 N, 117.25 W for June 10, 2013.

Figure 2.7 compares GHI, DNI and DIF between WRF and REST2 using simulation outputs from June 1 to June 10, 2013. For GHI and DNI WRF Goddard 2 achieves higher accuracies in terms of relative MAE and MBE (normalized by the mean REST2 value) than WRF Goddard. The increase in absorption decreases relative MBE for GHI from 3.0% to 0.8%. Relative MBE for DNI decreases from 7.7% to 0.5%, and relative MBE for DIF improves from -16.1% to 1.3%. While GHI and DNI are essentially bias-free across the entire range of irradiance values, diffuse is slightly overestimated at intermediate DIF values which correspond to medium to large solar zenith angles. While the relative MAE for DIF is significant, in clear skies diffuse contributes only about 10% to the GHI and the impact on GHI is therefore small.

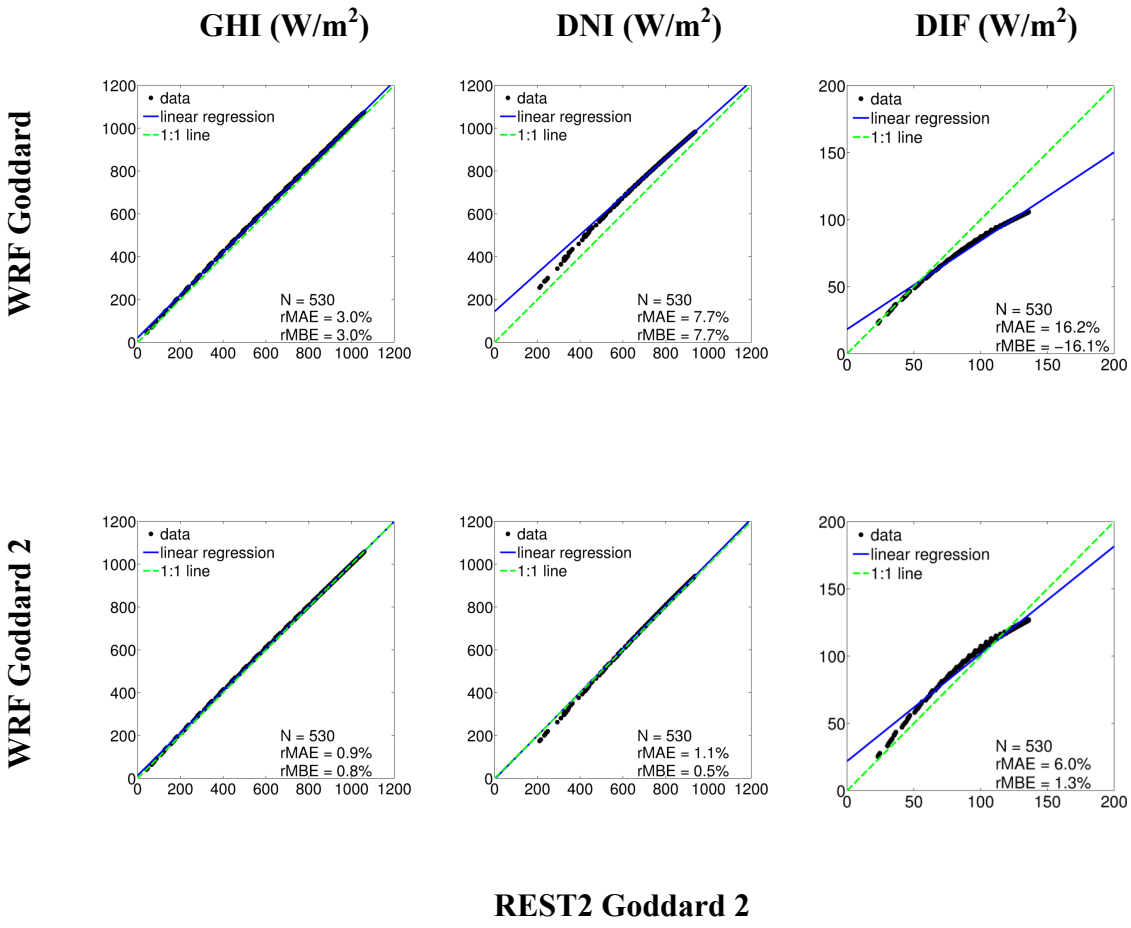

Figure 2.7: WRF Goddard (top row) and WRF Goddard 2 (bottom row) against REST2 Goddard 2 for GHI (column 1), DNI (column 2) and DIF (column 3, all in W m-2) at the grid point at 32.87 N, 117.25 W from June 1 to 10, 2013. The number of data points, relative mean absolute error and relative mean bias error are shown as N, rMAE, and rMBE. Solar zenith angles greater than 85° are omitted because the accuracy of the two-stream approximation in the New Goddard SW scheme decreases at large solar zenith angle.

2.6. Summary

The effects of different atmospheric constituents on the WRF's New Goddard SW clear-sky surface irradiance were analyzed. The comparison shows that an incorrect ozone profile and missing absorption of water vapor continuum in the New Goddard SW scheme are the leading sources of positive GHI biases while the atmospheric composition

is not a major source of error. The incorrect ozone profile was tracked down to a coding error related to the location of the domain center latitude which caused a tropical ozone profile, often with weaker ozone absorption than required, to be used by default everywhere. Use of the RRTMG ozone profile as well as the new parameterization of water vapor absorption including water vapor continuum allowed the corrected New Goddard SW scheme to compare favorably against REST2. The DNI and DIF biases were corrected by calculating direct irradiance transmittance using unscaled optical depth. The relative mean bias errors in GHI and DNI are around 1% and 0.5%. Overall, the methods presented here are useful tools for analyzing and correcting clear sky irradiance biases in other SW radiation schemes in NWP models.

Acknowledgements

Chapter 2, in full, is a reprint of the materials as it appears in Zhong, X., Ruiz-Arias, J. A., and Kleissl, J., 2016: Dissecting Surface Clear Sky Irradiance Bias in Numerical Weather Prediction: Application and Corrections to the New Goddard Shortwave Scheme. *Solar Energy*. The dissertation/thesis author was the primary investigator and author of this paper.

3. WRF Inversion Base Height Ensembles

In this chapter, a thermodynamic method was developed to modify the boundary layer temperature and moisture profiles to better represent the boundary layer structure in WRF. Firstly, we briefly describe meteorological conditions of 8 continuous marine layer days (Section 3.1). We hypothesize that underprediction of cloud cover in WRF (Section 3.2) over the California coastline is correlated with IBH biases. The MBL stratocumulus inland penetration is quantified using satellite irradiance data (Section 3.3.2) and the correlation between IBH derived from sounding data (Section 3.3.1) and MBL stratocumulus inland penetration is investigated in Section 3.4. We develop an IBH correction method in Section 3.5.1 and different IBH ensembles are run for eight June days. In Section 3.6, vertical temperature, moisture and relative humidity profiles of IBH ensembles are compared with sounding data. Also, the GHI forecasts of IBH ensembles are evaluated using irradiance measurements by both satellite and ground stations and persistence forecasts. Finally, we discuss our findings and conclude in Section 3.7. Section 3.8 validates the assumptions of well-mixed PBL and proposed a method to calculate IBH from surface measurements.

3.1. Meteorological Conditions for the Case Study

WRF (version 3.6) is initialized at 0 UTC and run for 26 hours each day from June 1 to June 8, 2013. The period was characterized by daily occurrence of MBL stratocumulus along the Southern California coastline. Starting on June 1, a trough of low pressure developed along the west coast and strengthened onshore flow. The stronger coastal eddy deepened the MBL and extended coastal clouds into the inland valleys. On

June 2 and 3, clouds persisted over much of coastal areas throughout the day and retreated from the inland valleys in the afternoon (see Figure 3.1a). For June 4, a high pressure system over the eastern Pacific expanded into northern and central California bringing about a warming trend. The low pressure system off the southern California coast moved slowly westward and continued to maintain the marine layer west of the mountains. The lowered IBH limited the inland extent of the MBL stratocumulus. Thus, on June 4 and June 5, clear skies prevailed over the inland region and even the coastal clouds cleared in the afternoon (see Figure 3.1b). On June 6, the low pressure system that moved westward moved back eastward and brought cooling inland. As a result, the MBL stratocumulus spread into the inland valleys in the mornings and retreated toward the coast through the early afternoon.

a) b)

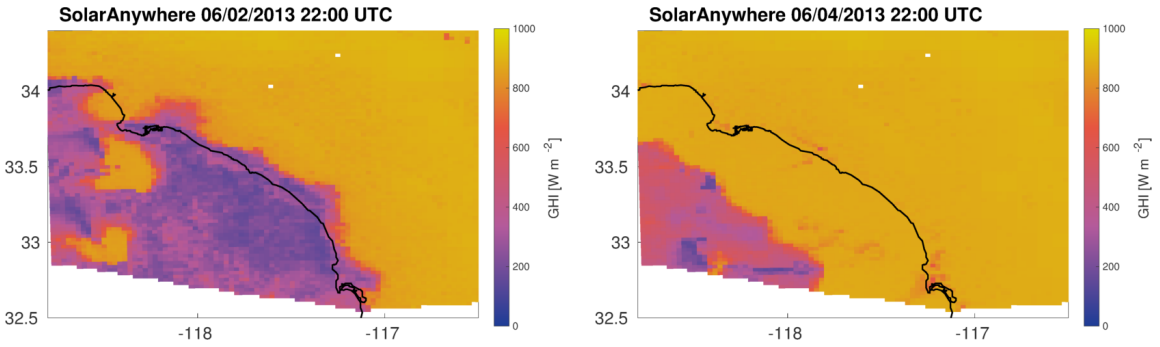

Figure 3.1: Spatial map of satellite GHI (SolarAnywhere) for two selected days at 22 UTC (14 PST) over Southern California. The coastline is in black and the spatial extent of the map is about 210 x 210 km. The left graph shows a scenario with overcast conditions at the coast throughout the day which occurred on June 3, 6, 7 and 8. The right graph shows a scenario where clouds had burned off during the morning; similar conditions were observed on June 1 and 5.

3.2. WRF Model Setup

As shown in Figure 3.2, the WRF model was configured with two nested domains with horizontal grid spacing of 12.5 km (domain 1) and 2.5 km (domain 2) centered at the University of California, San Diego, (32.88° N, 117.24° W). All variables are output every 15 min. North American Model (NAM) data were used for initial and boundary conditions. Following López-Coto et al. (2014) who analyzed 72 physics model combinations in the same region, we selected the physics parameterizations that are most accurate in irradiance and cloud forecasting: Morrison double-moment scheme for microphysics (Morrison et al. 2009), Mellor-Yamada Nakanishi and Niino Level 2.5 for PBL mixing (MYNN, Nakanishi and Niino, 2006), Noah land surface model (Ek et al. 2003), New Simplified Arakawa-Schubert for cumulus (NSAS, Han and Pan, 2011), and New Goddard (Chou and Suarez 1999) with Rayleigh scattering correction (Zhong et al. 2016) for both longwave and shortwave radiation. For the inner domain, the cumulus parameterization is turned off since the fine grid spacing ($\Delta x \leq 4$ km) explicitly resolves convection (Done et al. 2004).

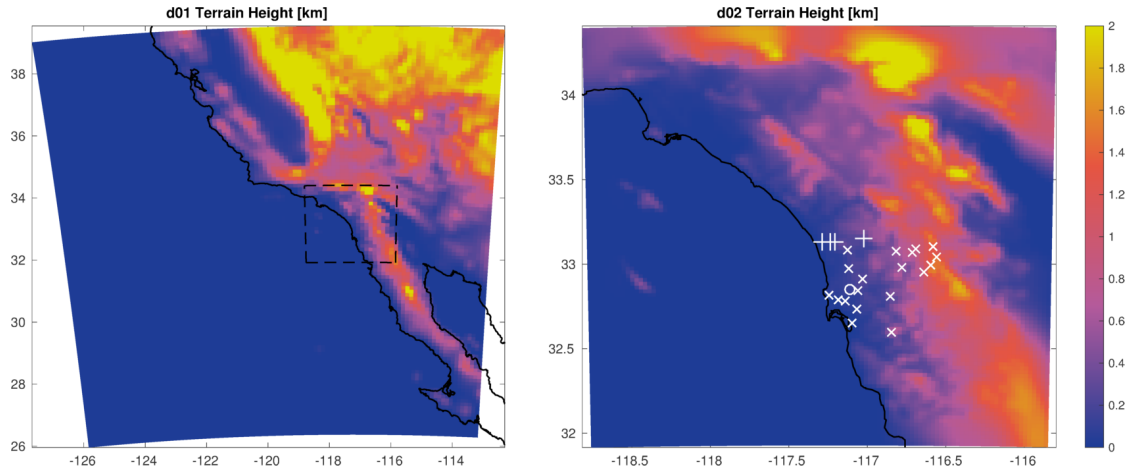

Figure 3.2: Digital elevation data of two nested WRF domains (left is domain 1 and right is domain 2) with four SDG&E pyranometer stations (plus), Miramar (NKX) radiosounding station (circle), and other SDG&E surface stations (x) overlaid. The color bar shows terrain elevation in km and the axis show latitude in degrees North and longitude in degrees East. The dashed line box in domain 1 indicates the nested domain 2.

3.3. Data

3.3.1. Radiosondes

Radiosondes are carried by weather balloons to measure vertical profiles of altitude, pressure, temperature, relative humidity, and wind. Due to geographical proximity to the area of interest, measurements from the sounding sites at San Diego (NKX: 32.88° N, 117.24° W) and Vandenberg (VBG: 34.75° N, 120.56° W) are used to determine the temperature inversion base height (IBH), inversion top height, and inversion strength. IBH and inversion top height are heights at the base and top of the inversion and inversion strength is the temperature difference between the top and bottom of the inversion layer. The temperature inversion below 3 km with maximum inversion strength is considered, consistent with Iacobellis and Cayan (2013). Also, inversions with inversion strength less than 3 K are ignored.

3.3.2. SolarAnywhere Data

SolarAnywhere (SAW, 2016) solar irradiance data is developed by Clean Power Research. Cloud indices derived from the Geostationary Operational Environmental Satellite (GOES) images are used to modulate a clear sky irradiance model (Perez et al. 2002). Jamaly and Kleissl (2012) concluded that MBE of SAW data is 18.1 W m^{-2} by validating SAW data against ground measurements in California.

In this work, SAW data at a horizontal resolution of 0.02° and temporal resolution of 30 min are interpolated spatially using nearest neighbor interpolation onto the grid of the WRF inner domain.

3.3.3. Ground Measured GHI Data

Throughout San Diego County, San Diego Gas & Electric (SDG&E) operates a pyranometer network with 55 stations measuring GHI using Licor Li-200 photodiode pyranometers. A shading analysis motivated removal of stations shaded by nearby structures. The stations listed in Table 3.1 provide high data quality and are used for evaluating WRF forecasts.

Table 3.1 Geographical information on SDG&E stations used for evaluating WRF forecasts (rows 2-5 of PWS1, PWS4, PWS6, and ESC) and SDG&E weather stations used for creating surface sounding in Appendix B (rows 6-24).

Station Name	Latitude (°)	Longitude (°)	Elevation (MSL m)
PWS1	33.12	-117.29	85
PWS4	33.14	-117.24	143
PWS6	33.13	-117.2	165
ESC	33.16	-117.03	315
NAT	32.65	-117.10	4
MVN	32.78	-117.14	63
TCN	32.79	-117.18	83
MSD	32.81	-117.24	113
CHO	32.74	-117.07	137
RPQ	32.97	-117.12	253
MTL	32.84	-117.06	275
SYC	32.91	-117.03	316
OLV	33.08	-117.13	356
CST	32.81	-116.85	453
BRM	32.98	-116.78	587
SSO	33.07	-116.81	712
DYE	33.07	-116.71	914
WSY	33.09	-116.69	1003
OTM	32.60	-116.84	1024
SIL	32.95	-116.64	1084
LCM	33.00	-116.60	1457
HRP	33.04	-116.56	1482
VCM	33.10	-116.58	1571

3.4. WRF IBH Biases and Implications

The WRF MYNN scheme determines the IBH height using a hybrid technique, which combines the 1.5-theta-increase method (Nielsen-Gammon et al. 2008; Hu et al. 2010) and the turbulent kinetic energy (TKE) method. The 1.5-theta-increase method defines PBL height as the level at which the virtual potential temperature first exceeds the minimum virtual potential temperature within the PBL by 1.25 K over land or 0.75 K

over ocean. The TKE-based method estimates PBL height at which TKE decreases to be less than 1/20 of maximum TKE within the PBL. However, virtual potential temperature is not conserved within the cloud layer in the PBL (Ghonima et al. 2016b), which leads to underestimation in PBL height. Following Ghonima et al. (2016), we replaced virtual potential temperature with liquid virtual potential temperature to calculate IBH correctly. Since IBH is only a diagnostic parameter in the MYNN scheme, the simulation results are not affected.

As demonstrated in Figure 3.3, WRF underpredicts 12 UTC IBH by approximately 200 m at NKX and 270 m at VBG on average compared with sounding measurements. IBH biases vary spatially and temporally. As detailed in the introduction, IBH biases can be attributed to the biases inherited from NAM and insufficient vertical mixing produced by WRF PBL schemes.

Figure 3.4 illustrates for one day how the IBH and coastal topography interact to limit cloud inland penetration. Since the IBH (black line) controls the stratocumulus cloud top height (red dashed line), the MBL stratocumulus cannot penetrate into the region where the ground elevation is higher than IBH. To further demonstrate the correlation between IBH and inland penetration of MBL stratocumulus with a larger dataset, the inland penetration of MBL stratocumulus were quantified in Figure 3.5 by the highest ground elevation of cloudy pixels at the cross section of NKX sounding station (see Figure 3.4 for an example). The coast pixels were classified as cloudy pixels if the ratio of SolarAnywhere GHI to the clear sky GHI, also called clear sky index kt, was smaller than 0.7. kt was computed from clear sky GHI using the Ineichen model (Ineichen and Perez 2002; Ineichen 2008) with monthly climatological Linke turbidity

from the Solar radiation Data (SoDa, 2012). The IBH were determined from radio soundings at 12 UTC. Since the sun rises at about 1245 UTC, SolarAnywhere at 1200 UTC cannot be used for cloud detection. Therefore, SolarAnywhere data at 1300 and 1330 UTC are used for this inland cloud penetration analysis, although soundings occur at 1200 UTC. The temporal variability in IBH over 1.5 hours is negligible.

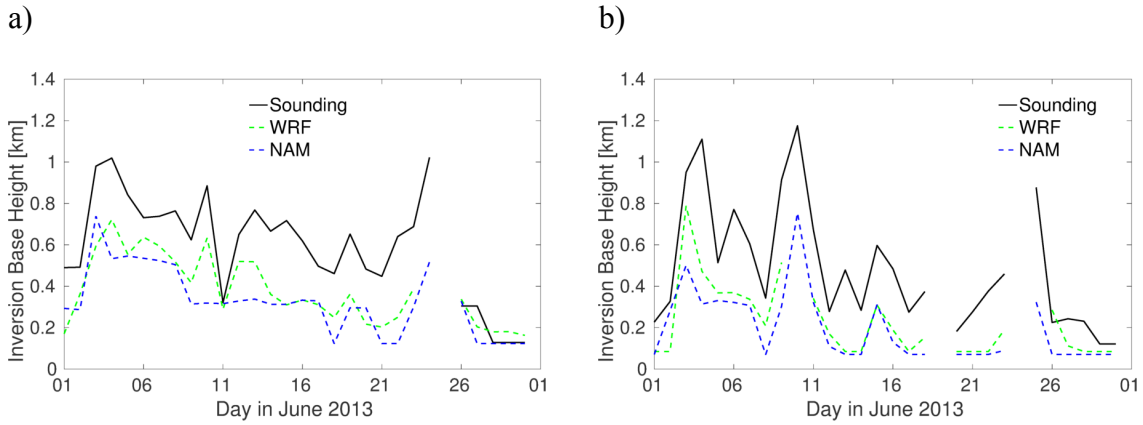

Figure 3.3: a) Inversion base height derived from 12 UTC WRF, NAM, and radiosonde profiles at NKX (a) and VBG (b) for every day in June, 2013 (30 data points). For June 25, 2013 at NKX and June 19 and 24 at VBG, the inversion base height is not specified as multiple inversions are observed and maximum inversion strength is less than 3 K.

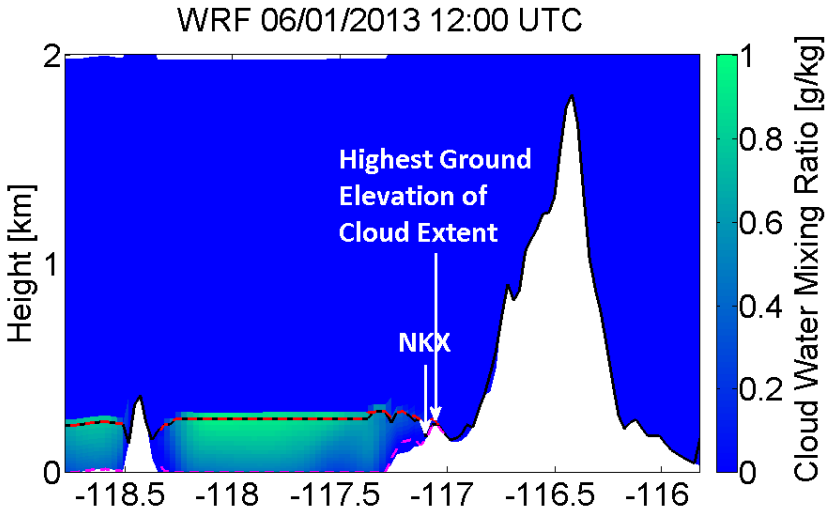

Figure 3.4: WRF cloud water mixing ratio (colorbar) at a west-east cross sections (x axis is Longitude in degrees) at NKX on June 1, 2013 at 12 UTC. Black, red and magenta lines indicate WRF IBH, cloud top and base height. NKX IBH was measured as 980 m on this day which based on geometrical arguments would have allowed farther inland penetration.

Figure 3.5 illustrates the positive correlation between sounding IBH and MBL stratocumulus inland penetration, consistent with Iacobellis and Cayan (2013). Therefore, when WRF underpredicts IBH, cloud cover over coastal land is also likely to be underpredicted. Traditional data assimilation techniques such as 3DVAR can be used to improve initial conditions, but the scarcity of vertical atmospheric profile measurements as well as the large biases of WRF forecasts (Figure 3.3a) make traditional data assimilation less effective than in other applications. Therefore, to better represent the IBH, we developed a method to modify the boundary layer temperature and moisture profiles as detailed in the next Section. As WRF often underpredicts IBH (see Figure 3.3), increasing IBH through the methods presented in the following section is expected to promote larger inland extent of MBL stratocumulus.

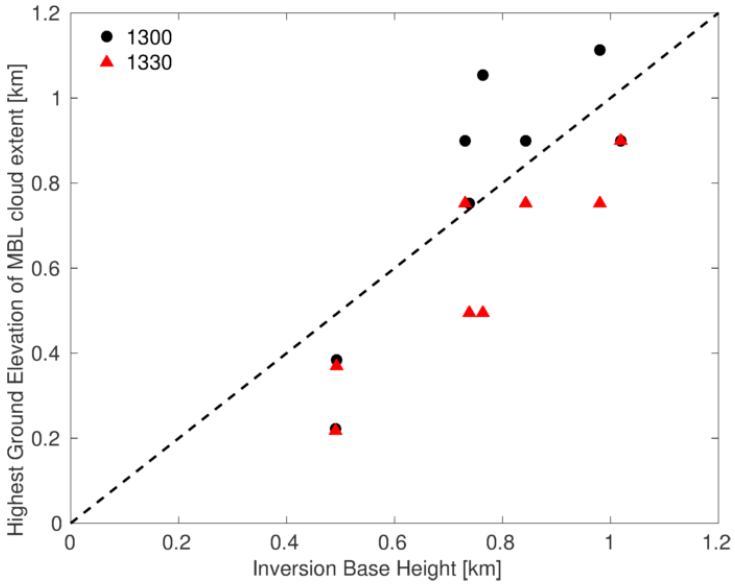

Figure 3.5: Relationship between NKX sounding inversion base height measured at 12 UTC and the highest ground elevations of SolarAnywhere MBL stratocumulus extent over land at 1300 (black circles) and 1330 (red triangles) UTC for June 1 to June 8, 2013. The dashed line indicates 1:1 line.

3.5. Methodology

3.5.1. Inversion Base Height Correction Method

According to the meteorological factors causing the inversion, low level inversions can be classified into two types: radiation (or surface) inversion and subsidence inversion (Iacobellis et al. 2009). Subsidence inversions develop when an upper layer of air is compressed and heated by increase in pressure as a result of subsiding air. Subsidence inversions are common over the subtropical oceans and the California coast and play a major role in stratocumulus formation and permanence. The IBH correction method targets these subsidence inversions. Radiation inversions typically develop during clear nights when a layer of air in contact with colder ground is cooled radiatively. Radiation inversions do not play a major role in stratocumulus formation, but are prevalent (and overestimated) in WRF simulations due to underprediction of cloud

cover. When subsidence inversions are accompanied with weak radiation inversions, only subsidence inversions are modified. Radiation inversions are only modified when radiation inversions are the only inversion present.

The IBH correction method is designed to respect the following principles: (i) adjust only columns with a low (under 3 km) inversion, (ii) do not adjust the temperature profile below the original inversion base, (iii) maintain the strength and depth of the inversion and temperature and water vapor gradients in the inversion layer, and (iv) avoid numerical instability. The motivations for these principles are as follows: (i) Only modify MBL inversions as other inversions are not related to stratocumulus. (ii, iii) Create a controlled experiment where the only major change is the IBH, while as much as possible of the original profiles is preserved. The procedure is illustrated for an increase in IBH of $\Delta h = 200$ m in Figure 3.6.

The new inversion base (z_{base}^{new}) and top (z_{top}^{new}) are determined as the model levels which are the closest to $z_{base}^{old} + \Delta h$ and $z_{top}^{old} + \Delta h$, respectively. In the example case, the inversion base and top height change at the grid point at 32.86 N and 117.10 W are 176 and 157 m respectively instead of exactly 200 m because of uneven vertical grid spacing in WRF. For the same reason, the change in inversion base and top height is not constant throughout the domain (Figure 3.6 e,f). The temperature profile below the original inversion base and above the new inversion top remains the same while temperature between the original inversion base and new inversion top is updated using the set of equations:

$$T^{new} =$$

$$\begin{cases} T^{old}, & z \le z_{base}^{old} \\ \left.\begin{matrix} T^{old}(z_{base}^{old}) - \Gamma_{dry} \times (z - z_{base}^{old}), air\ is\ not\ saturated \\ T^{old}(z_{base}^{old}) - \Gamma_{moist} \times (z - z_{base}^{old}), air\ is\ saturated \\ iterate, air\ is\ conditionally\ unstable \end{matrix}\right\}, & z_{base}^{old} < z \le z_{base}^{new} \\ T^{old}(z_{base}^{old} + z - z_{base}^{new}) - \left(T^{old}(z_{base}^{old}) - T^{new}(z_{base}^{new})\right), & z_{base}^{new} < z \le z_{top}^{new} \\ T^{old}, & z > z_{top}^{new} \end{cases} \quad (3.1)$$

T^{old} and T^{new} are the original and updated temperature, and Γ_{dry} and Γ_{moist} are the dry and moist adiabatic lapse rates. Between the original and new inversion base, the temperature is updated following either the dry or moist adiabatic temperature lapse rate depending on whether air is saturated or not. However, if the atmosphere is conditionally unstable the lapse rate falls between dry adiabatic and moist adiabatic. In that case, the temperature is calculated by iteratively solving temperature, water vapor mixing ratio (Q_v), cloud water mixing ratio (Q_c) for: (i) constant liquid water potential temperature throughout the PBL; (ii) constant total water mixing ratio, defined as sum of water vapor and cloud water mixing ratio ($Q_t = Q_v + Q_c$) and discussed in more detail in Appendix A; (iii) $Q_v = Q_s$, the saturation water mixing ratio, which is computed using the Clausius-Clapeyron equation based on T^{new} and pressure.

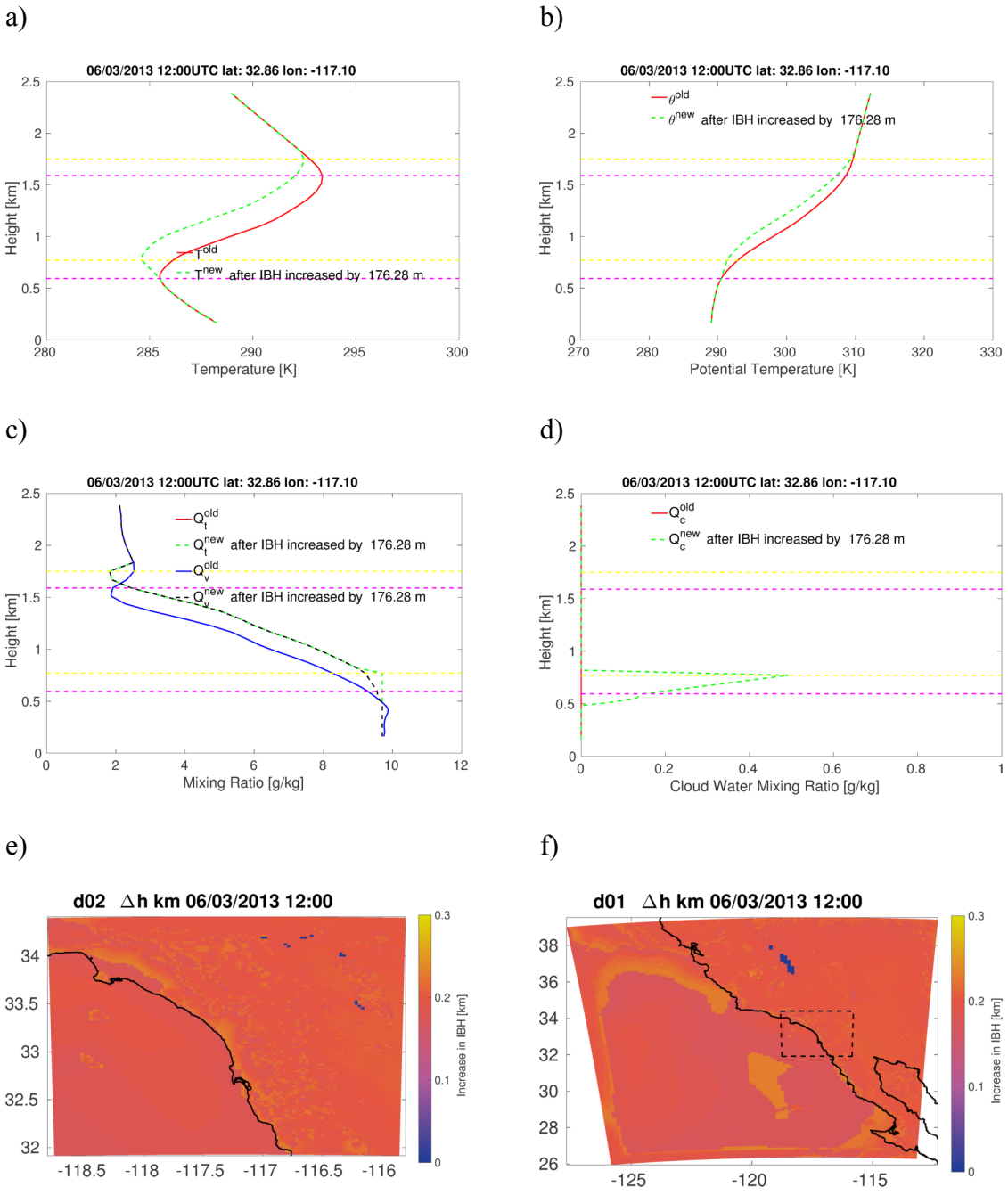

Figure 3.6: Intercomparison of temperature (a), potential temperature (b), Q_t and Q_v(c), and Q_c (d) before and after IBH was increased by $\Delta h = 200$ m for a grid point near the Miramar sounding station. (e) and (f) show spatial maps of IBH increase in km for the two WRF domains. Actual Δh is spatially variable, because the inversion can only exist at discrete vertical grid points. The dashed purple and yellow lines in a, b, c and d indicate the original and new inversion base and top. The dashed line box in domain 1 indicates the nested domain 2.

The temperature at the inversion base decreases to $T^{new}(z_{base}^{new})$ as the inversion base increases from z_{base}^{old} to z_{base}^{new}. If the temperature above the new inversion base were not changed, the inversion strength would be changed as a result of increase in the temperature gradient at the inversion base. To avoid unintended consequences such as changes to the entrainment which depends on the temperature gradient within the inversion, the temperature profile within the old inversion layer is shifted to the new inversion layer so that difference between $T^{new}(z = z_{base}^{new} + \Delta z)$ within the new inversion layer and $T^{new}(z_{base}^{new})$ is the same as the difference between $T^{old}(z_{base}^{old} + \Delta z)$ within the original inversion layer and $T^{old}(z_{base}^{old})$. Because of nonuniform vertical spacing, $T^{old}(z_{base}^{old} + \Delta z)$ is interpolated using T_2 and T_1 at height z_2 and z_1 of the two vertical levels which are the closest to $z_{base}^{old} + \Delta z$:

$$T^{old}\left(z_{base}^{old} + \Delta z\right) = T^{old}(z_{base}^{old} + z - z_{base}^{new}) = \frac{T_2 - T_1}{z_2 - z_1}[z - z_1] + T_1 \qquad (3.2)$$

As the temperature inversion base is also often accompanied by a large gradient of moisture, maintaining the original moisture profile is not physically reasonable. To extrapolate the water vapor and liquid water between original and new inversion base, we assume a well-mixed PBL, i.e. the total water mixing ratio is constant from the surface to the inversion base and is referred to as $\overline{Q_t}$.

Water vapor and cloud water above the new inversion top remain the same while water vapor and cloud water mixing ratio below the new inversion top, Q_v^{new} and Q_c^{new}, are updated using:

$$(Q_v^{new}, Q_c^{new}) =$$

$$\begin{cases} \left.\begin{matrix}(\overline{Q_t}, 0), air\ is\ not\ saturated \\ (Q_s, \overline{Q_t}\text{-}Q_s), air\ is\ saturated \\ iterate, air\ is\ conditionally\ unstable\end{matrix}\right\}, & z \le z_{base}^{new} \\ \left(Q_v^{old}(z_{base}^{old} + z - z_{base}^{new})\text{-}\left(Q_v^{old}(z_{base}^{old})\text{-}Q_v^{new}(z_{base}^{new})\right), 0\right), & z_{base}^{new} < z \le z_{top}^{new} \\ (Q_v^{old}, Q_c^{old}), & z > z_{top}^{new} \end{cases} \quad (3.3)$$

where Q_v^{old} and Q_c^{old} are original water vapor and cloud water mixing ratio, respectively. Analogous to $T^{old}(z_{base}^{old} + \Delta z)$, $Q_v^{old}(z_{base}^{old} + \Delta z)$ within the original inversion is calculated using Q_{v1} and Q_{v2} at height z_2 and z_1:

$$\mathrm{Q_v^{old}}\left(\mathrm{z_{base}^{old}} + \Delta \mathrm{z}\right) = \mathrm{Q_v^{old}}(\mathrm{z_{base}^{old}} + \mathrm{z} - \mathrm{z_{base}^{new}}) = \frac{\mathrm{Q_{v2}} - \mathrm{Q_{v1}}}{\mathrm{z_2} - \mathrm{z_1}}[\mathrm{z} - \mathrm{z_1}] + \mathrm{Q_{v1}} \quad (3.4)$$

Figure 3.6 e and f show an example of the IBH changes throughout both WRF domains.

3.5.2. Setup of the numerical experiments

Since Figure 3.5 suggests that the IBH is positively correlated with MBL stratocumulus inland penetration, different increases in IBH (Δh) are expected to generate different solar forecasts. Moreover, the IBH biases vary from day-to-day and spatially as shown by Figure 3.3. Therefore, we designed numerical experiments using different values of Δh (Table 3.2), which are named IBH ensembles. Since the IBH bias at 12 UTC in Figure 3.3 typically ranges from 100 to 400 m, the IBH is increased by 200 and 400 m for sensitivity studies. An additional run with $\Delta h = 0$ allows assessing whether modifying the initial total water distribution below z_{base}^{old} alone confounds the results. Lastly, a run with $\Delta h = 600$ m is added to demonstrate the effects of increasing IBH beyond what is suggested by IBH observations.

The impact of IBH change is likely to diminish over time similarly to cloud data assimilation (Mathiesen et al. 2013). To test the persistence of IBH changes, the IBH correction method is applied at 6 and 12 UTC, respectively. For 6 (or 12) UTC ensembles, simulations were initialized at 0 UTC and run until 6 (or 12) UTC, and temperature and moisture in restart files were modified by the method described in Section 3.5.1. The modified restart files were used to restart the simulations.

Table 3.2 Overview of the numerical experiments: Name convention takes into account the IBH increase and the time when the IBH correction is applied.

Time	$\Delta h = 0$ m	$\Delta h = 200$ m	$\Delta h = 400$ m	$\Delta h = 600$ m
6 UTC	IBH06d0	IBH06d200	IBH06d400	
12 UTC	IBH12d0	IBH12d200	IBH12d400	IBH12d600

3.5.3. Validation method and error metrics

Spatial errors distributions were quantified using the SolarAnywhere GHI dataset. The mean absolute errors (MAE) of both GHI and kt were computed at temporal resolution of 30 minutes from 6 PST to 18 PST of each day from June 1 to June 8, 2013 using

$$MAE = \frac{1}{N}\sum_{i=1}^{N}\left|x_i - x_i^{obs}\right|, \tag{3.5}$$

where x_i and x_i^{obs} are forecast outputs and satellite or ground observations, respectively. Using kt errors to evaluate model irradiance forecasts removes the time of day dependence due to the solar irradiance diurnal cycle.

The mean bias errors (MBE) of both GHI and kt were computed as a function of time of day for the coastal marine layer region which is most affected by MBL stratocumulus. The coastal marine layer region is delineated as in Yang and Kleissl

(2016) as the region where ground elevation is lower than 375 m MSL and June monthly mean observed kt is smaller than 0.92.

$$MBE = \frac{1}{N}\sum_{i=1}^{N}\left(x_i - x_i^{obs}\right) \quad (3.6)$$

Lastly, time series of forecast GHI were compared with ground stations measurements from SDG&E stations and GHI MBE and MAE were computed.

3.5.4. MOS correction

Since stratocumulus are often only present for a few hours in the mornings while the rest of the day is clear, daily error metrics can be disproportionally influenced by WRF clear sky biases. After applying the New Goddard shortwave radiation scheme in WRF (Zhong et al. 2016) residual clear sky biases compared with SDG&E ground stations are removed through a model output statistics (MOS) correction (Yang and Kleissl 2016a). Localized MOS correction functions were derived for the baseline WRF based on SDG&E ground observations during clear sky time periods at each of the 4 stations. Since the clear sky biases mostly depend on the shortwave radiation scheme and not the IBH correction, the baseline WRF MOS correction was applied for all other IBH ensembles.

3.6. Results and Discussions

This section is divided into three subsections based on the source of measurement used for evaluating IBH ensembles. First, vertical profiles of WRF forecasts with and without IBH correction are compared against sounding data to understand how well the IBH corrections persist through the day. The other two subsections present solar forecast errors of WRF forecasts against ground station measurements and SolarAnywhere.

3.6.1. WRF vertical profiles against soundings

Figure 3.7 illustrates the time evolution of temperature, water vapor mixing ratio, and relative humidity difference between baseline WRF (row 1), IBH06d400, and IBH12d400. The IBH correction improves the agreement of IBH06d400 and IBH12d400 with soundings. The IBH06d400 correction is not as persistent dropping from 1,035 m at 0415 PST to 822 m at 0800 PST on June 3, 2013. On the other hand, the IBH12d400 correction holds steady at IBH of about 1,000 m until 1200 PST maintaining an accurate IBH throughout the most critical period for intra-day solar forecasts. As shown in Figure 3.7 b, e, and h, the decrease in IBH is also accompanied by a decrease in moisture and relative humidity in the boundary layer. Therefore, the difference in persistence of the IBH correction likely explains why clouds in IBH6d400 dissipate at around 8 PST while clouds dissipate after 10 PST in IBH12d400.

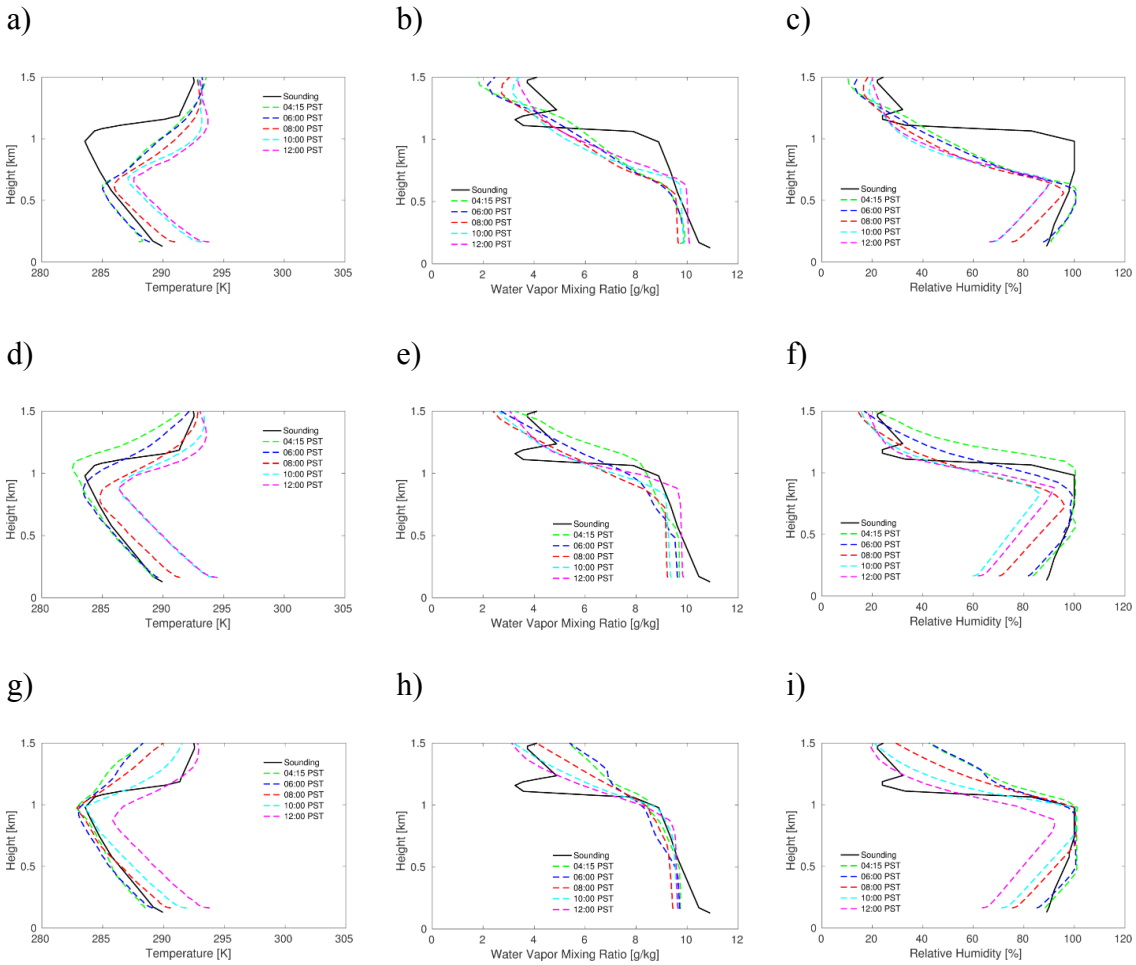

Figure 3.7: Intercomparisons of vertical profiles of temperature (column 1), water mixing ratio (column 2), and relative humidity (column 3) between sounding at 12 UTC (4 PST) and WRF forecasts (row 1 is baseline WRF, row 2 is IBH06d400, row 3 is IBH12d400) at different times on June 3, 2013.

3.6.2. Analysis for different days

Figure 3.8 compares the GHI time series of an inland (ESC, 315 m MSL) and a coastal station (PWS4) for June 2 and 4 as well as the average from June 1 to June 8. June 2 was an extreme marine layer day with NKX IBH of 492 m and far inland cloud extent in the morning and coastal cloudiness all day (Figure 3.1a, Figure 3.9). June 4 (with NKX IBH of 1019 m) was a more typical day when clouds burned off at the coast in the late morning. For PWS4, clouds are correctly predicted by baseline WRF in the

morning on June 2, but they dissipate much faster than in the observations. IBH ensembles, especially IBH12d400 and IBH12d600, significantly reduce GHI biases and resemble the observed diurnal evolution of GHI. But on June 4, the 12 UTC ensembles overpredict clouds until 13 PST. For ESC, most forecasts are false negatives (clouds exist, but are not forecasted) except for IBH12d400 and IBH12d600. For IBH12d400 clouds were too thin and evaporated too quickly, and the opposite occurred for IBH12d600. Figure 3.8 demonstrates that the inability of WRF to predict clouds at ESC is closely associated with WRF IBH biases.

Figure 3.9 and Figure 3.10 present the GHI MBE and kt MAE of the coastal marine layer region as a function of time of day. The baseline WRF persistently overpredicts irradiances and underpredicts cloud cover in the morning and the GHI MBE (kt MAE) can be as large as 400 W/m^2 (0.6). The errors drop significantly as clouds dissipate or thin in the afternoon. All five IBH ensembles with nonzero Δh improve on baseline WRF, and the 12 UTC ensembles stands out reducing GHI MBE (kt MAE) to within -100 to 100 W/m^2 (0.1 – 0.2). Exceptions are June 1 and 8, when all IBH ensembles underpredict irradiance and thus have larger MAE. IBH12d600 performs the best during morning time for some days (as shown in Figure 3.9 and Figure 3.10). However, IBH12d600 also develops overly thick clouds due to overly large increase in IBH and GHI are underpredicted and clouds dissipate too late, for example around 1000 PST on June 4.

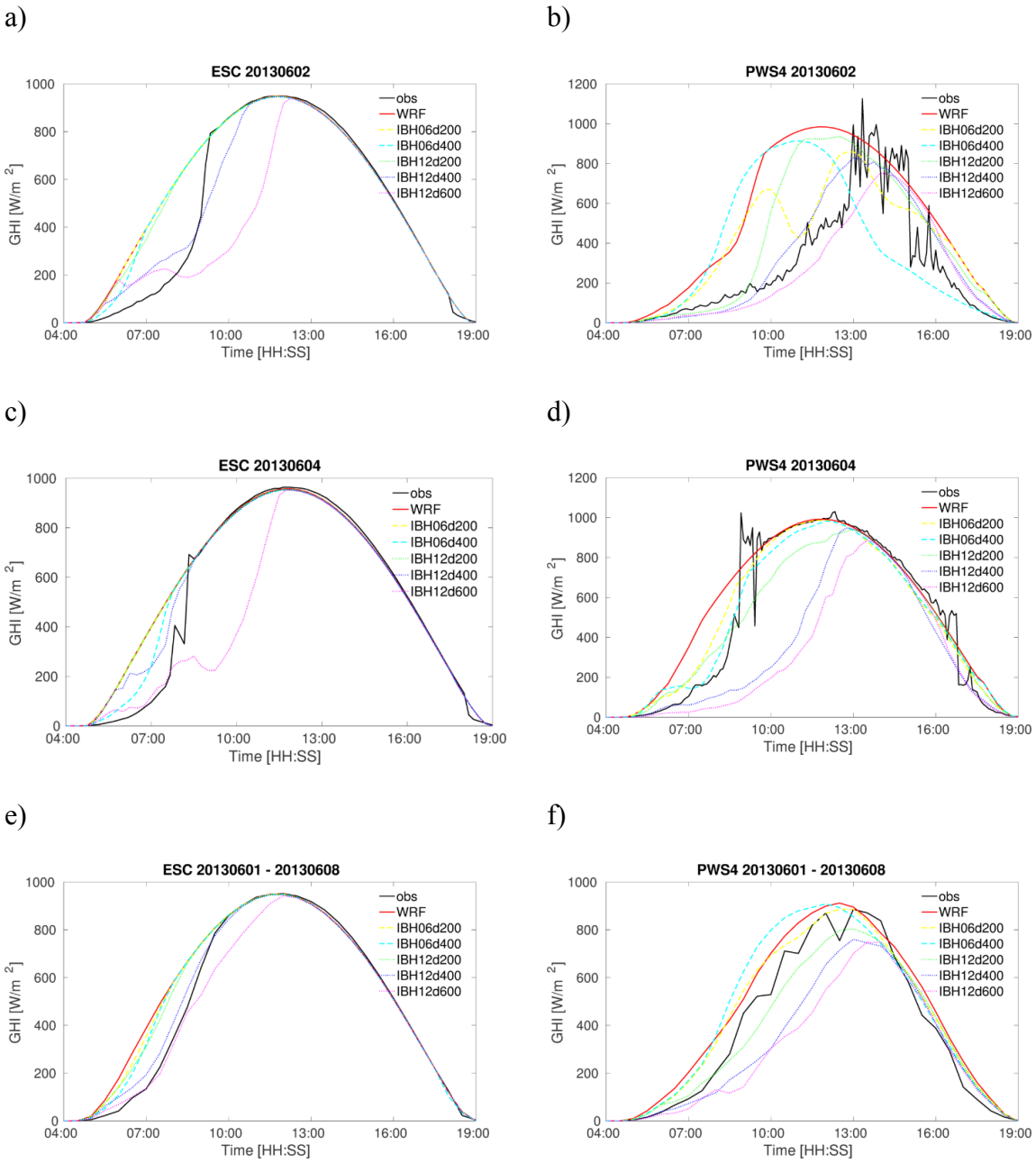

Figure 3.8: GHI time series at ESC (a, c, e) and PWS4 (b, d, f) stations for June 2 (row 1) and June 3 (row 2), 2013 and average from June 1 to June 8, 2013 (row 3).

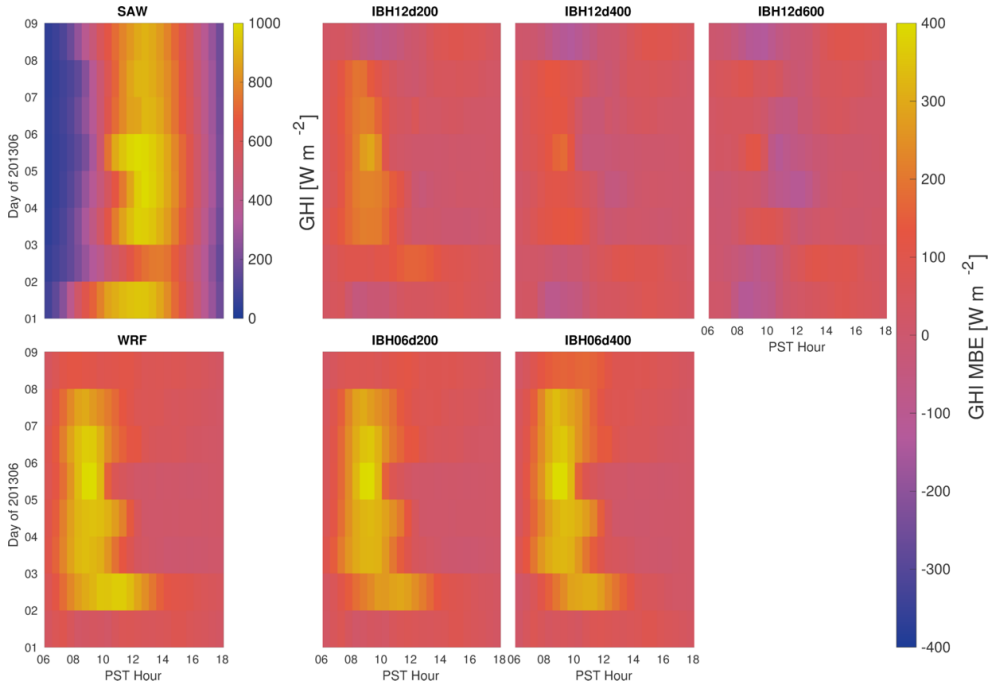

Figure 3.9: Time of day dependence of SolarAnywhere GHI and GHI MBE of the baseline WRF simulation and selected IBH ensembles compared to SolarAnywhere data spatially averaged over the coastal marine layer region.

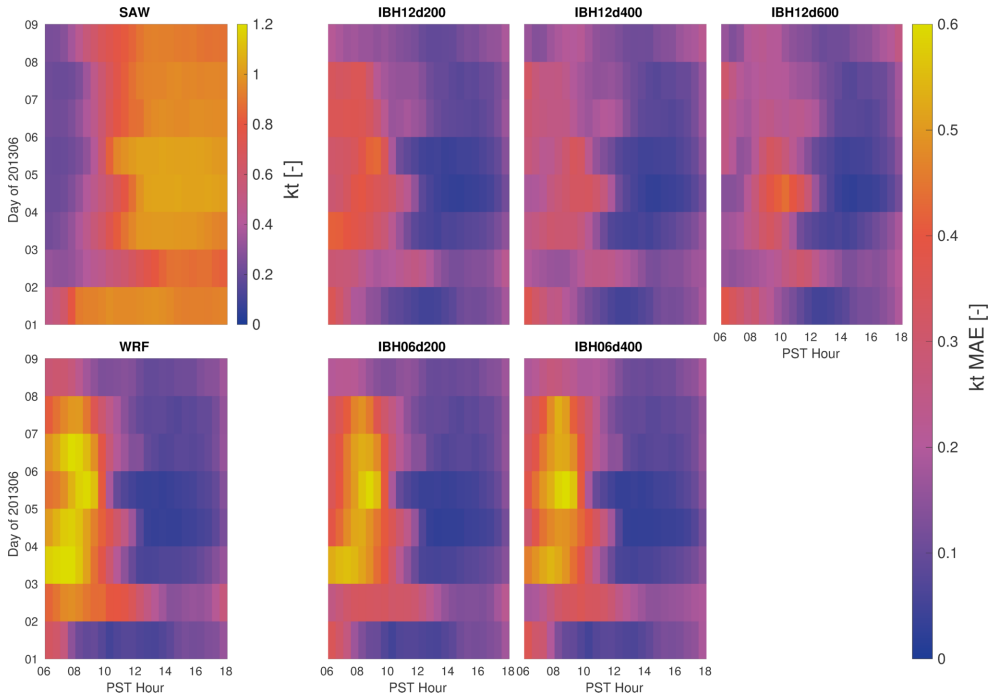

Figure 3.10: Time of day of SolarAnywhere kt and kt MAE of the baseline WRF simulation and each IBH ensembles compared to SolarAnywhere data for coastal marine layer region.

As a result of persistent synoptic conditions in the summertime, a naive 24 hour persistence forecast derived from ground measurements and SolarAnywhere data tends to perform well and serves as a valuable forecast benchmark. Table 3.3 and Table 3.4 summarize the GHI MBE and kt MAE of each ensemble and the persistence forecast at each ground stations and averaged over the coastal marine layer region. IBH12d400 is the overall best performer and is comparable to the persistence forecast. IBH06d200 and IBH12d200 outperform the other WRF forecasts for all three coastal stations as IBH ensembles with higher Δh tend to overpredict clouds and thus have larger errors (Figure 3.8f). For ESC, the improvement from IBH12d400 is most significant (Figure 3.8e).

Table 3.3 Summary of GHI (kt) forecast MBE [W/m2] for baseline WRF, 24 hour persistence, and IBH ensembles at SDG&E stations from coastal (PWS1) to inland (ESC) as well as averaged over the coastal marine layer region. Bold font indicate the best forecast (excluding persistence) and underscore indicate that the best forecast is also better than persistence. See also the map in Figure 3.1.

Station	WRF	Persistence	IBH06d200	IBH06d400	IBH12d200	IBH12d400	IBH12d600
PWS1	40 (0.08)	32 (0.05)	37 (0.07)	92 (0.15)	-33 (-0.02)	-52 (-0.05)	-11 (-0.02)
PWS4	97 (0.19)	12 (0.03)	75 (0.15)	98 (0.17)	-5 (0.05)	-72 (-0.05)	-16 (-0.01)
PWS6	87 (0.18)	5 (0.02)	72 (0.14)	76 (0.13)	-20 (0.02)	-91 (-0.08)	-107 (-0.12)
ESC	89 (0.17)	0 (0.00)	83 (0.15)	78 (0.14)	76 (0.14)	45 (0.07)	-50 (-0.04)
Coastal average	116 (0.20)	13 (0.02)	107 (0.18)	112 (0.19)	62 (0.12)	31 (0.07)	11 (0.04)

Table 3.4 Summary of GHI (kt) forecast MAE [W/m2] for baseline WRF, 24 hour persistence, IBH ensembles at SDG&E stations as well as average of coastal marine layer region.

Station	WRF	Persistence	IBH06d200	IBH06d400	IBH12d200	IBH12d400	IBH12d600
PWS1	133 (0.20)	180 (0.25)	127 (0.19)	163 (0.25)	128 (0.19)	150 (0.22)	132 (0.18)
PWS4	144 (0.25)	166 (0.23)	126 (0.21)	153 (0.25)	132 (0.21)	153 (0.23)	132 (0.20)
PWS6	119 (0.23)	140 (0.22)	111 (0.20)	127 (0.22)	113 (0.19)	142 (0.22)	165 (0.25)
ESC	91 (0.19)	40 (0.07)	86 (0.17)	81 (0.15)	79 (0.15)	56 (0.10)	70 (0.11)
Coastal average	127 (0.22)	99 (0.14)	119 (0.20)	123 (0.21)	101 (0.18)	98 (0.16)	105 (0.17)

3.6.3. Geographical error distribution

Figure 3.11 presents the spatial GHI MAE of baseline WRF and IBH ensembles averaged from 6 PST to 18 PST on June 1 to June 8, 2013. Figure 3.12 presents the GHI MAE of baseline WRF and the GHI MAE difference between IBH ensembles and baseline WRF. The baseline WRF shows significant GHI overprediction in coastal southern California as expected. The errors decrease from the coast to inland since clouds are less prevalent inland and the predominantly clear sky WRF forecasts therefore automatically become more accurate. Both IBH06d0 and IBH12d0 (the ensembles without IBH change) have similar spatial error patterns as baseline WRF, which suggests that the constant total water assumption in the PBL will not affect the results and these two ensembles will not be discussed further.

The 12 UTC ensembles (IBH12d200 and IBH12d400) outperform the 06 UTC ensembles. The difference in performance is likely related to the difference in timing of applying the IBH correction. As shown in Figure 3.13, the area of surface radiation inversions expands from 6 UTC to 12 UTC on June 3, due to surface cooling under (erroneously) clear skies, consistent with Kann et al. (2009). For example, for the grid

point at 33.88 N and -117.10 W, Figure 3.14 a and c show a subsidence inversion at 6 UTC while a surface radiation inversion is observed at 12 UTC. Since $\overline{Q_t}$ was computed from the lowest grid point near the surface to the original inversion base, a smaller value of $\overline{Q_t}$ was used for extrapolating the elevated inversions at 12 UTC than 6 UTC (see Figure 3.14 b and d). Therefore, for the expanded surface inversion areas from 6 to 12 UTC, the boundary layer tends to become drier in the 12 UTC ensembles. As shown in Figure 3.15, the 12 UTC ensembles predict less cloud cover than their 6 UTC counterparts for the west part of Los Angeles (LA), where surface inversions are observed at 12 UTC. However, the time averaged accuracy of the 06 UTC ensembles degrades as their clouds dissipate faster, as shown by Figure 3.7 f and i. Overall this suggests that it is important to maintain accurate IBH and cloud cover throughout the night to avoid unrealistic surface inversions that limit the ability to apply IBH corrections.

Considering the different Δh, IBH12d400 performs better than IBH12d200, especially in the LA basin area where IBH biases are larger (see Figure 3.3). The inconsistent performance at different times of day points towards using an ensemble forecast system with a postprocessing algorithm that adjusts the weights of the different ensemble members by time of day and location.

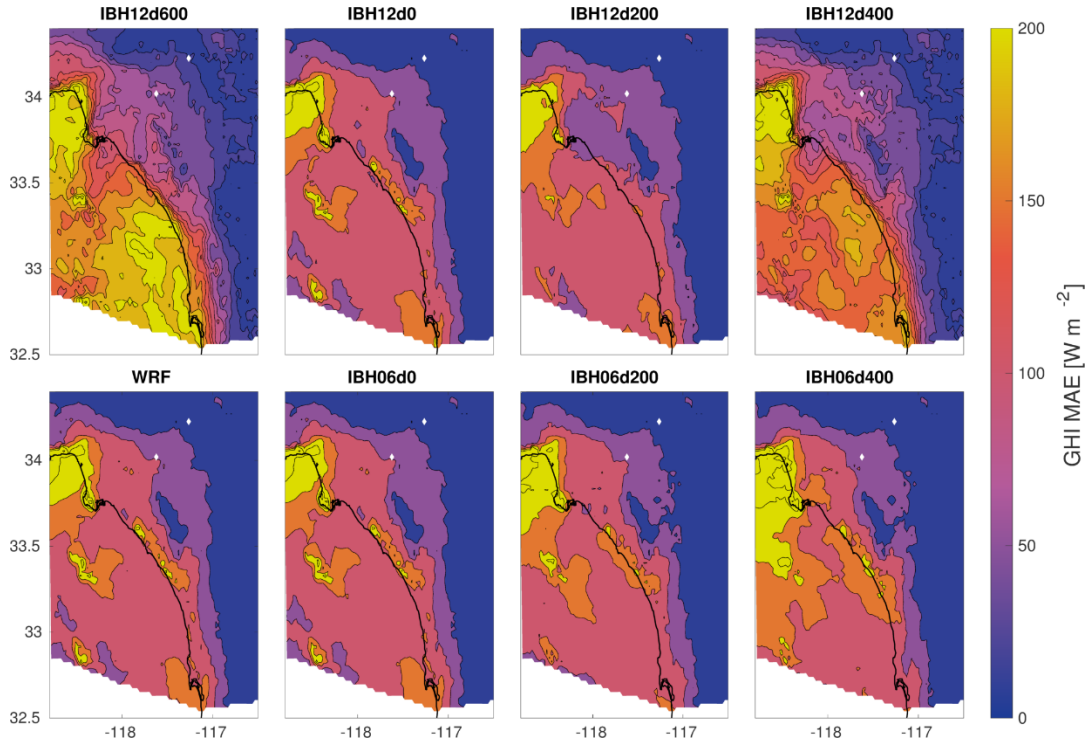

Figure 3.11: Spatial map of GHI MAE of the baseline WRF simulation and each IBH ensemble compared to SolarAnywhere data. Data are averaged from 6 PST to 18 PST on June 1 to June 8, 2013.

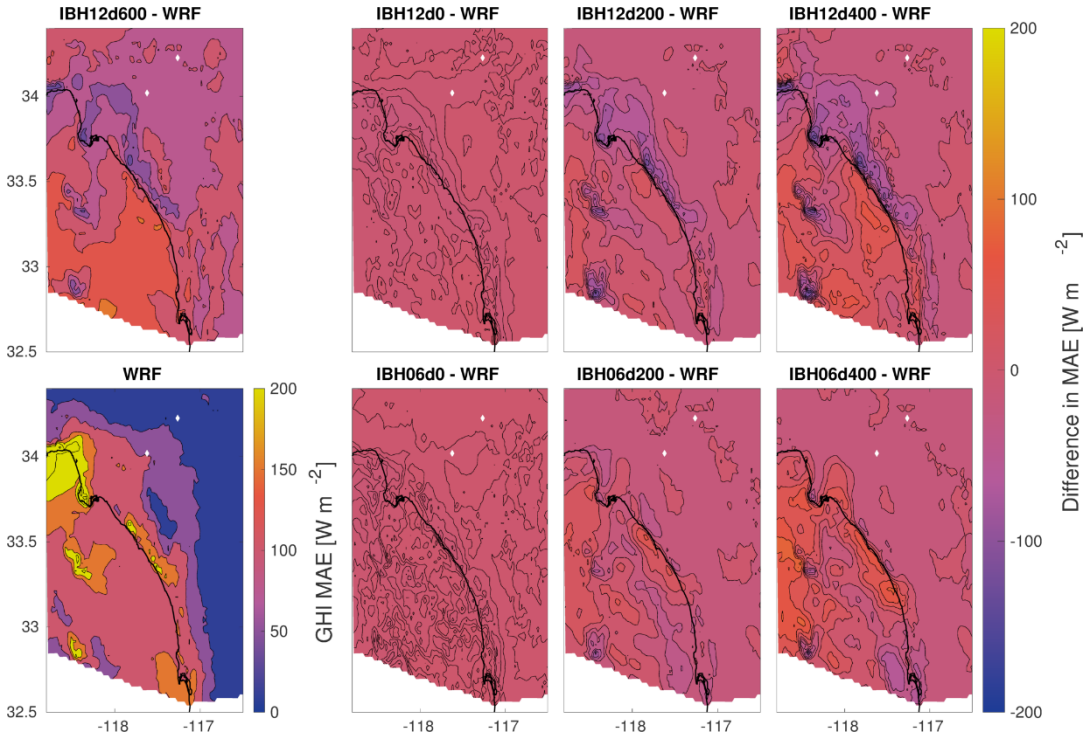

Figure 3.12: Spatial map of GHI MAE of baseline WRF compared to SolarAnywhere and the GHI MAE difference between IBH ensembles and baseline WRF from June 1 to June 8, 2013.

a) b)

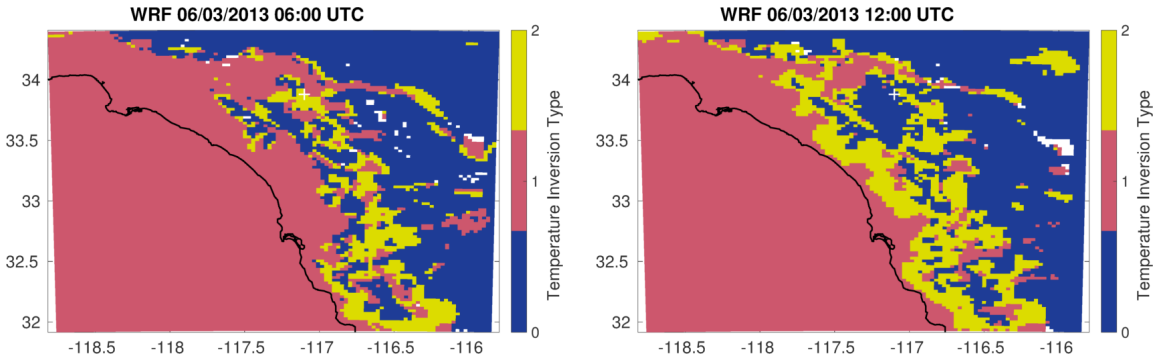

Figure 3.13: Spatial map of temperature inversion types (0: surface inversion; 1: subsidence inversion; 2: both surface and subsidence inversions) at 6 UTC (a) and 12 UTC (b) of June 3, 2013. See Section 6.1. for a definition of the inversion types. The white plus indicates the grid point at 33.88 N and -117.10 W (see Fig. 14).

a) b)

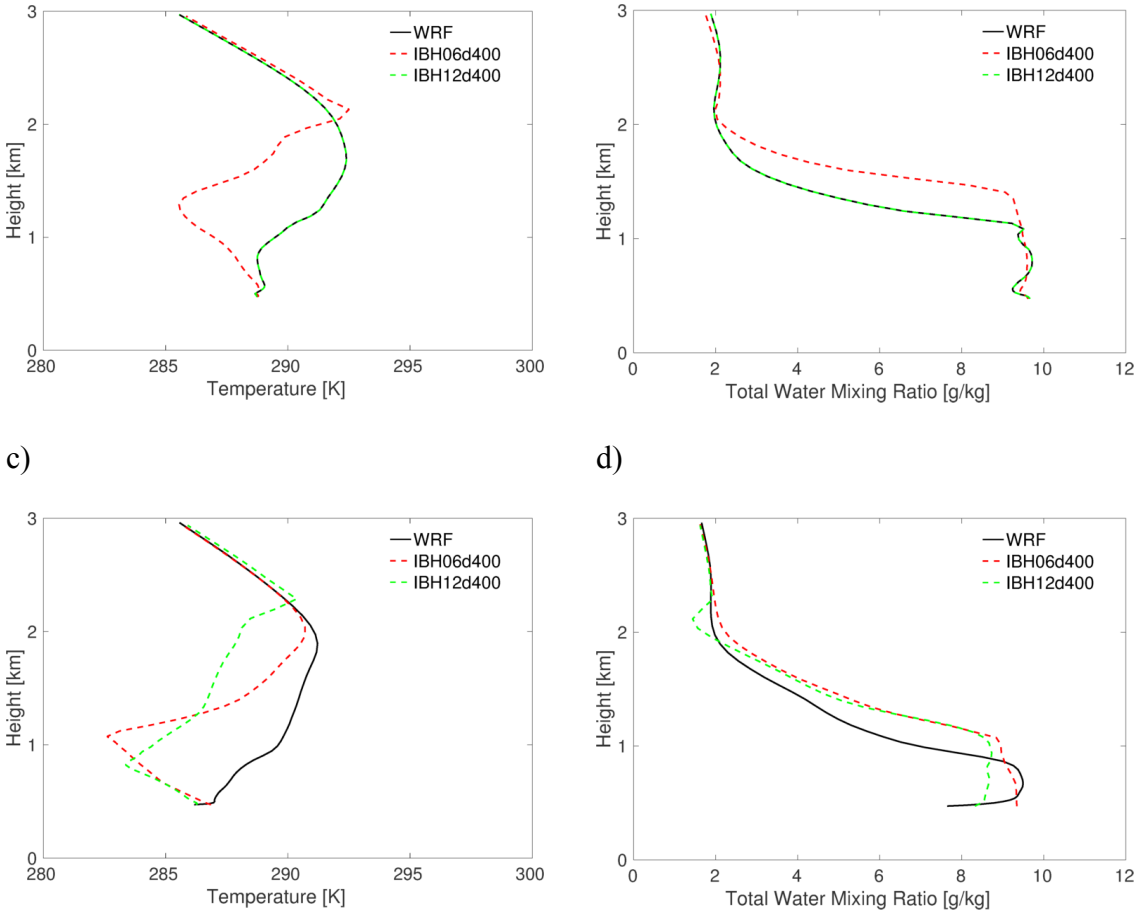

Figure 3.14: Vertical profiles of temperature (column 1) and total water mixing ratio (column 2) at 6:15 UTC (row 1) and 12:15 UTC (row 2) of the grid point at 33.88 N and -117.10 W (see white plus on Figure 3.13).

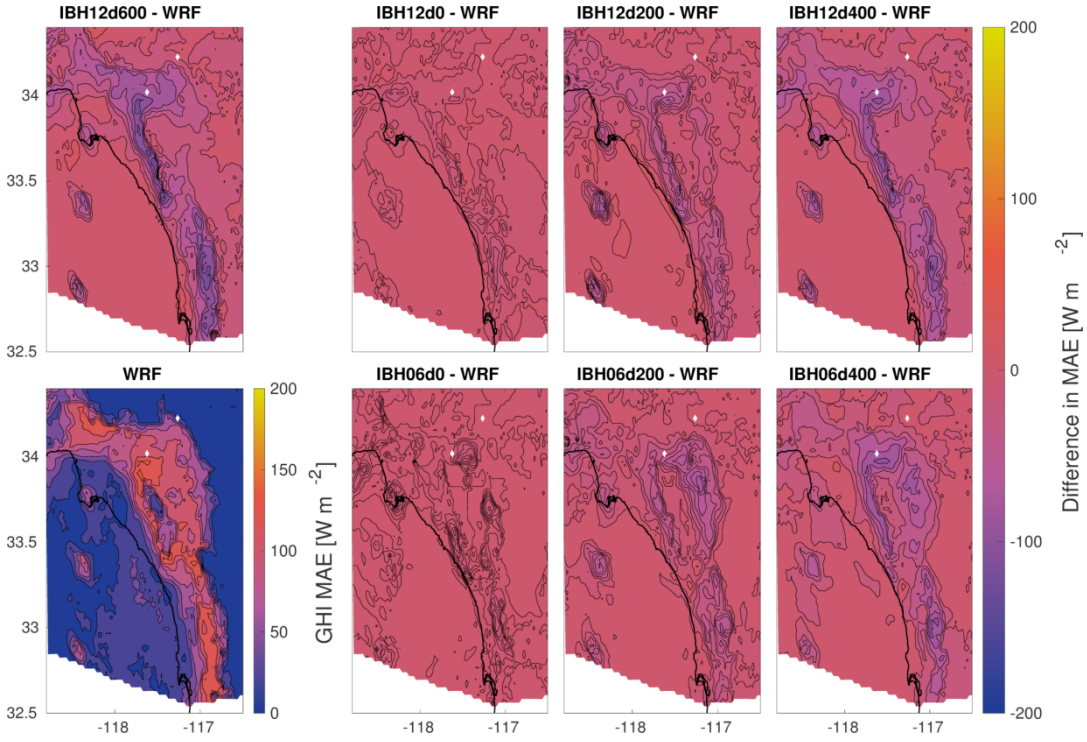

Figure 3.15: Spatial map of GHI MAE of baseline WRF compared to SolarAnywhere and the GHI MAE difference between IBH ensembles and baseline WRF at 14 UTC (6 PST) averaged from June 1 to June 8, 2013.

3.7. Conclusion

Marine boundary layer stratocumulus along the California coast are notoriously difficult to forecast with NWP. Forecasting stratocumulus over coastal lands did not receive significant attention from the research community until the increasing utilization of solar photovoltaic systems. Previous studies have found a correlation between temperature inversion base height (IBH) and MBL stratocumulus (Klein and Hartmann 1993). While IBH has been recognized as key for predicting MBL stratocumulus by NWP (Koračin et al. 2003; Jousse et al. 2016), the NWP models predict lower IBH than observations (Rahn and Garreaud 2010a,b). The IBH biases in WRF are associated with initial conditions, boundary conditions, and parameterizations of different atmospheric

processes and their interactions. While WRF PBL parameterization including insufficient vertical mixing and entrainment were postulated to be the fundamental issue (Hu et al. 2010), we did not attempt to address the fundamental causes of IBH biases.

In this paper, we first confirmed the positive correlation between IBH and inland extent of MBL stratocumulus (Figure 3.5). We developed a thermodynamically consistent IBH correction method to reduce the IBH biases. IBH ensembles differed by the values of Δh (0, 200, 400, and 600 m) and the timing (06 and 12 UTC) of applying the IBH correction. When validated spatially against SolarAnywhere GHI data, IBH ensembles with nonzero Δh improved substantially upon the baseline WRF, especially in the coastal strip (Figure 3.12). IBH corrections applied at 6 UTC predict more cloud cover inland during the early morning due to reduced prevalence of surface radiation inversions at 6 UTC compared to 12 UTC. The performance of the 6 UTC corrections degrades as clouds dissipate faster. Overall IBH ensembles applied at 12 UTC performed best.

For each IBH ensemble, the same Δh is applied for the entire domain. But IBH biases vary spatially and larger IBH biases were observed at VBG near the LA basin than in San Diego. Although using higher Δh reduces GHI biases and promotes further inland penetration in the morning, cloud thickness is often overpredicted around noontime (IBH12d600). For operational forecasting, it is suggested to run IBH ensembles with multiple values of Δh and/or to correct NWP IBH by the actual biases compared with sounding. However, since sounding measurements are only available at 12 UTC and for this application the grid operator required solar forecast delivery by 06 PDT = 13 UTC. The 12 UTC sounding leaves insufficient time to run and postprocess WRF while the 00

UTC sounding is suboptimal due to its age. An alternative data source for IBH calibration that is accessible at an earlier time is needed. A method of deriving sounding data using surface measurements is described and validated in Appendix B.

While the simulation results with IBH corrections show promise, ultimately, we would like to also improve PBL parameterizations and numerical advection schemes to reduce IBH biases and improve the WRF stratocumulus forecasts over the California coast.

3.8. Appendix

3.8.1. Well-mixed PBL Assumption

The plausibility of assuming constant total water mixing ratio is examined by computing deviations of Q_t at the original inversion base from the mass-weighted average of $\overline{Q_t}$ within the PBL which is calculated by

$$\overline{Q_t} = \frac{\sum_{z_1}^{z_{base}^{old}} dp(z) Q_t(z)}{\sum_{z_1}^{z_{base}^{old}} dp(z)} \tag{3.7}$$

where z_1 is the height of lowest grid point near surface, and dp is the layer pressure. As shown in Figure 3.16, the aforementioned assumption is valid for most WRF grids.

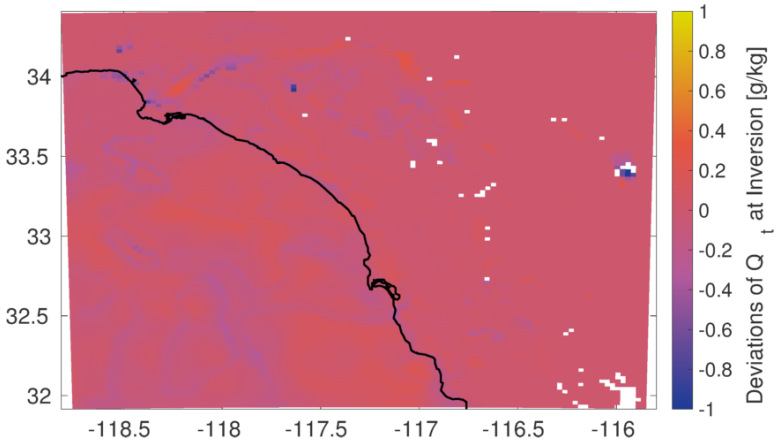

Figure 3.16: Spatial map of deviations of Q_t at inversion base from the mass-weighted average of $\overline{Q_t}$ (Eq. A-1). White areas indicate that no inversion was found. The domain average Q_t and deviation of Q_t was 6.2 and -0.017 g/kg.

3.8.2. Derivation of IBH using Surface Measurements

Assuming homogeneous and steady PBL structure west of the mountains on stratocumulus days, measurements from SDG&E weather stations along an elevation gradient at 10 UTC compose a "surface sounding"[2]. To avoid micrometeorological effects such as cold pools a subset of 19 topographically exposed SDG&E weather stations (Figure 3.2 and Table 3.1) spanning from coast to inland region are selected.

[2] Surface soundings were originally proposed by Steve Vanderburg from San Diego Gas & Electric Company.

Figure 3.17a validates the assumption of steady PBL structure as surface sounding temperature profiles at 10 to 12 UTC are similar and agree with the NKX sounding. Small IBH errors of surface soundings compared with that WRF or NAM profiles (Figure 3.1) are confirmed in Figure 3.17b and Table 3.5 proving the feasibility of using surface sounding IBH to run WRF IBH ensemble.

On some days the assumption of homogeneous PBL structure was invalidated e.g. by strong onshore flow that pushed marine air masses up the slopes. With the exception of those cases, surface sounding can be created using the widely distributed surface temperature measurements.

a) b)

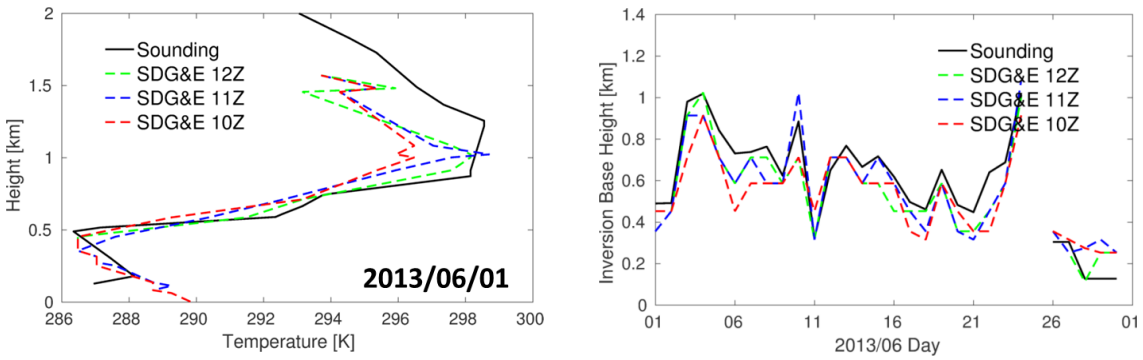

Figure 3.17: Comparisons of temperature profile (a) and IBH (b) from 12 UTC NKX sounding and SDG&E surface sounding created using measurements at 10 to 12 UTC. For June 25, 2013 at NKX, multiple inversions are observed and maximum inversion strength is less than 3 K which does not pass the inversion requirements in our algorithm.

Table 3.5 Summary of IBH MBE (m) and MAE (m) for surface sounding using temperature measurements of SDG&E weather stations at 10 to 12 UTC.

	2013/06	
	MBE (m)	MAE (m)
SD&GE 12Z	-51	76
SD&GE 11Z	-37	90
SD&GE 10Z	-69	114

Acknowledgements

Chapter 3, in full, is a reprint of the material as it appears in Zhong, X., D. K. Sahu, and J. Kleissl, 2017: WRF inversion base height ensembles for simulating marine boundary layer stratocumulus. *Solar Energy*. The dissertation/thesis author was the primary investigator and author of this paper.

4. Machine Learning Models with Selected Meteorological Variables

4.1. Data Processing

4.1.1. Data and Prediction Domain

SolarAnywhere (SAW, 2016) solar irradiance data developed by Clean Power Research is used for evaluating the performance of the machine learning models. The SAW GHI data is normalized by clear sky GHI computed from the Ineichen model (Perez et al. 2002; Ineichen 2008) to remove the diurnal and seasonal variations of solar irradiance and yield the clear sky index. Hourly SAW data at a horizontal resolution of 0.02°(2km) are interpolated spatially using nearest neighbor interpolation onto the grid at a horizontal resolution of 12.5 km shown in Figure 4.1a. Also, as MBL clouds are more commonly observed over the coastal region, model performance is computed for the marine layer region (Figure 4.1b) where the ground elevation is lower than 375 mean sea level (MSL) and June monthly average kt is smaller than 0.92 (Zhong et al. 2017; Yang and Kleissl 2016b). The sounding sites at San Diego (NKX: 32.85 N, -117.11 W) and Vandenberg (VBG: 34.75 N, 120.56 W) measure vertical profiles of altitude, pressure, temperature, relative humidity, and wind at 0 and 12 UTC every day. To account for the daily and seasonal cycle of solar radiation, solar altitude and azimuth angles are also included in feature space.

We collect the historical SolarAnywhere and sounding data for 11 months, including May to September in 2013 and 2014 as well as June in 2016 (data in 2015 are not used as it is an El Niño year). As we are only interested in MBL clouds, days with high clouds are removed. The remaining 210 days are divided into training (172 days)

and testing dataset (38 days). For each grid point in the domain, the data from the two sounding station at 12 UTC (pre sunrise), solar altitude and azimuth angles of the grid point from 14 UTC to 25 UTC (i.e. 1 UTC) are used to predict the solar radiation intra-day, i.e. from 14 UTC (7 LST) to 25 UTC (i.e. 1 UTC on the second day, 18 LST).

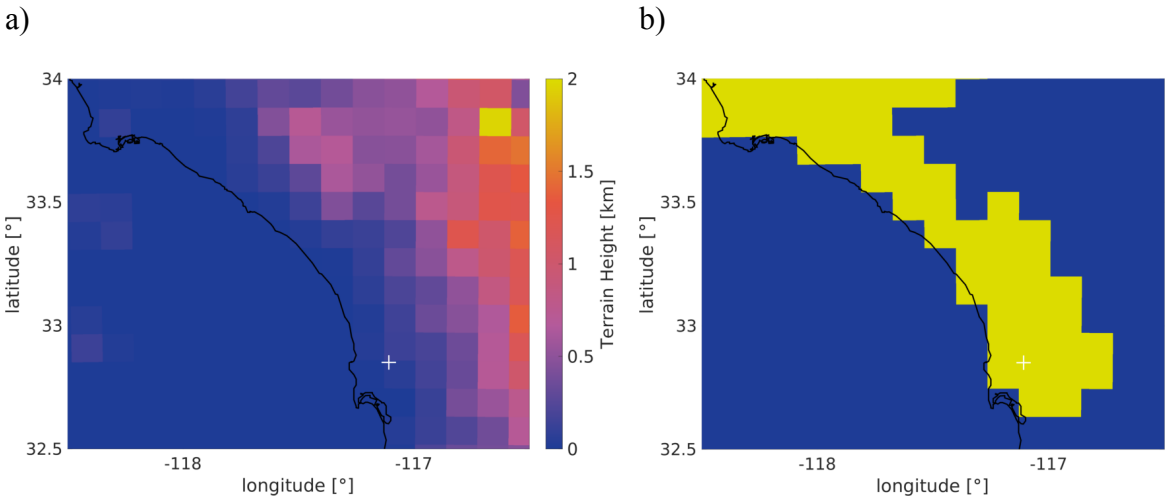

Figure 4.1: Digital elevation data of the domain used for training and testing (a) and marine layer region (b). White plus is NKX station. VBG station is outside the domain.

4.1.2. Characteristics of MBL Clouds and Variable Selection

MBL clouds are characterized by a strong temperature inversion that inhibits mixing of warm dry air with the cool moist cloud layer. The higher the inversion base, the higher the cloud top height and the larger the inland penetration and spatial extent of cloud cover. The temperature inversion is unusually sharp because of subsidence, and the inversion strength is expected to be an important predictor of solar irradiances. Subsidence is quantified using the 1000-500 mb thickness from 12 UTC radiosounding.

Table 4.1 List of Meteorological Variables

Feature Name	Symbol
Inversion Base Height	IBH
Inversion Strength / Temperature Jump at Inversion	ΔT_{inv}
Moisture jump at Inversion	Δq_v
1000-500 mb Thickness	$\Delta h_{1000-500\,mb}$
Liquid Water Path	LWP
Precipitable Water	PW
Maximum Relative Humidity below 3 km	RH_{max}
Maximum Relative Humidity above 3 km	$RH_{high\,max}$
Boundary Layer Wind Component in East-West direction	U
Boundary Layer Wind Component in North-South direction	V
Solar Altitude Angle	α_s
Solar Azimuth Angle	ϕ_s

Usually, MBL clouds over land reach maximum thickness and spatial coverage during the early morning hours before sunrise. Therefore, during the first few hours after sunrise, the amount of solar radiation at the surface mostly depends on the initial cloud optical depths which are directly related to the cloud liquid water path (LWP) in Eq. 4.1.

$$LWP = \int_o^{p=p_0} q_L dp/g, \tag{4.1}$$

where g is gravitational acceleration, p is pressure, and q_L is the cloud water mixing ratio, which can be approximated using water vapor mixing ratio and estimated saturation water vapor mixing ratio from temperature and pressure of the radiosounding. Since the variance in the feature values is more important than the absolute values, we

approximate LWP by assuming saturation occurs when relative humidity is larger than or equal to 90% which likely overestimates LWP.

After sunrise, a significant portion of solar radiation is absorbed by the land surface and converted to surface heat and moisture fluxes. The warming and moistening of near surface air leads to stronger turbulent mixing in the boundary layer, and stronger mixing of dry air from cloud top (called entrainment) causes clouds to dissipate. The cloud-top entrainment velocity derived by Ghonima et al. (2016) shows that the entrainment is related to the temperature and moisture jump at the inversion. Larger temperature jump leads to weaker entrainment and delays the cloud dissipation. On the other hand, larger moisture jumps suggest that drier air from above the inversion is mixed into cloud layer, which will accelerate the cloud dissipation and vice versa. Ghonima et al. (2016) also showed that when strong winds blow from ocean to the land, clouds dissipation time is usually delayed. Here, we compute the average west-east (U, across the coast line) and north-south (V, along the coast line) wind components below the inversion base height to account for the strength and direction of wind. As shown in Figure 4.2, the U wind component at 0 UTC (afternoon) is mostly positive in the boundary layer, indicating that the sea breeze is fully developed. On the other hand at 12 UTC (night), wind is much weaker and the distribution is symmetric about zero. In Fig. 3, kt shows stronger correlations with wind at 0 UTC than wind at 12 UTC. Therefore, wind at 0 UTC is used for NKX, while wind at 12 UTC is still used for VBG due to very limited number of 0 UTC measurements available at VBG.

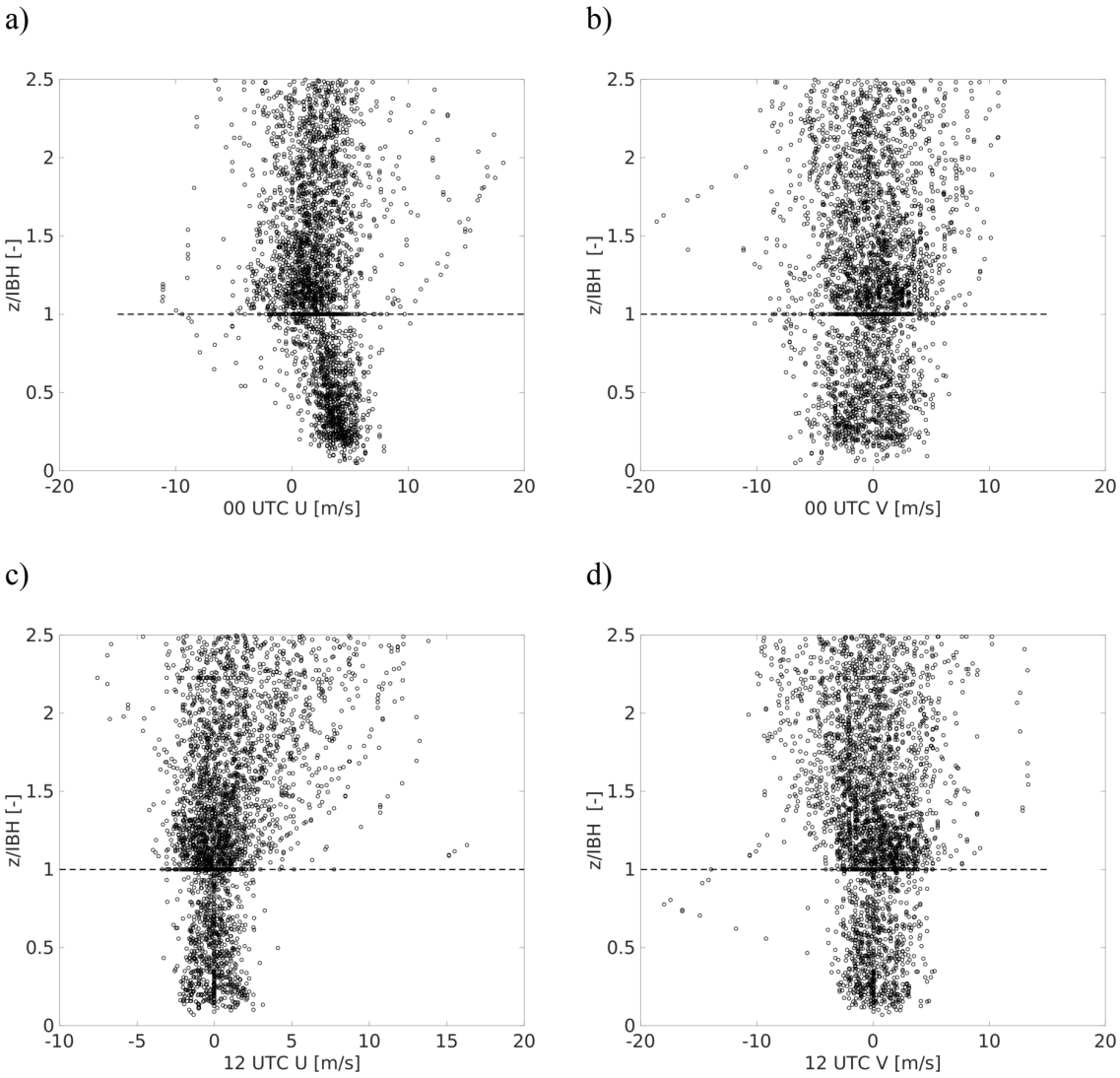

Figure 4.2: 0 UTC (a,b) and 12 UTC (c,d) U (across the coast line) and V (along the coast line) wind components measured at the Miramar sounding station.

All the variables relevant to either cloud optical properties or the cloud development are derived from sounding data and listed in Table 4.1. As the sounding sites only represent two grid points, to improve forecasts in the cases when clouds are only observed near the immediate coast while not observed at sounding sites, we include the maximum relative humidity below and above 3 km and total precipitable water to specify the dryness and possibility of cloud formation in the boundary layer.

4.1.3. Linear correlation between kt and meteorological variables

Figure 4.3 shows the Pearson correlation coefficient between all the selected meteorological variables and kt at different hours of the day. kt has the highest correlation with IBH as it indicates the spatial extent of clouds. The second highest correlation is with LWP, since marine layer is spatially homogenous and the amount of cloud water over the marine layer region are highly correlated. And the correlation with kt is usually highest in the morning hours and decreases gradually from morning to afternoon. The strong negative correlation between kt and V indicates that strong southerly wind favors more clouds. The southerly wind is often a result of Catalina eddy events, which are usually accompanied with persistent clouds along the coast. In addition, meteorological variables measured at NKX generally have higher correlation than those measured at VBG probably due to geographical proximity. The correlation coefficient between each variable and kt only shows linear dependence, and some non-linear correlation will be further discussed in next section.

a)

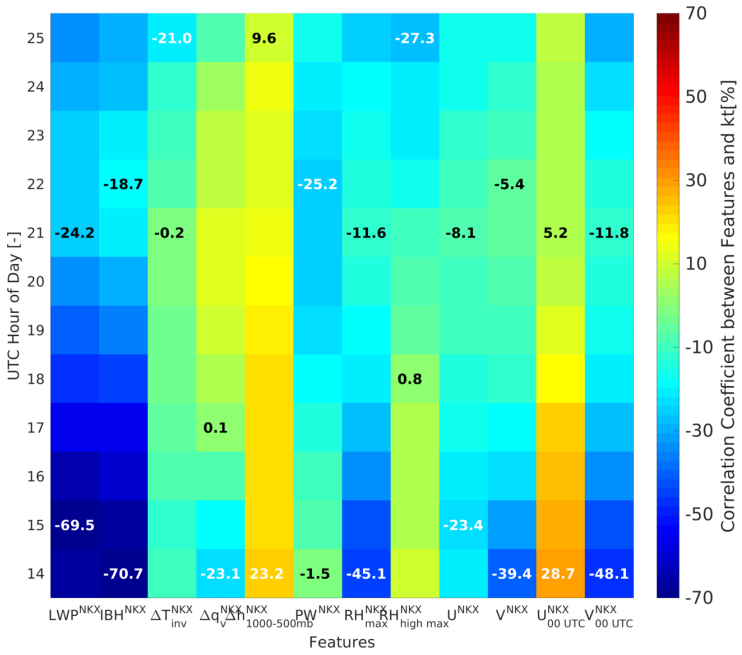

b)

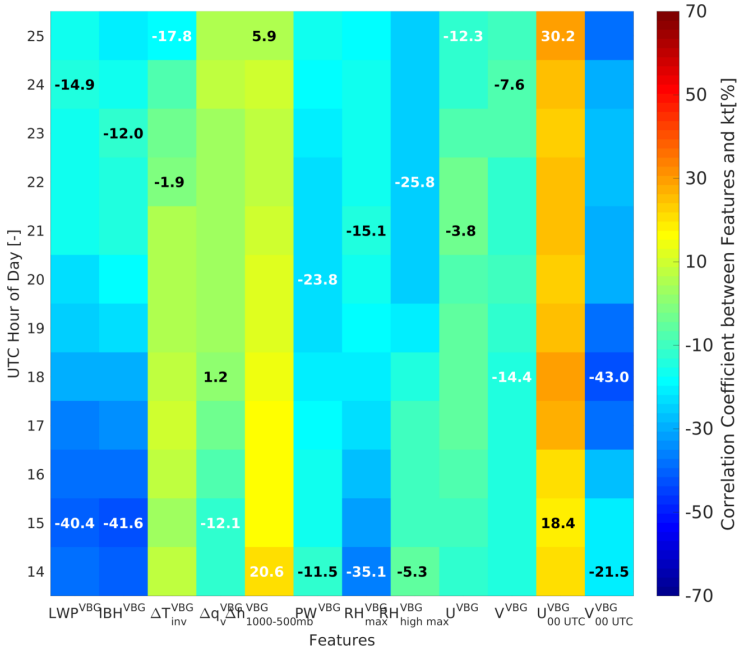

Figure 4.3: Pearson correlation coefficient between kt at different hours of day and selected meteorological variables measured at NKX (a) and VBG (b) sounding station at 12 UTC. The highest absolute correlation between each variable and kt at different UTC hours is shown in whitewhite numbers while the lowest is shown in black numbers.

4.1.4. Non-linear correlation

To further investigate the importance of the selected variables to cloud dissipation, all 210 days are classified into days when MBL clouds dissipate over land in the daytime (115 days), days when at least a patch of clouds persist for the entire day along the coastline (88 days), and clear sky days (17 days). We found the most distinguishing features determining whether clouds dissipate or not include inversion strength, LWP, and 1000-500 mb thickness. As shown in Figure 4.4, the chances of clouds persist increases substantially when the inversion strength is larger than 10 K. The stronger inversion suppresses the entrainment of dry air at cloud top, which favors maintenance of clouds, consistent with Myers and Norris (2013). And thin clouds, defined here as approximated LWP smaller than 200 g/m^2, are more likely to dissipate during the day, while thick clouds are more likely to persist especially when approximated LWP is larger than 600 g/m^2. Figure 4.4b shows a strong and positive correlation between inversion strength and 1000-500 mb thickness, which is a measure of subsidence and an indicator for the presence of a low or high pressure system. For days when the 1000-500 mb thickness is smaller than 5650 m, clouds always persist for the entire day. Those small values of 1000-500 mb thickness suggest a low-pressure system, which usually indicates longer cloud lifetime probably due to the associated cold front bringing cold air.

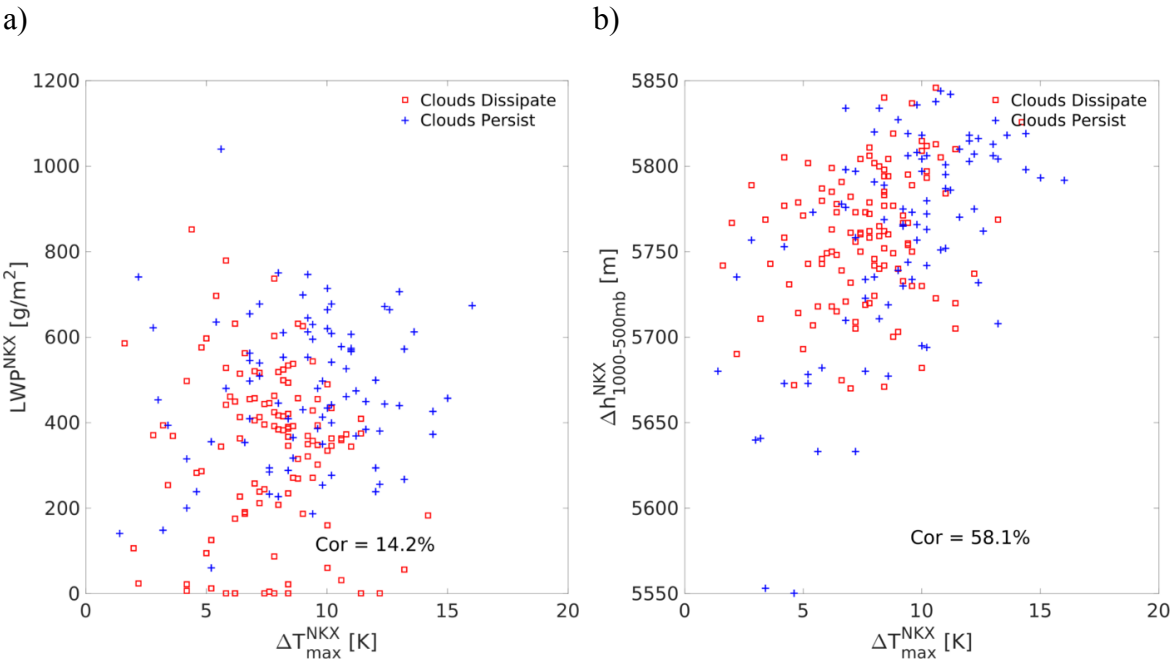

Figure 4.4: Inversion strength, liquid water path (a) and 1000-500mb thickness (b) are closely related to whether clouds will dissipate. While the relationships especially with cloud persistence are non-linear, the correlation coefficients between the variables plotted on the axes are also given.

Based our domain knowledge and case studies, we propose four common cases why MBL clouds persist along the coastline for the whole day: 1) strong inversion; 2) thick cloud layer; 3) post cold front and low pressure system; 4) moist inversion layer (i.e. small moisture jump at inversion); 5) strong coastal or Catalina eddy. The most common case is a strong inversion, which is associated with persistent Pacific high pressure system during summertime or cool ocean water. Cool ocean water cools the boundary layer both off and on-shore via advection and can be caused by upwelling of cold deep coastal water and/or the California ocean current system bring cold water from high latitude to California. Cases 1), 2), and 3) are demonstrated by the Figure 4.4, and a strong coastal eddy (Case 5) is often associated with Catalina eddy events as

demonstrated by the large anticorrelation in Figure 4.3. To better illustrate case 4), we compare two days of similar initial LWP and different cloud dissipation time.

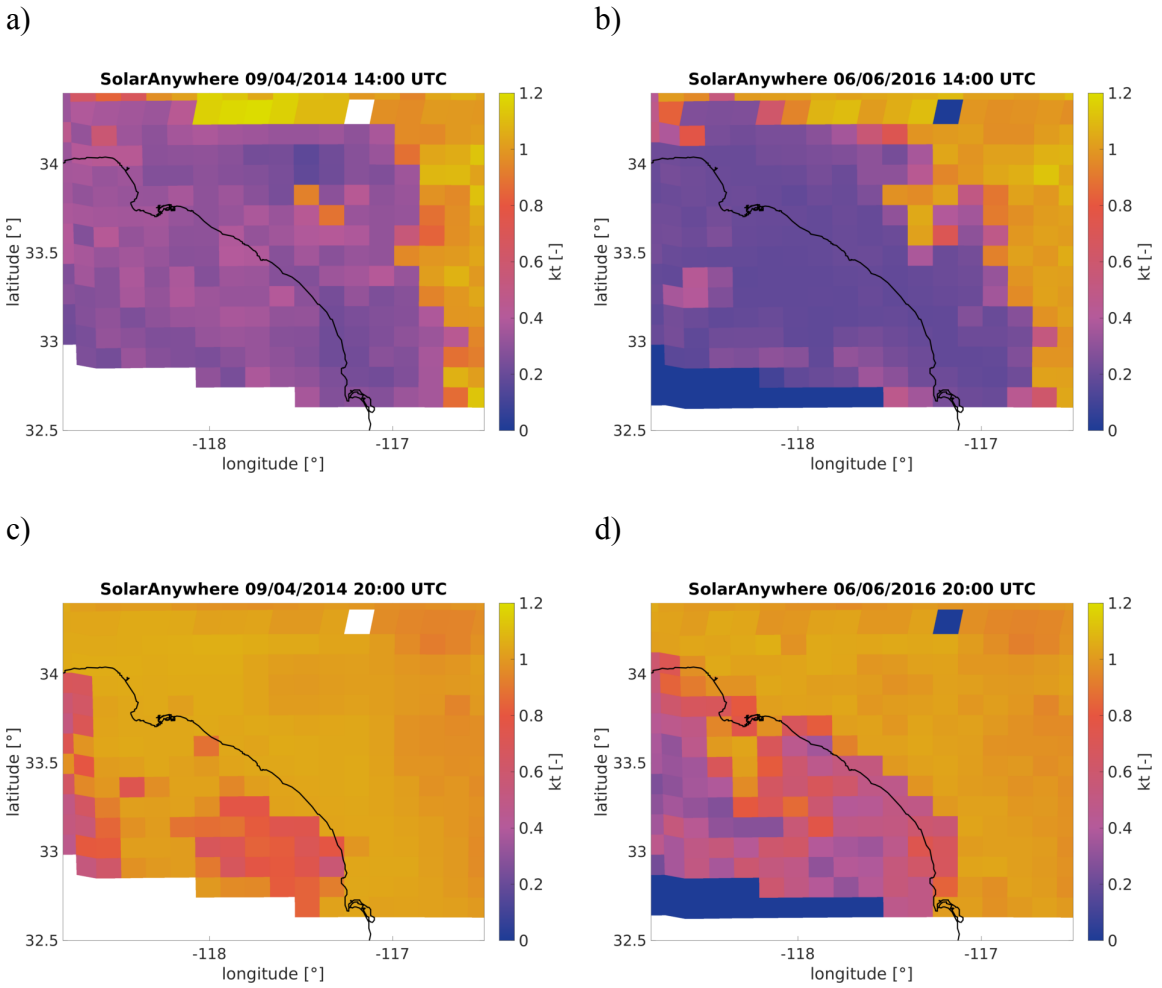

Figure 4.5: Spatial map of SolarAnywhere clear sky index at 14 UTC (a) and 20 UTC (c) on September 4, 2014 and 14 UTC (b) and 20 UTC (d) on June 6, 2016.

Figure 4.5 shows that clouds dissipate over land on September 4, 2014 (hereafter day 1) before 20 UTC while clouds with similar spatial coverage in the morning on June 6, 2016 (hereafter day 2) persist until sunset (not shown here). The feature intercomparisons between these two days in Table 4.2 indicate that meteorological conditions are almost the same except for the difference in Δq_v (moisture jump at

inversion) and *PW* (amount of total column water in the atmosphere). Although day 2 has less water in the atmosphere, day 2 has a smaller moisture jump at the inversion (3.9 versus 7.8 g/kg, see also Figure 4.6) and therefore the entrainment drying is weakened.

Overall, we have selected all the relevant meteorological variables that are derived from two sounding stations over southern California. And only with these relevant variables, can machine learning methods learn the day-to-day variations and generalize to new data. In next section, we discuss the machine learning models we used for prediction.

Table 4.2 List of feature values derived using the 12 UTC sounding data from NKX station.

Feature	09/04/2014	06/06/2016
IBH [km]	0.9	0.8
ΔT_{inv} [K]	7.8	8.0
Δq_v [g/kg]	7.8	3.9
$\Delta h_{1000-500\,mb}$ [m]	5772.0	5791.0
LWP [g/m2]	736.5	749.8
PW [mm]	18.8	14.3
RH_{max} [%]	100.0	100.0
$RH_{high\,max}$ [%]	50.0	43.0
$U_{00\,UTC}$ [m/s]	3.5	3.9
$V_{00\,UTC}$ [m/s]	-0.6	-2.1

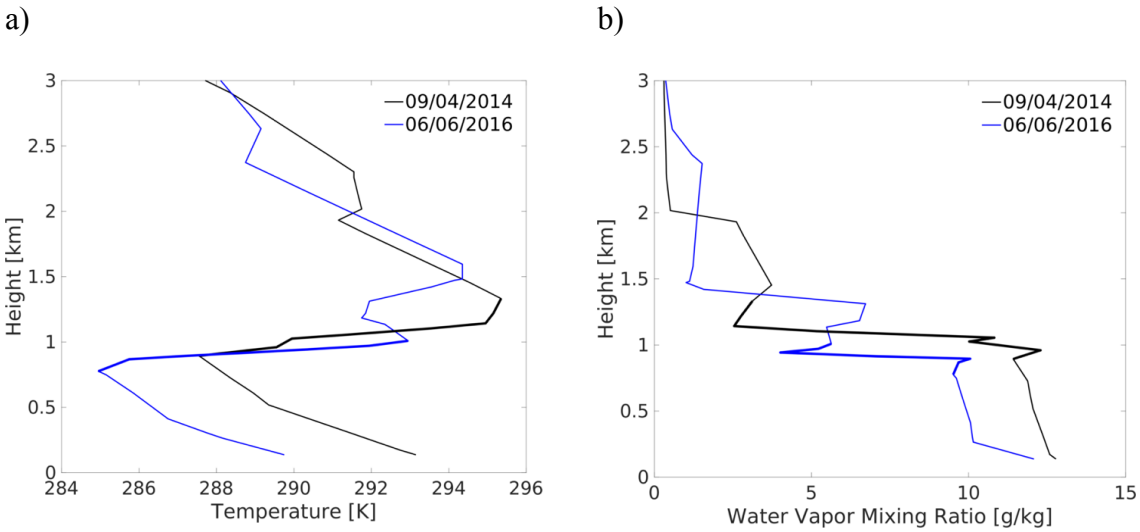

Figure 4.6: Vertical profiles of temperature (a) and water vapor mixing ratio (b) at 12 UTC measured by NKX sounding station for the days in Figure 5 and Table 2. Vertical profiles within inversion layer are thickened.

4.2. Description of Machine Learning Models

4.2.1. Overview

Machine-learning techniques such as SVM, RF or GB are supervised learning methods or data-driven approaches. As a result, these techniques rely on the information content embedded in the training data to produce forecasts on unseen data. In specific, the model parameters are determined with the help of N pairs of input and output examples contained in the training data. Once the model is fitted, the model can be evaluated on the test dataset. This second phase, called the generalization phase, consists of evaluating the ability to generalize, i.e., to give correct outputs when it is confronted with examples that were not seen during the training phase, using the test dataset.

In our context, $\mathcal{D} = \{\boldsymbol{x}_i, y_i\}_{i=1}^{N}$ represents the training dataset. The vector $\boldsymbol{x}_i$ contains the input features values and y_i refers to the corresponding clear sky indeces. The column vector inputs for all N training cases can be aggregated in the so-called $N \times p$

(p is the number of features) design matrix $\boldsymbol{X}$ and the corresponding model outputs (or targets) are collected in the vector $\boldsymbol{y}$ so we can write $\mathcal{D} = \{\boldsymbol{X}, \boldsymbol{y}\}$. Similarly, considering n^* test cases, we have $\mathcal{D}^* = \{\boldsymbol{X}^*, y^*\}$ for the test dataset.

4.2.2. Support vector machine

Support vector machine (SVM) is a kernel-based machine learning technique (Vapnik 1995). It can be shown (Smola and Schölkopf 2004) that, given N training samples, the prediction generated by this method for an input test vector $\boldsymbol{x}^*$ can be expressed in terms of a linear combination of n kernel functions, each one centered on a training point.

Support vector regression (SVR) is based on the application of SVMs to regression problems. The prediction $\hat{y}$ calculated by a SVR machine for an input test case $\boldsymbol{x}^*$ is given by Eq. 4.2:

$$\hat{y} = \sum_{i=1}^{N} a_i \, k_{rbf}(\boldsymbol{x_i}, \boldsymbol{x}^*) + b, \tag{4.2}$$

where k_{rbf} is the radial basis function (RBF) $k_{rbf}(\boldsymbol{x_p}, \boldsymbol{x_q}) = exp\left[-\gamma \left|(\boldsymbol{x_p} - \boldsymbol{x_q})\right|\right]$ with hyperparameter γ. The coefficients a_i are determined by minimizing a specific loss or cost function. For SVM, this cost function can be minimized by solving a quadratic programming (QP) that provides a unique solution for the coefficients as the problem is strictly convex. The parameter b (or bias parameter) is derived from Equation 2 and some specific conditions. See Smola and Schölkopf (2004) for details on SVM principles.

In addition, it must be stressed that not all the training samples are used in Eq. 4.2. A convenient choice of a cost function called Vapnik's ε-insensitive function (Smola and

Schölkopf 2004) in the QP problem yields a sparse solution, meaning that the loss function ignores the error when the errors are no greater than ε. Those $\boldsymbol{x_i}$ in Eq. 4.2 with nonzero coefficients are called Support Vectors. Smola and Schölkopf (2004) also proposed a variant called the υ -SVR method where the ν that controls the amount of support vectors used in the regression.

We chose the RBF kernel of the libSVM library for this work. The libSVM library evaluates the prediction performance based on the mean squared error (MSE) calculated as (Hsu et al. 2003)

$$MSE = \frac{\sum_{i=1}^{N}(f(x_i)-y_i)^2}{N}, \tag{4.3}$$

where $f(x_i)$ are the predicted values and y_i are the observed values. The Eq. 4.3 is also called loss function, which machine learning models try to minimize over the training dataset. We selected MSE over another commonly used loss function, the mean absolute error, to emphasize performance on outlier (extremely cloudy) days.

The libSVM library provides both ϵ-SVR and υ-SVR for regression. ϵ-SVR provides more control over the allowable error for the model while the proportion of the number of support vectors can be controlled in υ-SVR. The optimization is achieved through a parameter C that control the trade-off between overfitting and generalization ability of the algorithm, a parameter γ of the kernel function that controls the smoothness of the kernel function, and ϵ (or υ) for ϵ-SVR (or υ-SVR). These parameters are found using the "grid-search" method and a k-fold cross-validation procedure. The grid-search method trains and evaluates the SVM model by first trying a relatively coarse and exponentially growing sequences of C (2^{-10}, 2^{-5}, 2^{0}, 2^{5}, 2^{10}), γ ($2^{\left(\log_2\frac{1}{D}-10\right):5:\left(\log_2\frac{1}{D}+10\right)}$, D

is the number of features), and ϵ ($2^{(\log_2 0.1-10):5:(\log_2 0.1+10)}$) or υ ($2^{(\log_2 0.5-10):5:(\log_2 0.5+10)}$) values. After identifying the optimal parameters in the coarse search, grid search will be run on a finer grid centering on the optimal parameters.

If all of the training data were used for optimizing those parameters, the model would likely overfit the training data and perform poorly on the validation set. Therefore, a 5-fold cross-validation is applied by partitioning the training data into 5 subsets of equal size (Hsu et al. 2003). Then the model is trained using one subset at a time and the MSE is calculated using the remaining (validation) subsets. The average MSE is used to find the optimal parameters. Before partitioning the training dataset into 5 folds, the training data are grouped into kt bins (0:0.1:1.2) so that each subset has the same portions of binned data. In addition, as the 12 UTC sounding features are repeatedly used from 14 UTC to 25 UTC with variations only in solar altitude and azimuth angle, features of the same day are required to be in the same fold to avoid overfitting.

4.2.3. Random forest

RF are constructed by growing many binary decision trees called classification and regression trees (CART) (Hastie et al. 2009). Regression trees are simple models that divide the input (or feature) space into a set of rectangular regions and then assume a constant value to each region. A recursive greedy top-down algorithm is used to partition the input space into regions. See Hastie et al. (2009) for details regarding the stratification of the input space.

Following the notation given by Breiman (2001), a tree is denoted by $T(\theta)$. θ is a random parameter vector that determines how a tree is grown, i.e. how the input space is

stratified in terms of split variables, split locations, and terminal-node mean values. $T(\theta)$ partitions the input space into L distinct regions $\{R_l\}_{l=1}^{L}$.

Using the N independent observations of the training set (x_i, y_i), $i = 1, 2, \cdots, N$, the prediction $\widehat{y(x)}$ of a single tree $T(\theta)$ for a new data point $X = \boldsymbol{x}$ is obtained by averaging over the training observations that fall in the region $R_{l(x,\theta)}$ of the input space to which $\boldsymbol{x}$ belongs :

$$\widehat{y(x)} = \sum_{i=1}^{N} \omega_i(x, \theta) y_i, \tag{4.4}$$

where the weights $\omega_i(x, \theta)$ are given by : $\omega_i(x, \theta) = \frac{\mathbb{I}_{\{X_i \in R_{l(x,\theta)}\}}}{\#\{j: x_j \epsilon\, R_{l(x,\theta)}\}}$. The indicator function $\mathbb{I}_{\{u\}}$ has the value of 1 if its argument u is true and 0 otherwise.

Random Forest is a collection or committee of K single trees that are built on bootstrapped training subsets (Hastie et al. 2009). In addition, a random sample of input variables is considered at each split of the tree. Using RFs, the prediction $\widehat{y(x)}$ for a new data point $X = x$ is approximated by the averaged prediction of K single trees:

$$\widehat{y(x)} = \sum_{i=1}^{N} \omega_i(x)\, y_i, \tag{4.5}$$

where $\omega_i(x) = \frac{1}{K} \sum_{t=1}^{K} \omega_i(x, \theta_t)$. The size of the random sample of input variables called mtry is the single tuning parameter of the algorithm. The optimal value of this hyper-parameter was found with the tuneRF function provided by the R package RandomForest (Liaw and Wiener, 2002).

The RandomForest package also offers a means to assess the relative importance or contribution of each input variable in predicting the response. At each split in each tree, the improvement in the splitting criterion (here the residual sum of squares) is the

importance measure attributed to the splitting variable. This importance metric is averaged over all the trees and the higher this metric, the more important the input feature.

4.2.4. Gradient boosting

Boosting is a general approach that can be applied to many statistical learning methods for regression or classification (Friedman 1999). Given a training set, the goal is to find a function $y = f(x)$ such that a specified loss function is minimized. Boosting approximates $f(x)$ by an additive expansion of the form:

$$\hat{f}(x) = \sum_{m=0}^{M} \beta_m \, h(x, \theta_m), \tag{4.6}$$

where the functions $h(x, \theta_m)$ are simply functions of x parameterized by θ_m. $h(x, \theta_m)$ are called "base learners" or "weak learners" (Friedman, 1999). The expansion coefficients β_m and the parameters θ_m are fit to the training data in a forward "stage wise" manner (i.e. without adjusting the previous expansion coefficients and parameters of the base learners that have already been added).

In this work, we restrict the application of boosting to the context of regression trees (i.e. the base learner $h(x, \theta)$ is a tree $T(\theta)$). For that purpose, boosting builds an ensemble of trees iteratively in order to optimize a loss function Ψ, which we chosen to be MSE here. The generic gradient tree boosting algorithm (Friedman, 1999) is depicted below. The training set contains N samples (x_i, y_i), $i = 1, 2, ..., N$.

1. Initialize $f(x)$ to be a constant, $\widehat{f_O}(x) = argmin_\gamma [\sum_{i=1}^{N} \Psi\,(y_i, \gamma)]$
2. For m $= 1$ to M

1) Compute the negative gradient of the loss function Ψ (also called the pseudo-residuals $\widetilde{y_{im}}$)

$$\widetilde{y_{im}} = -\left[\frac{\partial \Psi(y_i, f(x_i))}{\partial f(x_i)}\right]_{f(x)=\widehat{f_{m-1}}(x)}, i = 1, \cdots, N$$

2) Fit a tree $T(\theta)$ with d splits predicting the pseudo-residuals $\widetilde{y_{im}}$ from covariate x. $T(\theta)$ partitions the input space into $L = d + 1$ distinct regions R_{lm}.

3) Compute the optimal node predictions, $l = 1, \cdots, L$, $\gamma_{lm} = \operatorname{argmin}_{\gamma}\left[\sum_{x_i \in R_{lm}} \Psi\,(y_i, f_{m-1}(x_i) + \gamma)\right]$

4) Update the estimates of f(x): $\widehat{f_m}(x) = \widehat{f_{m-1}}(x) + \nu.\gamma_{lm}\mathbb{I}_{\{x \in R_{lm}\}}$.

3. EndFor

Similar to RFs, once a boosted tree is grown, a prediction $\widehat{y(x)}$ for a new data point is obtained by averaging the predictions of the M single trees. As the loss function Ψ is the MSE, the tree that best fits the residuals $\widetilde{y_{im}} = r_{im} = y_i - f_{m-1}(x_i)$ is added at each step.

In this work, we used the XGboost R package (Ridgeway 2007) that proposes, among others, an ad1ditional improvement based on a regularized learning objective in order to prevent overfitting. The interested readers are referred to Chen and Guestrin (2016) for details regarding the derivation of this variant.

Unlike RFs, due to model complexity Gradient boosting models must be tuned carefully to prevent overfitting. Some tuning parameters or hyperparameters are adjustable by the user to control the model complexity, including M, υ, d:

1. M is the number of trees (or iterations). Unlike random forests, boosting can overfit if M is too large. One can use cross-validation to optimize M.

2. υ is the shrinkage parameter (see line 2.4 of the generic algorithm above). This parameter controls how fast boosting learns. Typical values are 0.01 or 0.001 and the choice depends on the specific problem. Smaller values of υ require larger numbers of iterations (M) to converge.

3. d is the number of splits (also called the interaction or maximum depth) in each tree, which controls the complexity of the boosted ensemble.

In this work, the parameters were set to $d = 2$, $M = 5000$, and $\upsilon = 0.001$ to design a model that makes a reasonable trade-off between complexity and predictive power.

Finally, like RFs, the XGboost package provides a specific metric to rank the input features according to their impact on predicting the model's response. The XGboost package also offers additional control parameters related to the regularization terms (see Chen and He 2015 for details).

4.2.5. Training and Evaluation

As different meteorological variables are measured on different scales, we normalize all feature values to range between -1 and 1 as

$$feature_{normalized} = \frac{feature - min\,(feature)}{max(feature) - min\,(feature)} \quad (4.7)$$

To achieve the best model performance and a better understanding of the data, we implemented the sequential backward elimination to find the optimal subset of features. The backward elimination removes one feature at a time from the full set of features until removing more features does not reduce the MSE (Guyon and Elisseeff, 2003).

The model prediction is evaluated by calculating the root mean square error, and the associated skill score (SS):

$$RMSE = \sqrt[2]{\frac{\sum_{i=1}^{l}(f(x_i) - y_i)^2}{l}} \quad (4.8)$$

$$SS = 1 - \frac{RMSE\ forecast}{RMSE_{ref}}, \quad (4.9)$$

where $RMSE_{\text{forecast}}$ is the $RMSE$ of forecast and $RMSE_{\text{ref}}$ is reference forecast which is the 24-hour persistence forecast. While kt removes diurnal and seasonal effects to focus on the ability to forecast cloud cover, since solar power generation depends more on GHI, the error metrics are also computed for GHI. The forecasted GHI is obtained from kt using the clear sky model.

4.3. Results and Discussion

4.3.1. Comparisons of Spatial error distribution

Figure 4.7 presents the spatial kt and GHI RMSE and SS of the four machine learning models, WRF, NAM and 24-hours persistence as well as SolarAnywhere data averaged from 6 PST to 17 PST. The SolarAnywhere average kt shows that the coastal region is more cloudy than the inland areas. As WRF and NAM tend to underpredict clouds, their RMSE are larger over the coast where clouds are more prevalent while

RMSE decreases farther from the coast. Compared to WRF and NAM, the simple 24-hours persistence has smaller kt RMSE but GHI RMSE is close or even higher for some regions, which may due to large day to day variation before and after some extreme cloud events (e.g. June 11, 2016, will be discussed in next section). All four machine learning models outperform WRF, NAM and 24-hours persistence forecasts and the differences between them are small (see Table 4.3).

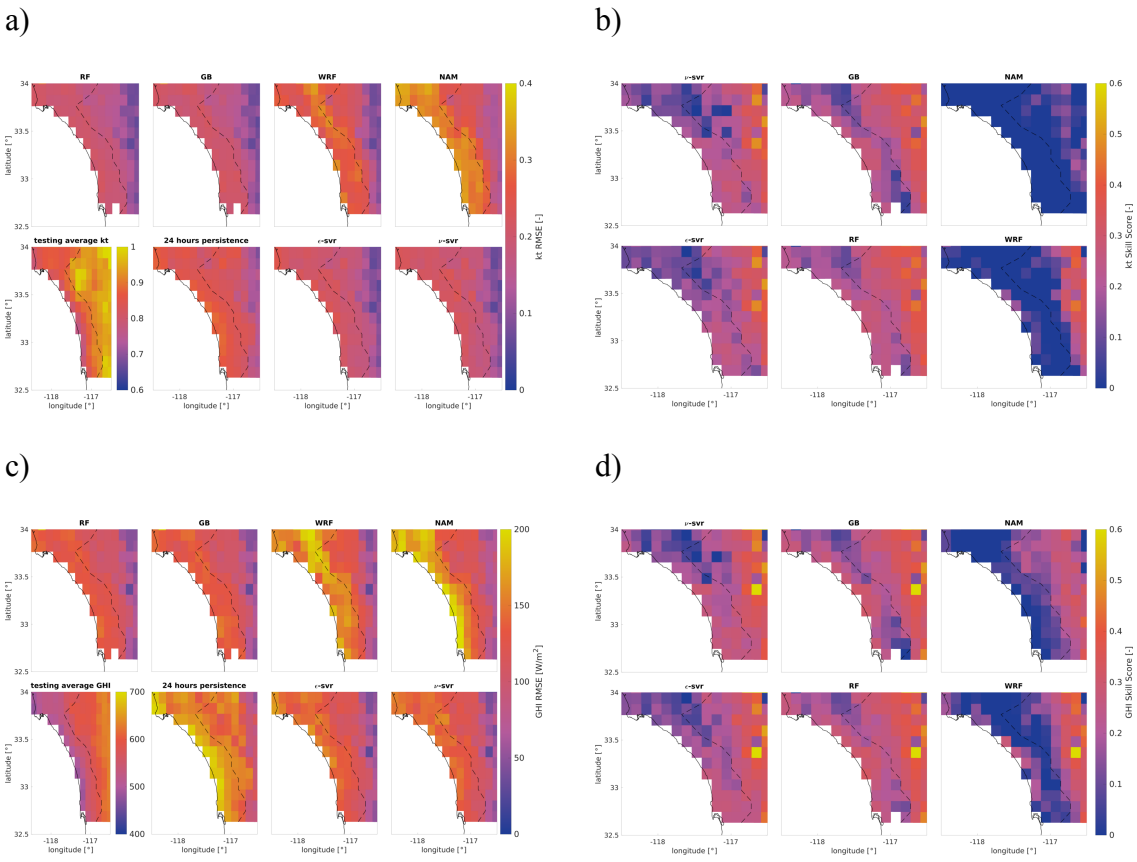

Figure 4.7: RMSE and RMSE skill score for kt (a,b) and GHI (c,d) averaged from 14 UTC (6 PST) to 25 UTC (17 UTC) for all the testing days. And the boundary of the marine layer region is marked by the black dashed line.

Table 4.3 Average kt and GHI RMSE and SS over the entire domain and marine layer region.

Model Name	Entire domain average				Marine layer region average			
	kt RMSE [-]	kt SS [-]	GHI RMSE [W/m2]	GHI SS [-]	kt RMSE [-]	kt SS [-]	GHI RMSE [W/m2]	GHI SS [-]
ϵ-SVR	0.17	0.22	112.39	0.23	0.21	0.17	137.52	0.17
υ-SVR	0.17	0.22	111.9	0.24	0.20	0.18	135.54	0.18
RF	**0.16**	**0.26**	**105.6**	**0.28**	**0.20**	**0.21**	**129.04**	**0.22**
GB	0.17	0.24	108.31	0.26	0.20	0.18	133.00	0.19
WRF	0.21	0.03	129.05	0.12	0.27	-0.10	161.64	0.02
NAM	0.25	-0.14	129.21	0.12	0.31	-0.27	165.33	0.00
24-hours persistence	0.22		143.89		0.25		165.85	

4.3.2. Analysis for different hours of the day and different days

To better understand the temporal performance of the models, Figure 4.8 compares the average kt and GHI of all the forecasts at different hours of the day over the entire domain and marine layer region, respectively. The SolarAnywhere average kt increases from 14 UTC to 25 UTC, showing the process of clouds dissipation. In the morning time, WRF and NAM show the largest errors, while RF and GB perform best. After 20 UTC, all the models except for the 24-hour persistence shows similar error and the two SVM models are most accurate. The machine learning models provide the largest benefit over NWP models in the morning, as the meteorological observations before sunrise are more accurate than the initial conditions of the NWP models. Also, the selected meteorological variables contain in-depth information about cloud optical

properties and spatial coverage, which are very important for predicting solar radiation in southern California.

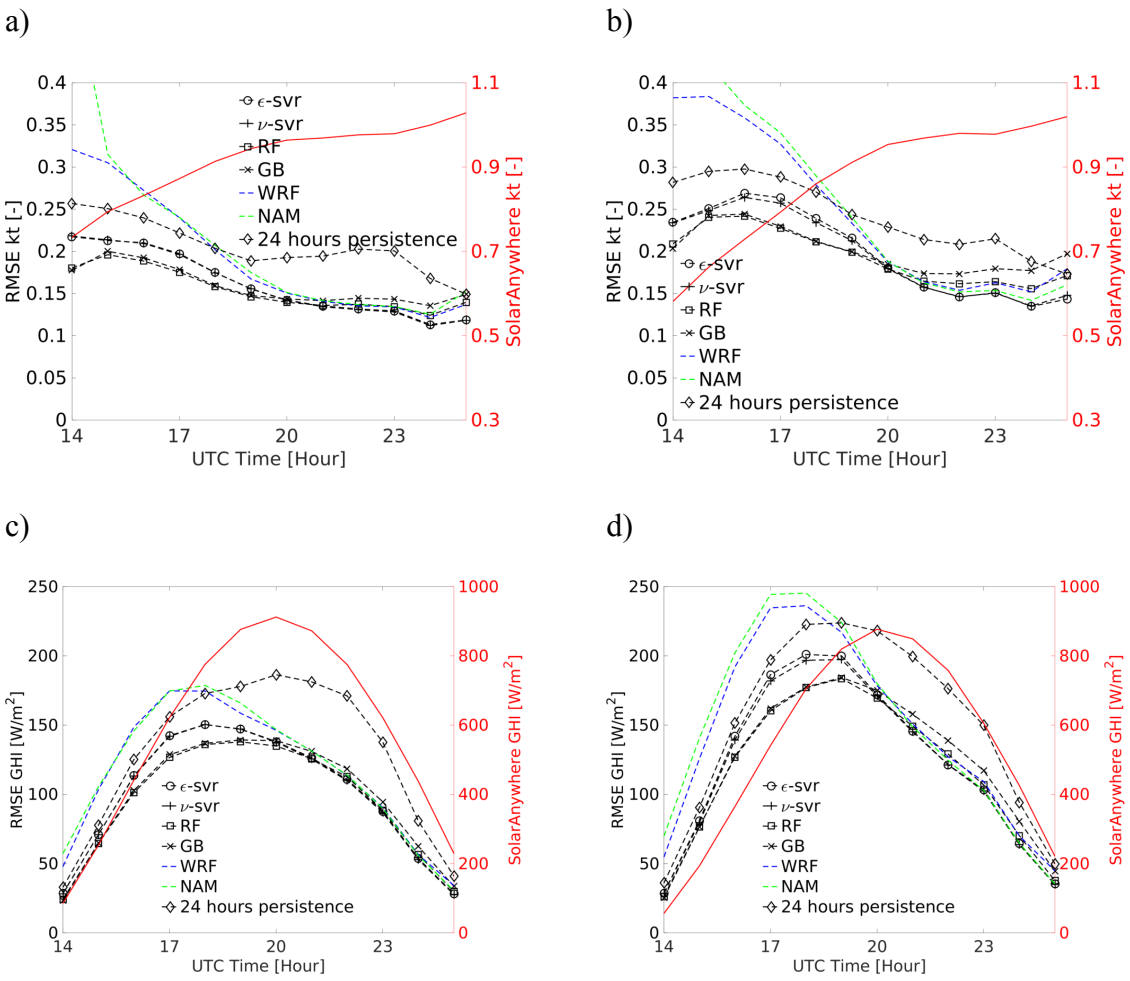

Figure 4.8: Timeseries of average kt and GHI over the entire domain (a, c) and the marine layer region (b, d) at different hours of the day during all testing days.

Figure 4.9 illustrates the domain average kt and GHI at 15 and 20 UTC on all validation days. Figure 4.9 a and c show that all machine learning models predict kt and GHI at 15 UTC accurately. However, Figure 4.9 b and d shows that at 20 UTC, RF and GB tend to overpredict clouds while the two SVM models underpredict clouds. This poor performance of machine learning models is not unexpected as the correlation between kt

in the afternoon and features in the morning is low (see Figure 4.3). There is also one outlier day shown on Figure 4.9 b and d, which is June 11, 2016 (day 24 in the figure). On June 11, 2016, widespread cloud cover persisted through the day. None of the models are able to accurately predict irradiance for the outlier day.

The NWS forecast discussions issued by human forecasters in both the LA/Oxnard and San Diego offices in the evening of June 10 suggest that the clouds are highly likely to persist for the entire next day due to strong Catalina eddy circulation and mid/upper level trough of low pressure system approaching the area. Figure 4.10 confirms that southerly winds and low pressure are observed by the two sounding stations for June 11, 2016, on which the domain average kt at 20 UTC is about 0.4. However, the models still fail to predict any afternoon cloud cover probably because of some other meteorological conditions are captured by the selected variables. The ground wind field measured by buoy and METAR stations (Figure 4.11) confirmed the strong Catalina eddy events. More research and data is needed to understand how to quantify how the size and strength of the Catalina eddy is related to cloud persistence.

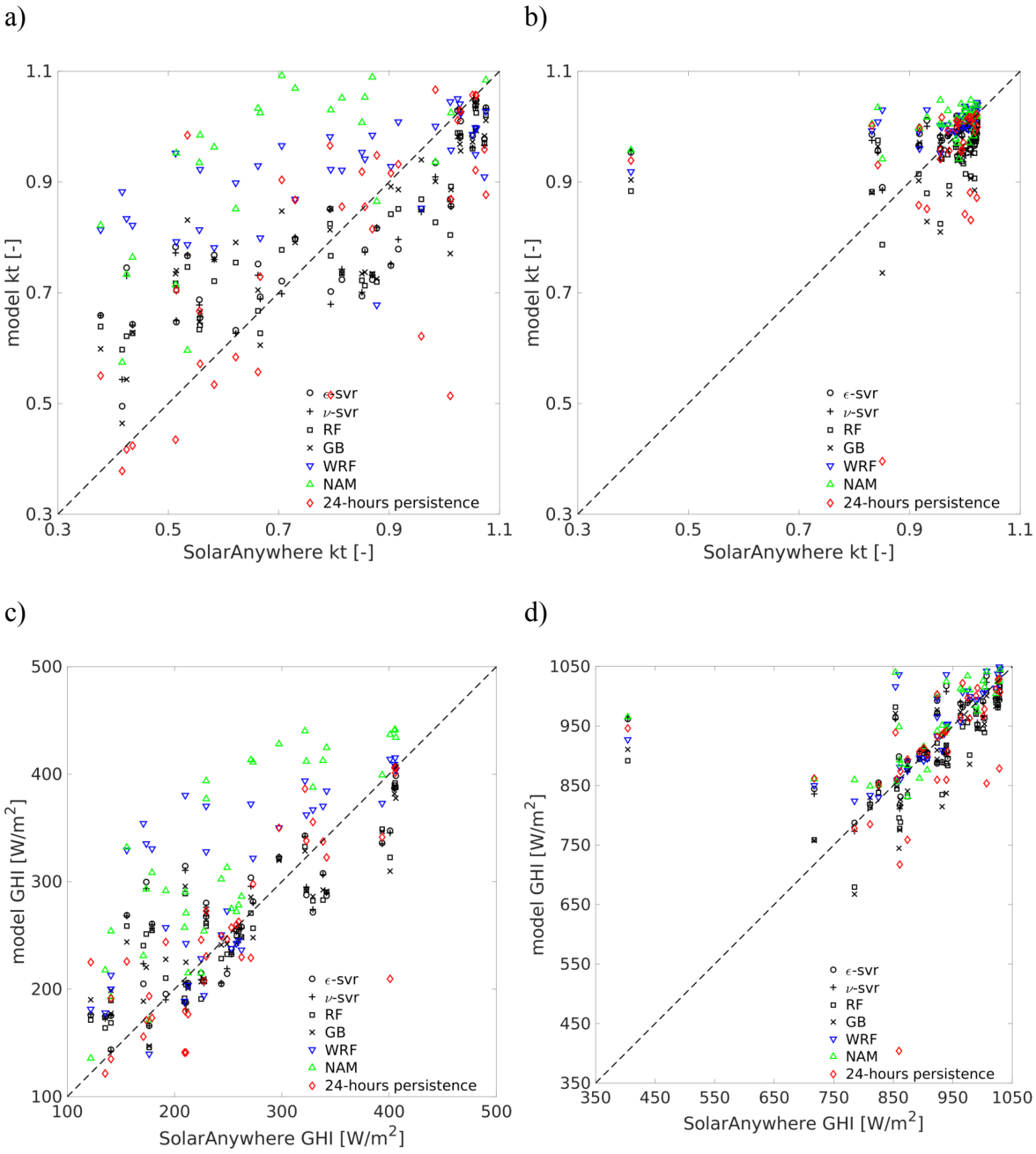

Figure 4.9: Average kt and GHI over the entire domain at 15 (a,c) and 20 UTC (b,d) against SolarAnywhere data for all testing days.

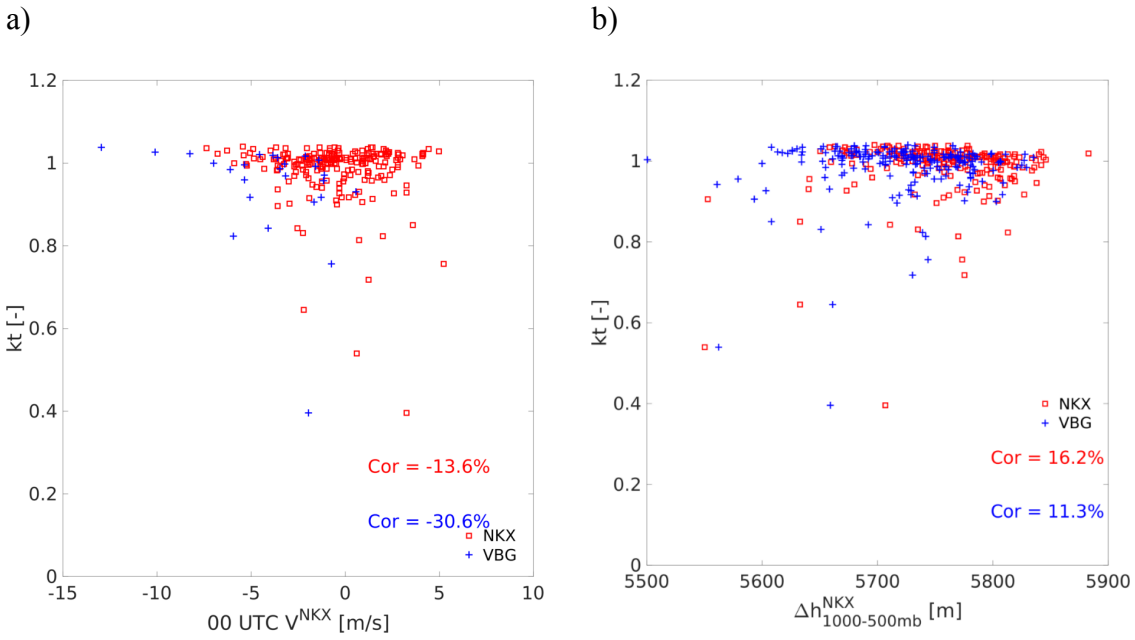

Figure 4.10: Plots of domain average kt at 20 UTC against 0 UTC V^{NKX} (a) and $\Delta h^{NKX}_{1000-500\,mb}$ (b) including both training and testing data. The day with the smallest kt = 0.4 is June 11, 2016.

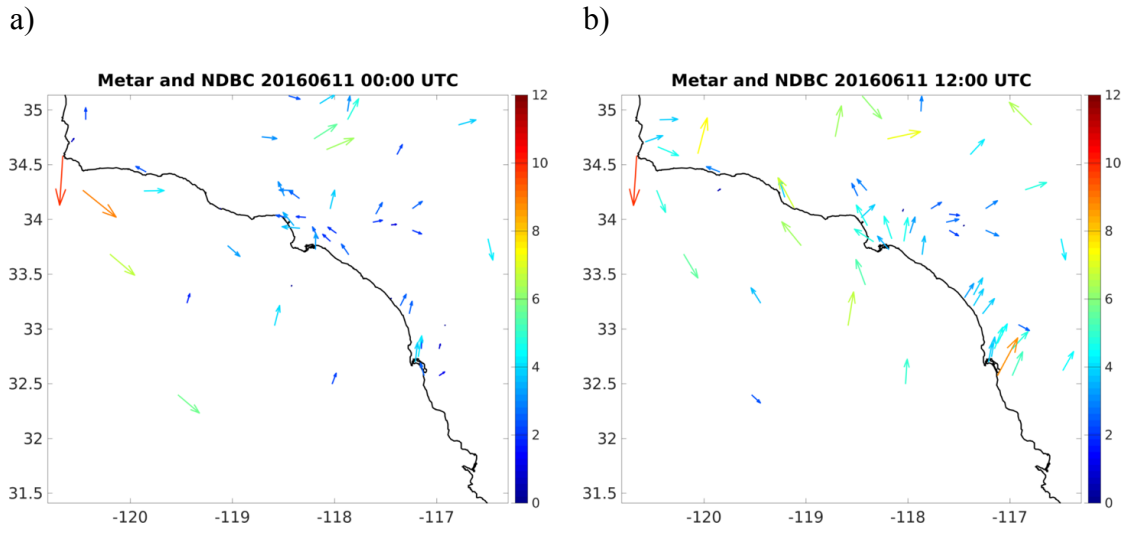

Figure 4.11: Surface wind field observed by buoy and METAR stations at 0 (a) and 12 (b) UTC on June 11, 2016. The color of the vector shows the 10 m wind speed.

4.3.3. Feature Selection and Importance

Although the total number of features is 22, not all the features are equally important for prediction. Fig. 12 illustrates the importance of the 12 most important variables using RF. We use this analysis both to confirm our physical and empirical insights presented in Section 2 as well as to allow us to develop new insight into which variables are important for solar forecasting. Due to the typical diurnal evolution of low clouds, the solar azimuth angle is the most important variable in all machine learning models. Over the coastal marine layer region, LWP^{NKX} is most important meteorological variable, which also indicates coastal marine layer are well mixed and LWP at one sounding station is representative of LWP along the coast. In the more inland region, IBH^{NKX} is weighted as the most important meteorological variable, as clouds can only penetrate to the inland region if IBH is greater than the land elevation. For the further inland area, $\Delta h^{NKX}_{1000-500\,mb}$ is the most important meteorological variable for predicting kt, which implies clouds over the further inland area are usually associated with low pressure systems.

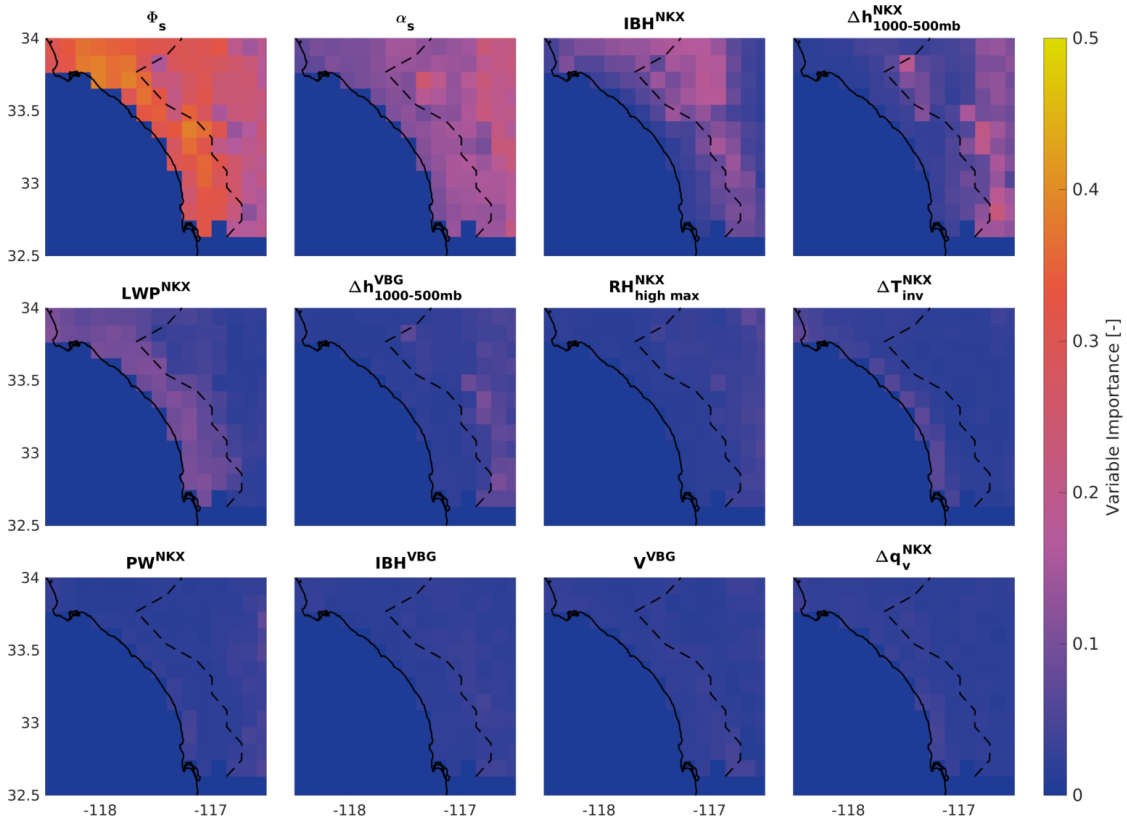

Figure 4.12: Spatial map of importance of different meteorological variables using RF. X-axis is longitude and y-axis is latitude. And the boundary of the marine layer region is marked by the black dashed line.

4.4. Conclusion

In this study, we selected meteorological variables that are important for the evolution of low clouds, the most common cloud type in southern California. All three machine learning models significantly outperform physics-based NWP models and 24-hour persistence in terms of prediction accuracy of solar radiation, especially during cloudy periods in the morning. In the afternoon, all the models perform similarly with the SVM model as best performer. The most important variables for RF and GR are found to be ϕ_s, α_s, LWP^{NKX}, IBH^{NKX}, and $\Delta h^{NKX}_{1000-500mb}$. Moreover, the outlier day on June 11, 2016 indicated that although Catalina eddy circulation is a valuable indicator for

persistent clouds, more research and data are needed to make better use of the Catalina eddy circulation for prediction.

Acknowledgements

Chapter 4, in part is currently being prepared for submission for publication of the material as it may appear in Zhong, X., Lauret, P., and Kleissl, J., 2017: Intra-day solar energy prediction using machine learning models with selected meteorological variables over southern California. *Solar Energy*, to be submitted. The dissertation/thesis author was the primary investigator and author of this paper.

5. Conclusion and Prospects of Future Development

To forecast solar irradiance/MBL stratocumulus over southern California, we used WRF and machine learning models. To overcome the positive biases of WRF models under clear sky conditions, we proposed an approach to isolate the effect of each atmospheric constituent in radiation schemes and applied it to WRF's New Goddard SW scheme (Chapter 2). The comparisons against WRF's RRTMG scheme shows that the incorrect ozone profile and missing absorption of water vapor continuum are the source of clear sky GHI errors in New Goddard SW scheme. We confirmed that the inland extent of cloud cover is dependent on the temperature inversion base height and topography using radiosonde sounding measurement and satellite irradiance data. In WRF model, we developed a method to modify the boundary layer temperature and moisture files to better represent boundary layer structure (Chapter 3). Also, we input IBH along with other meteorological variables of importance to evolution of MBL clouds into machine learning models and achieve higher prediction accuracies of GHI and kt than NWP models (Chapter 4).

Whether we use a physics based model or a data-driven model for solar forecasting over southern California, the key to success is to recognize the limitation of model used and to improve understanding of the MBL stratocumulus clouds. Firstly, initial and boundary conditions of a regional NWP model are usually derived from large-scale NWP models at coarser resolutions. It is inevitable that the regional NWP model will inherit errors from the large-scale NWP models. Although data assimilation of observations has been implemented to reduce these errors for those large-scale operational NWP models such as RAP and NAM, it is nearly impossible to have a prefect

initial and boundary conditions. As even the smallest changes in initial conditions can grow like a snowball with time, more and more scientist (Epstein 1969; Leith 1974) advocate generating an ensemble of forecasts with initial conditions within the range of uncertainty.

Secondly, NWP parametrization commonly are developed based on some simplifying assumptions, and tested and tuned using observational data under either idealized or specific environmental conditions. Therefore, when the parametrization scheme is applied for a more realistic or other environment for which they are not tested or tuned, the parametrization scheme may not work equally well as in testing stage. Additionally, the complex interactions among different parametrization make it hard to interpret the behavior of one parametrization scheme. Even though current parametrizations are typically far removed from the elemental atmospheric physics, parametrization schemes are necessary for capturing all natural processes in solar forecasting. Also, since the interactions among different physical parametrizations are so complicated, reducing forecast errors requires improvements not only to one scheme but also the consideration of feedback effects with other model components. Thirdly, I found the improvements to the parametrization schemes are not well documented and parametrization code are not well commented. It is harder for newbies to understand how parametrization works. I also found machine learning models much easier to learn as there are lot more resources available and people trying better to illustrate things that confuses people. To guarantee the future of NWP models continue to prosper, we need to improve the documentation of parametrization scheme and NWP code writing, and have more online resources. Overall, the improvement of NWP models requires collective

efforts from not only meteorologists but also computer scientist, statisticians, oceanographers, and scientists from other fields. We also need to continue to learn other sciences to improve NWP model forecasts.

Additionally, we are living in an era when Google's AlphaGo artificial intelligence (AI) Go player defeats the world's best human Go player, Sony's AI composes a Beatles-inspired song, "Daddy's Car", The Weather Company of IBM uses a machine learning model to predict power outage. Machine learning is pushing our imagination boundary and showing off its unprecedented learning ability in this century thanks to the explosively increasing amount of data. I think that the machine learning models will be more and more used to help us to understand complex weather phenomena and provide us with highly accurate forecast in the foreseeable future. The success of machine learning models in solar forecasting relies on whether the evolution of solar irradiances/clouds related variables are selected for input and whether enough historical data are available to learn the relations between input variables and target. In this thesis, we showed very promising results after we selected the meteorological variables important for predicting MBL stratocumulus clouds. I think there is still a large room for improvement if we include some variables account for the surface conditions and accurate measurements are available at higher temporal and spatial resolutions.

References

Antonanzas, J., N. Osorio, R. Escobar, R. Urraca, F. J. Martinez-de-pison, and F. Antonanzas-torres, 2016: Review of photovoltaic power forecasting. *Sol. Energy*, **136**, 78–111, doi:10.1016/j.solener.2016.06.069. http://dx.doi.org/10.1016/j.solener.2016.06.069.

Banks, R. F., J. Tiana-Alsina, F. Rocadenbosch, and J. M. Baldasano, 2015: Performance Evaluation of the Boundary-Layer Height from Lidar and the Weather Research and Forecasting Model at an Urban Coastal Site in the North-East Iberian Peninsula. *Boundary-Layer Meteorol.*, **157**, 265–292, doi:10.1007/s10546-015-0056-2. http://link.springer.com/10.1007/s10546-015-0056-2.

Blanc, P., and Coauthors, 2014: Direct normal irradiance related definitions and applications: The circumsolar issue. *Sol. Energy*, **110**, 561–577, doi:10.1016/j.solener.2014.10.001. http://linkinghub.elsevier.com/retrieve/pii/S0038092X14004824.

Bluma, A. L., and P. Langley, 1997: Selection of relevant features and examples in machine learning. *Artif. Intell.*, **97**, 245–271.

Bosart, L. F., 1983: Analysis of a California Catalina Eddy Event. *Mon. Weather Rev.*, **111**, 1619–1633.

Breiman, L., 2001: RANDOM FORESTS. Machine Learning, 45. 5–32.

Brenguier, B. J. L., P. Y. Chuang, Y. Fouquart, D. W. J. F. Parol, H. Pawlowska, J. Pelon, L. Schu, and J. S. Me, 2000: An overview of the ACE-2 CLOUDYCOLUMN closure experiment. 815–827.

Bretherton, C. S., and D. L. Hartmann, 2009: Large-scale Controls on Cloudiness. *Clouds in the Perturbed Climate System: Their Relationship to Energy Balance, Atmospheric Dynamics, and Precipitation*, J. Heintzenberg and R. Charlson, Eds., MIT Press, 217–234.

——, and Coauthors, 2004: The EPIC 2001 stratocumulus study. *Bull. Am. Meteorol. Soc.*, **85**, 967–977, doi:10.1175/BAMS-85-7-967.

Chang, C., and C. Lin, 2013: LIBSVM : A Library for Support Vector Machines. 1–39. http://www.csie.ntu.edu.tw/~cjlin/papers/libsvm.pdf.

Charney, J. G., J. Fjortoft, and J. Von Neumann, 1950: Numerical Integration of the Barotropic Vorticity Equation. *A Q. J. Geophys.*, **2**, 237–254.

Chen, J., G. Li, and S. Wu, 2013: Assessing the potential of support vector machine for estimating daily solar radiation using sunshine duration. *Energy Convers. Manag.*,

75, 311–318, doi:10.1016/j.enconman.2013.06.034. http://dx.doi.org/10.1016/j.enconman.2013.06.034.

Chen, T., and T. He, 2015: xgboost : eXtreme Gradient Boosting. R package version 0.4-2. 1–4.

——, and C. Guestrin, 2016: XGBoost : A Scalable Tree Boosting System. *ArXiv e-prints*.

Chou, M.-D., 1990: Parameterizations for the Absorption of Solar Radiation by O2 and CO2 with Application to Climate Studies. *J. Clim.*, **3**, 209–217.

Chou, M. D., 1992: A Solar Radiation Model for use in Climate Studies. *J. Atmos. Sci.*, **49**, 762–772. http://journals.ametsoc.org/doi/abs/10.1175/1520-0469(1992)049%3C0762:ASRMFU%3E2.0.CO;2.

——, and K. T. Lee, 1996: Parametrizations for the Absorption of Solar Radiation by Water Vapour and Ozone. *J. Atmos. Sci.*, **53**, 1203–1208.

——, and M. J. Suarez, 1999: *Technical Report Series on Global Modeling and Data Assimilation Volume 15: A Solar Radiation Parameterization for Atmospheric Studies NASA. Tech. Rep. Series on Global Modeling and Data Assimilation, NASA/TM-1999- 104606, Vol. 15, 40 pp.*

Clough, S. A., F. X. Kneizys, and R. W. Davies, 1989: Line shape and the water vapor continuum. *Atmos. Res.*, **23**, 229–241, doi:10.1016/0169-8095(89)90020-3.

Clough, S. A., M. J. Iacono, and J. Moncet, 1992: Line-by-line calculations of atmospheric fluxes and cooling rates: Application to water vapor. *J. Geophys. Res.*, **97**, 15761, doi:10.1029/92JD01419.

Clough, S. A., M. W. Shephard, E. J. Mlawer, J. S. Delamere, M. J. Iacono, K. Cady-Pereira, S. Boukabara, and P. D. Brown, 2005: Atmospheric radiative transfer modeling: a summary of the AER codes. *J. Quant. Spectrosc. Radiat. Transf.*, **91**, 233–244, doi:10.1016/j.jqsrt.2004.05.058. http://linkinghub.elsevier.com/retrieve/pii/S0022407304002158.

Daniel, J. S., 2004: Atmospheric water vapor complexes and the continuum. *Geophys. Res. Lett.*, **31**, 1–4, doi:10.1029/2003GL018914.

Davis, C., and S. Low-Nam, 2000: Dynamics of a Catalina Eddy Revealed by Numerical Simulation. *Mon. Weather Rev.*, **128**, 2885–2904.

Done, J., C. A. Davis, and M. Weisman, 2004: The next generation of NWP: Explicit forecasts of convection using the weather research and forecasting (WRF) model. *Atmos. Sci. Lett.*, **5**, 110–117, doi:10.1002/asl.72.

Eastman, R., S. G. Warren, and C. J. Hahn, 2011: Variations in Cloud Cover and Cloud Types over the Ocean from Surface Observations, 1954–2008. *J. Clim.*, **24**, 5914–5934, doi:10.1175/2011JCLI3972.1.

Ek, M. B., K. E. Mitchell, Y. Lin, E. Rogers, P. Grunmann, V. Koren, G. Gayno, and J. D. Tarpley, 2003: Implementation of Noah land surface model advances in the National Centers for Environmental Prediction operational mesoscale Eta model. *J. Geophys. Res.*, **108**, doi:10.1029/2002JD003296. http://doi.wiley.com/10.1029/2002JD003296.

Epstein, E. S., 1969: Stochastic dynamic prediction. *Tellus*, 739–759.

Feng, Z., Z. Qingcun, Y. Gu, and K. N. Liou, 2005: Parameterization of the absorption of the H2O continuum, CO2, O2, and Other Trace Gases in the Fu-Liou Solar Radiation Program. *Adv. Atmos. Sci.*, **22**, 545–558, doi:10.1128/mBio.01383-14.Editor.

Friedman, J. H., 1999: *Stochastic Gradient Boosting, technical report*.

Ghonima, A. M. S., T. Heus, J. R. Norris, and J. Kleissl, 2016a: Factors controlling Stratocumulus cloud lifetime over the coast. *J. Atmos. Sci.*,.

——, H. Yang, C. K. Kim, T. Heus, and J. Kleissl, 2016b: Evaluation of WRF SCM simulations of a stratocumulus topped marine boundary layers and proposed correction to improve entrainment parameterization.

Gilliland, E. K., and C. M. Rowe, 2007: A comparison of cumulus parameterization schemes in the WRF model. *Preprints, 21st Conference on Hydrology*, San Antonio, TX.

Gueymard, C. a., and J. A. Ruiz-Arias, 2015: Validation of direct normal irradiance predictions under arid conditions: A review of radiative models and their turbidity-dependent performance. *Renew. Sustain. Energy Rev.*, **45**, 379–396, doi:10.1016/j.rser.2015.01.065. http://linkinghub.elsevier.com/retrieve/pii/S1364032115000751.

Gueymard, C. A., 2001: Parameterized transmittance model for direct beam and circumsolar spectral irradiance. *Sol. Energy*, **71**, 325–346, doi:10.1016/S0038-092X(01)00054-8.

——, 2008: REST2: High-performance solar radiation model for cloudless-sky irradiance, illuminance, and photosynthetically active radiation – Validation with a benchmark dataset. *Sol. Energy*, **82**, 272–285, doi:10.1016/j.solener.2007.04.008.

——, 2012: Clear-sky irradiance predictions for solar resource mapping and large-scale applications: Improved validation methodology and detailed performance analysis of 18 broadband radiative models. *Sol. Energy*, **86**, 2145–2169,

doi:10.1016/j.solener.2011.11.011.

Guyon, I., and A. Elisseeff, 2003: An Introduction to Variable and Feature Selection. *J. Mach. Learn. Res.*, **3**, 1157–1182.

Hahn, C. J., and S. G. Warren, 2007: *A gridded climatology of clouds over land (1971-96) and ocean (1954-97) from surface observations worldwide. Numeric Data Package NDP-026E ORNL/CDIAC-153, CDIAC, Department of Energy, Oak Ridge, TN.*

Han, J., and H. L. Pan, 2011: Revision of Convection and Vertical Diffusion Schemes in the NCEP Global Forecast System. *Weather Forecast.*, **26**, 520–533, doi:10.1175/WAF-D-10-05038.1.

Hannay, C., D. L. Williamson, J. J. Hack, J. T. Kiehl, J. G. Olson, S. A. Klein, C. S. Bretherton, and M. Kohler, 2009: Evaluation of Forecasted Southeast Pacific Stratocumulus in the NCAR, GFDL, and ECMWF Models. *J. Clim.*, **22**, 2871–2889, doi:10.1175/2008JCLI2479.1.

Hartmann, D. L., M. E. Ockert-Bell, and M. L. Michelsen, 1992: The effect of cloud type on Earth's energy balance: results for selected regions. *J. Clim.*, **5**, 1281–1304, doi:10.1175/1520-0442(1992)005<1281:TEOCTO>2.0.CO;2.

Hastie, T., R. Tibshirani, and J. Friedman, 2009: *The Elements of Statistical Learning*. 2nd ed. Springer, New York, https://link.springer.com/book/10.1007%2F978-0-387-84858-7.

Hewitt, C. N., and A. V. Jackson, 2009: *Atmospheric Science for Environmental Scientists*.

Hsu, C., C. Chang, and C. Lin, 2003: A Practical Guide to Support Vector Classification. **1**, 1–16.

Hu, X. M., J. W. Nielsen-Gammon, and F. Zhang, 2010: Evaluation of three planetary boundary layer schemes in the WRF model. *J. Appl. Meteorol. Climatol.*, **49**, 1831–1844, doi:10.1175/2010JAMC2432.1.

Iacobellis, S. F., and D. R. Cayan, 2013a: The variability of California summertime marine stratus: Impacts on surface air temperatures. *J. Geophys. Res. Atmos.*, **118**, 9105–9122, doi:10.1002/jgrd.50652.

——, and ——, 2013b: The variability of California summertime marine stratus: Impacts on surface air temperatures. *J. Geophys. Res. Atmos.*, **118**, 9105–9122, doi:10.1002/jgrd.50652. http://doi.wiley.com/10.1002/jgrd.50652 (Accessed May 8, 2014).

Iacobellis, S. F., J. R. Norris, M. Tyree, and R. Daniel, 2009: *Climate Variability and*

California Low-Level Temperature Inversions. California Climate Change Center, Publication # CEC-500-2009- 020-F. http://www.energy.ca.gov/2009publications/CEC-500-2009-020/CEC-500-2009-020-F.PDF.

Iacono, M. J., J. S. Delamere, E. J. Mlawer, M. W. Shephard, S. a. Clough, and W. D. Collins, 2008: Radiative forcing by long-lived greenhouse gases: Calculations with the AER radiative transfer models. *J. Geophys. Res. Atmos.*, **113**, 1–8, doi:10.1029/2008JD009944.

Ineichen, P., 2008: A broadband simplified version of the Solis clear sky model. *Sol. Energy*, **82**, 758–762, doi:10.1016/j.solener.2008.02.009. http://linkinghub.elsevier.com/retrieve/pii/S0038092X08000406 (Accessed January 10, 2013).

——, and R. Perez, 2002: A new airmass independent formulation for the Linke turbidity coefficient. *Sol. Energy*, **73**, 151–157, doi:10.1016/S0038-092X(02)00045-2. http://linkinghub.elsevier.com/retrieve/pii/S0038092X02000452.

Jamaly, M., and J. Kleissl, 2012: *Validation of SolarAnywhere Enhanced Resolution Irradiation Using Power Output of Distributed PV Systems in California. Report to the California Solar Initiative RD&D Program*.

——, J. L. Bosch, and J. Kleissl, 2013: Aggregate ramp rates of distributed photovoltaic systems in San Diego county. *IEEE Trans. Sustain. Energy*, **4**, 519–526, doi:10.1109/TSTE.2012.2201966.

Jimenez, P. A., and Coauthors, 2015: WRF-Solar: An augmented NWP model for solar power prediction. Model description and clear sky assessment. *Bull. Am. Meteorol. Soc.*, doi:10.1175/BAMS-D-14-00279.1. http://journals.ametsoc.org/doi/abs/10.1175/BAMS-D-14-00279.1.

Joseph, J. H., W. J. Wiscombe, and J. A. Weinman, 1976: The Delta-Eddington Approximation for Radiative Flux Transfer. *J. Atmos. Sci.*, **33**, 2452–2459.

Jousse, A., A. Hall, F. Sun, and J. Teixeira, 2016: Causes of WRF surface energy fluxes biases in a stratocumulus region. *Clim. Dyn.*, **46**, 571–584, doi:10.1007/s00382-015-2599-9. http://link.springer.com/article/10.1007/s00382-015-2599-9.

Kann, A., H. Seidl, C. Wittmann, and T. Haiden, 2009: Advances in Predicting Continental Low Stratus with a Regional NWP Model. *Weather Forecast.*, **25**, 290–302, doi:10.1175/2009WAF2222314.1.

King, M. D., and Harshvardhan, 1986: Comparative Aaccuracy of Selected Multiple Scattering Approximations. *J. Atmos. Sci.*, **43**, 784–801.

Klein, S. A., and D. L. Hartmann, 1993: The Seasonal Cycle of Low Stratiform Clouds.

J. Clim., **6**, 1587–1606.

Koračin, D., J. Poweres, M. Wetzel, S. Chai, and N. Adhikari, 2003: IMPROVING PREDICTION OF THE MARINE COASTAL CLOUDS USING SATELLITE AND AIRCRAFT DATA. *Fifth Conference on Coastal Atmospheric Prediction and Processes*, Seattle, WA., 139–140.

Lara-Fanego, V., J. A. Ruiz-Arias, D. Pozo-Vázquez, F. J. Santos-Alamillos, and J. Tovar-Pescador, 2011: Evaluation of the WRF model solar irradiance forecasts in Andalusia (southern Spain). *Sol. Energy*, **86**, 2200–2217, doi:10.1016/j.solener.2011.02.014.

Lauret, P., C. Voyant, T. Soubdhan, M. David, and P. Poggi, 2015: A benchmarking of machine learning techniques for solar radiation forecasting in an insular context. *Sol. ENERGY*, **112**, 446–457, doi:10.1016/j.solener.2014.12.014. http://dx.doi.org/10.1016/j.solener.2014.12.014.

Leith, C. E., 1974: Theoretical Skills of Monte Carlo Forecasts.pdf. *Mon. Weather Rev.*, **102**, 409–418.

Liaw, A., and M. Wiener, 2002: Classification and Regression by randomForest. *R News*, **2/3**, 18–22.

Lilly, D., 1968: Models of cloud-topped mixed layers under a strong inversion. *Q. J. R. Meteorol. Soc.*, **94**, 292–309, doi:10.1002/qj.49709440106. http://onlinelibrary.wiley.com/doi/10.1002/qj.49709440106/abstract.

López-Coto, I., J. L. Bosch, P. Mathiensen, and J. Kleissl, 2014: COMPARISON BETWEEN SEVERAL PARAMETERIZATION SCHEMES IN WRF FOR SOLAR FORECASTING IN COASTAL ZONES. *ASES*.

Lorenz, E., J. Hurka, D. Heinemann, and H. G. Beyer, 2009: Irradiance forecasting for the power prediction of grid-connected photovoltaic systems. *IEEE J. Sel. Top. Appl. Earth Obs. Remote Sens.*, **2**, 2–10, doi:10.1109/JSTARS.2009.2020300.

Mass, C. F., and M. D. Albright, 1989: Origin of Catalina Eddy. *Mon. Weather Rev.*, **117**, 2406–2436.

Mathiesen, P., and J. Kleissl, 2011: Evaluation of numerical weather prediction for intra-day solar forecasting in the continental United States. *Sol. Energy*, **85**, 967–977, doi:10.1016/j.solener.2011.02.013.

Mathiesen, P., C. Craig, and J. Kleissl, 2013: A high-resolution, cloud-assimilating numerical weather prediction model for solar irradiance forecasting. *Sol. Energy*, **92**, 47–61, doi:10.1016/j.solener.2013.02.018. http://dx.doi.org/10.1016/j.solener.2013.02.018.

Mlawer, E. J., and S. A. Clough, 1997: On the Extension of Rapid Radiative Transfer Model to the Shortwave Region. *Proceedings of the 6th Atmospheric Radiation Measurement (ARM) Science Team Meeting*.

——, and ——, 1998: Shortwave and longwave enhancements in the rapid radiative transfer model. *Proceedings of the 7th Atmospheric Radiation Measurement (ARM) Science Team Meeting* http://www.arm.gov/publications/proceedings/conf07/extended_abs/mlawer_ej.pdf?i.

Mlawer, E. J., S. J. Taubman, P. D. Brown, M. J. Iacono, and S. a. Clough, 1997: Radiative transfer for inhomogeneous atmospheres: RRTM, a validated correlated-k model for the longwave. *J. Geophys. Res.*, **102**, 16663–16682, doi:10.1029/97JD00237.

Montornès, A., B. Codina, and J. W. Zack, 2015: Analysis of the ozone profile specifications in the WRF-ARW model and their impact on the simulation of direct solar radiation. *Atmos. Chem. Phys.*, **15**, 2693–2707, doi:10.5194/acp-15-2693-2015. http://www.atmos-chem-phys.net/15/2693/2015/.

Morrison, H., G. Thompson, and V. Tatarskii, 2009: Impact of Cloud Microphysics on the Development of Trailing Stratiform Precipitation in a Simulated Squall Line: Comparison of One- and Two-Moment Schemes. *Mon. Weather Rev.*, **137**, 991–1007, doi:10.1175/2008MWR2556.1.

Myers, T. a., and J. R. Norris, 2013: Observational Evidence That Enhanced Subsidence Reduces Subtropical Marine Boundary Layer Cloudiness. *J. Clim.*, **26**, 7507–7524, doi:10.1175/JCLI-D-12-00736.1. http://journals.ametsoc.org/doi/abs/10.1175/JCLI-D-12-00736.1 (Accessed May 26, 2014).

Nakanishi, M., and H. Niino, 2006: An improved Mellor-Yamada Level-3 model: Its numerical stability and application to a regional prediction of advection fog. *Boundary-Layer Meteorol.*, **119**, 397–407, doi:10.1007/s10546-005-9030-8.

Nielsen-Gammon, J. W., and Coauthors, 2008: Multisensor estimation of mixing heights over a coastal city. *J. Appl. Meteorol. Climatol.*, **47**, 27–43, doi:10.1175/2007JAMC1503.1.

Pedro, H. T. C., and C. F. M. Coimbra, 2017: Assessment of forecasting techniques for solar power production with no exogenous inputs. *Sol. Energy*, **86**, 2017–2028, doi:10.1016/j.solener.2012.04.004. http://dx.doi.org/10.1016/j.solener.2012.04.004.

Perez, R., P. Ineichen, K. Moore, M. Kmiecik, C. Chain, R. George, and F. Vignola, 2002: A new operational model for satellite-derived irradiances: description and Validation. *Sol. Energy*, **73**, 307–317, doi:10.1016/S0038-092X(02)00122-6.

Rahn, D. A., and R. Garreaud, 2010a: Marine boundary layer over the subtropical southeast Pacific during VOCALS-REx – Part 1: Mean structure and diurnal cycle. *Atmos. Chem. Phys.*, **10**, 4491–4506, doi:10.5194/acp-10-4491-2010. http://www.atmos-chem-phys.net/10/4491/2010/.

——, and ——, 2010b: Marine boundary layer over the subtropical southeast Pacific during VOCALS-REx – Part 2: Synoptic variability. *Atmos. Chem. Phys.*, **10**, 4507–4519, doi:10.5194/acp-10-4507-2010. http://www.atmos-chem-phys.net/10/4507/2010/.

Remund, J., R. Perez, and E. Lorenz, 2008: Comparison of solar radiation forecasts for the USA. *European PV Conference*, Valencia, Spain http://www.task34.iea-shc.org/data/sites/1/publications/Comparison_of_USA_radiation_forecasts.pdf.

Ricchiazzi, P., S. Yang, C. Gautier, and D. Sowle, 1998: SBDART: A Research and Teaching Software Tool for Plane-Parallel Radiative Transfer in the Earth's Atmosphere. *Bull. Am. Meteorol. Soc.*, **79**, 2101–2114.

Ridgeway, G., 2007: Generalized Boosted Models : A guide to the gbm package. http://www.saedsayad.com/docs/gbm2.pdf.

Rothman, L. S., and Coauthors, 1992: The HITRAN molecular database: Editions of 1991 and 1992. *J. Quant. Spectrosc. Radiat. Transf.*, **48**, 469–507, doi:10.1016/0022-4073(92)90115-K. http://linkinghub.elsevier.com/retrieve/pii/002240739290115K.

Ruiz-Arias, J. A., C. A. Gueymard, J. Dudhia, and D. Pozo-vázquez, 2012: IMPROVEMENT OF THE WEATHER RESEARCH AND FORECASTING (WRF) MODEL FOR SOLAR RESOURCE ASSESSMENTS AND FORECASTS UNDER CLEAR SKIES. *World Renewable Energy ForumWorld Renewable Energy Forum*, Denver, CO.

Ruiz-Arias, J. A., J. Dudhia, F. J. Santos-Alamillos, and D. Pozo-Vázquez, 2013: Surface clear-sky shortwave radiative closure intercomparisons in the Weather Research and Forecasting model. *J. Geophys. Res. Atmos.*, **118**, 9901–9913, doi:10.1002/jgrd.50778.

Ruiz-Arias, J. A., J. Dudhia, and C. A. Gueymard, 2014: A simple parameterization of the short-wave aerosol optical properties for surface direct and diffuse irradiances assessment in a numerical weather model. *Geosci. Model Dev.*, **7**, 1159–1174, doi:10.5194/gmd-7-1159-2014.

Ruiz-Arias, J. A., C. A. Gueymard, F. J. Santos-Alamillos, and D. Pozo-Vázquez, 2015: Do spaceborne aerosol observations limit the accuracy of modeled surface solar irradiance? *Geophys. Res. Lett.*, 2014GL062309, doi:10.1002/2014GL062309. http://dx.doi.org/10.1002/2014GL062309.

Sharma, N., P. Sharma, D. Irwin, and P. Shenoy, 2011: Predicting Solar Generation from Weather Forecasts Using Machine Learning. *IEEE SmartGridComm*, 528–533.

Shi, J. J., T. Matsui, W.-K. Tao, M. Chin, and C. Peters-Lidard, 2007: Implementation of the Updated Goddard Longwave and Shortwave Radiation Packages into WRF. *WRF User Workshop*.

Shine, K. P., I. V. Ptashnik, and G. Rädel, 2012: The Water Vapour Continuum: Brief History and Recent Developments. *Surv. Geophys.*, **33**, 535–555, doi:10.1007/s10712-011-9170-y.

Skamarock, W. C., and Coauthors, 2008: *A Description of the Advanced Research WRF Version 3. NCAR TECHNICAL NOTE NCAR/TN–475+STR*.

Smola, A. J., and B. Schölkopf, 2004: A tutorial on support vector regression. *Stat. Comput.*, **14**, 199–222.

Stensrud, D. J., 2009: *Parameterization Schemes: Keys to Understanding Numerical Weather Prediction Models*. Cambridge University Press,.

Tarasova, T. A., and B. A. Fomin, 2000: Solar Radiation Absorption due to Water Vapor: Advanced Broadband Parameterizations. *J. Appl. Meteorol.*, **39**, 1947–1951, doi:10.1175/1520-0450(2000)039<1947:SRADTW>2.0.CO;2.

Twomey, S., 1974: Pollution and the Planetary Albedo. *Atmos. Environ.*, **8**, 1251–1256, doi:10.1016/j.atmosenv.2007.10.062.

——, 1977: The Infulence of Pollution on the Shortwave Albedo of Clouds. *J. Atmos. Sci.*, **34**, 1149–1152.

Vapnik, V. N., 1995: *The Nature of Statistical Learning Theory*. Springer,.

Weisman, M. L., W. C. Skamarock, and J. B. Klemp, 1997: The Resolution Dependence of Explicitly Modeled Convective Systems. *Mon. Weather Rev.*, **125**, 527–548.

Wood, R., 2012: Stratocumulus Clouds. *Mon. Weather Rev.*, **140**, 2373–2423, doi:10.1175/MWR-D-11-00121.1.

World Meteorological Organization, 1986: *Atmospheric Ozone, Global Ozone Research Monitoring Project. Vol. I, Report No. 16, 392 pp.*

Wyant, M. C., and Coauthors, 2010: The PreVOCA experiment: modeling the lower troposphere in the Southeast Pacific. *Atmos. Chem. Phys.*, **10**, 4757–4774, doi:10.5194/acp-10-4757-2010. http://www.atmos-chem-phys.net/10/4757/2010/.

Yang, H., and J. Kleissl, 2016a: Preprocessing WRF initial conditions for coastal stratocumulus forecasting. *Sol. Energy*, **133**, 180–193,

doi:10.1016/j.solener.2016.04.003. http://dx.doi.org/10.1016/j.solener.2016.04.003.

——, and ——, 2016b: Preprocessing {WRF} initial conditions for coastal stratocumulus forecasting. *Sol. Energy*, **133**, 180–193, doi:10.1016/j.solener.2016.04.003. http://dx.doi.org/10.1016/j.solener.2016.04.003.

Zamo, M., O. Mestre, P. Arbogast, and O. Pannekoucke, 2014: A benchmark of statistical regression methods for short-term forecasting of photovoltaic electricity production , part I : Deterministic forecast of hourly production. *Sol. Energy*, **105**, 792–803, doi:10.1016/j.solener.2013.12.006. http://dx.doi.org/10.1016/j.solener.2013.12.006.

Zeng, J., and W. Qiao, 2013: Short-term solar power prediction using a support vector machine. *Renew. Energy*, **52**, 118–127, doi:10.1016/j.renene.2012.10.009. http://dx.doi.org/10.1016/j.renene.2012.10.009.

Zeng, J., S. Madronich, and K. Stamnes, 1996: A note on the use of the two-stream delta-scaling approximation for calculating atmospheric photolysis rate coefficients. *J. Geophys. Res.*, **101**, 14,525-14,530.

Zhong, X., and J. Kleissl, 2015: Clear sky irradiances using REST2 and MODIS. *Sol. Energy*, **116**, 144–164, doi:10.1016/j.solener.2015.03.046.

——, J. A. Ruiz-Arias, and J. Kleissl, 2016: Dissecting Surface Clear Sky Irradiance Bias in Numerical Weather Prediction: Application and Corrections to the New Goddard Shortwave Scheme. *Sol. Energy*, **132**, 103–113, doi:10.1016/j.solener.2016.03.009.

——, D. K. Sahu, and J. Kleissl, 2017: WRF inversion base height ensembles for simulating marine boundary layer stratocumulus. *Sol. Energy*, **146**, 50–64, doi:10.1016/j.solener.2017.02.021. http://dx.doi.org/10.1016/j.solener.2017.02.021.

SolarAnywhere, 2016. Web-Based Service that Provides Hourly, Satellite-Derived Solar Irradiance Data Forecasted 7 Days Ahead and Archival Data Back to January 1, 1998. https://www.solaranywhere.com/products/solaranywhere-data/ (Accessed September 4, 2016).

2012: SoDa Linke Turbidity. http://www.soda-is.com/eng/services/linke_turbidity_info.html (Accessed January 5, 2016).